ORGANIC DOTS WITH AGGREGATION-INDUCED EMISSION CHARACTERISTICS FOR BIOLOGICAL APPLICATIONS

FENG GUANGXUE

(B. Eng (Hons.), NUS)

A THESIS SUBMITTED FOR THE DEGREE OF DOCTOR OF PHILOSOPHY

DEPARTMENT OF CHEMICAL & BIOMOLECULAR ENGINEERING

NATIONAL UNIVERSITY OF SINGAPORE

2015

DECLARATION

I hereby declare that the thesis is my original work and it has been written by me in its entirety. I have duly acknowledged all the sources of information which have been used in the thesis.

This thesis has also not been submitted for any degree in any university previously.

FENG Guangxue

5th Jan 2016

ACKNOWLEDGESMENTS

I would like to take this opportunity to thank all the people who have helped me during the wonderful and exciting four years of my Ph.D. study.

Firstly and most importantly, my greatest appreciation goes to my supervisor, Prof. Liu Bin, for her constructive guidance, continuous inspiration and encouragement throughout my doctoral study. She led me to this promising and amazing research world of nanomaterials and aggregation-induced emission which I started with almost zero knowledge. Her enthusiasm and persistence in science, rigorous and vigorous methodology always encouraged me to hunger for adventure of novel research fields and topics.

I would like to sincerely thank Dr. Li Kai, Dr. Ding Dan, Dr. Liu Jie, and Dr. Geng Junlong for teaching and guiding me, without their help I could not complete my Ph.D. study. I am grateful to Dr. Hu Qinglian, Dr. Liang Jing, Dr. Yuan Youyong, Dr. Wang Guan, Dr. Zhang Chongjing, Dr. Shi Haibin, Dr. Xue Zhaosheng, Dr. Wang long, Ms. Zhang Ruoyu, Mr. Cai Xiaolei for their kind help. I appreciate other collaborators for their great supporting and help in my experiments. I am also grateful to Mr. Boey Kok Hong, Ms. Lee Chai Keng, Mr. Liu Zhicheng, Ms. Lim Kwee Mei and other technicians for their supports and assistance.

I wish to acknowledge Singapore Perking Oxford Research Enterprise (SPORE) and National University of Singapore for providing scholarships, Chinese government for the Award for Outstanding Self-Financed Students Abroad in 2014, and Department of Chemical and Biomolecular Engineering for research facilities.

Finally, I would love to thank my parents, my parents-in-law, relatives, friends and especially my beloved wife, Ms. Hu Yating, for their unconditional love, understanding, and encouragement in my everyday life.

TABLE OF CONTENTS

DECLARATION.....i

ACKNOWLEDGESMENTS.....ii

TABLE OF CONTENTS..... iii

SUMMARY.....vii

LIST OF FIGURES.....ix

LIST OF SCHEMES.....xiv

LIST OF SYMBOLS.....xv

CHAPTER 1 INTRODUCTION.....1

1.1 Background.....2

1.2 AIE Fluorogens.....4

1.3 Synthesis of AIE Dots.....8

1.3.1 Silica AIE Dots.....9

1.3.2 Organic AIE Dots.....11

1.4 AIE Dots for Biological Applications.....18

1.4.1 *In Vitro* Imaging.....19

1.4.2 *In Vivo* Imaging.....22

1.4.3 Theranostic Applications.....27

1.5 Research Objectives.....31

1.6 Thesis Outline.....33

CHAPTER 2 GENERAL STRATEGY OF PREPARING ULTRA-BRIGHT ORGANIC DOTS WITH AGGREGATION-INDUCED EMISSION CHARACTERISTICS AS A FACILE CELL TRACKER.....34

2.1 Introduction.....35

2.2 Experimental.....37

2.2.1 Materials.....37

2.2.2 Fabrication of AIE Dots.....38

2.2.3 Fabrication of AIE-Tat Dots.....38

2.2.4 Characterization.....38

2.2.5 Calculation of AIE Dot Concentration.....39

2.2.6 Single Particle Fluorescence Imaging.....39

2.2.7 Cell Culture 40
2.2.8 Cell Labelling by AIE-Tat Dots 41
2.2.9 Cytotoxicity of AIE-Tat Dots 42
2.2.10 Cell Labelling by GFP 42
2.2.11 *In Vitro* Cell Tracing 43
2.3 Results and Discussion 44
2.3.1 Fabrication of AIE-Tat Dots 44
2.3.2 Characterization of AIE-Tat Dots 46
2.3.3 *In Vitro* Cellular Imaging by AIE-Tat Dots 50
2.3.4 *In Vitro* Cell Labelling Comparison between GFP and AIE-Tat Dots 53
2.3.5 *In Vitro* Long Term Cell Tracing 56
2.4 Conclusion 57
CHAPTER 3 MULITMODAL DETECTION OF VASCULAR INTEGRITY AND LEAKAGE BY GADOLINIUM FUNCTIONALIZED ORGANIC DOTS WITH AGGREGATION-INDUCED EMISSION CHARACTERISTICS 59
3.1 Introduction 60
3.2 Experimental 62
3.2.1 Materials 62
3.2.2 Characterization 63
3.2.3 Synthesis of AIE-Gd Dots 63
3.2.4 Single Particle Fluorescence Imaging 64
3.2.5 Two-Photon Absorption Measurement 65
3.2.6 Blood Vascular Imaging 65
3.2.7 Evans blue Detection 66
3.2.8 Gd Contents Detection 66
3.3 Results and Discussion 67
3.3.1 Fabrication of AIE-Gd Dots 67
3.3.2 Characterization of AIE-Gd Dots 68
3.3.3 Inflammation Imaging 72
3.3.4 Quantification of Vascular Leakage 74
3.3.5 Real-Time Monitoring of Vascular Leakage 76
3.4 Conclusion 77
CHAPTER 4 ORGANIC DOTS WITH AGGREGATION-INDUCED EMISSION CHARACTERISTICS FOR TARGETED AND IMAGE-GUIDED PHOTODYANMIC THERAPY 78
4.1 Introduction 79
4.2 Experimental 80
4.2.1 Materials 80

4.2.2 Characterization 81
4.2.3 Preparation of AIE Aggregates 81
4.2.4 ROS Measurement in Solution 82
4.2.5 Preparation of TPETPADCM Loaded AIE Dots 82
4.2.6 Conjugation of cRGD to TPETPADCM Dots 82
4.2.7 Cell Culture 83
4.2.8 Intracellular ROS Detection 83
4.2.9 Confocal Imaging 83
4.2.10 Cytotoxicity Studies 84

4.3 Results and Discussion 85

4.3.1 Synthesis and Characterization of TPETPADCM 85
4.3.2 Synthesis and Characterization of TPETPADCM-cRGD Dots 87
4.3.3 Targeted Cellular Imaging 89
4.3.4 Photodynamic Therapy 91

4.4 Conclusion 94

CHAPTER 5 CELLULAR AND MITOCHONDRIA DUAL TARGETED ORGANIC DOTS WITH AGGREGATION-INDUCED EMISSION CHARACTERISTICS FOR IMAGE-GUIDED PHOTODYNAMIC THERAPY 95

5.1 Introduction 96

5.2 Experimental 97

5.2.1 Materials 97
5.2.2 Characterization 98
5.2.3 Preparation of DPBA-TPE 98
5.2.4 Preparation of DPBA-TPE Nanoaggregates 99
5.2.5 ROS Generation Measurement 99
5.2.6 Preparation of AIE Dots 100
5.2.7 Confocal Imaging 100
5.2.8 Measurement of Mitochondrial Membrane Potential 101
5.2.9 Flow Cytometry 101
5.2.10 Cell Migration Assay 101
5.2.11 Cytotoxicity Studies 102

5.3 Results and Discussion 103

5.3.1 Synthesis and Characterization of DPBA-TPE 103
5.3.2 Fabrication and Characterization of AIE dots 105
5.3.3 Cellular and Mitochondria Dual Targeted Imaging 108
5.3.4 Photodynamic Therapy of AIE Dots 111
5.3.5 Mitochondria Membrane Potential Study 113
5.3.6 Cell Migration Study 114

5.4 Conclusion 116

CHAPTER 6 CONCLUSIONS AND RECOMMENDATIONS 117
6.1 Conclusions 118
6.2 Recommendations 121
REFERENCES 124
LIST OF PUBLICATIONS 134

SUMMARY

Fluorescence imaging technique that provides the direct visualization of biological species or processes has become the most indispensable platform and modern imaging modality for fundamental studies of live science as well as in practical applications. However, the aggregation-caused quenching (ACQ) effect of conventional organic dyes has greatly hampered their biological applications and fluorescent nanoparticle fabrication. Recently, the novel fluorogens with unique aggregation-induced emission (AIE) characteristics which show intensified fluorescence in aggregate state have attracted great research interests in imaging and other biological applications. However, the applications of AIE fluorogens (AIEgens) have been mainly focused on the development small molecular bio-probes for sensing and detection, where the merits of AIE are not fully utilized. The AIE feature enables the fabrication of ultra-bright fluorescent nanoparticles, which can serve as the promising imaging reagents with high sensitivity and imaging contrast. In this thesis, I developed a general strategy to fabricate organic AIE dots with high brightness, good colloidal and photostability, surface functionalization, and desirable optical properties for *in vitro* and *in vivo* imaging, and image-guided photodynamic therapy.

Firstly, a generic and simple strategy to synthesize ultra-bright AIE dots with amendable surface functional groups has been developed. Upon surface decoration with cell penetration peptide, the *in vitro* long-term cell tracking application was demonstrated. Following that, the Gadolinium (III) was successfully chelated onto the surface of AIE dots which possess bright fluorescence under two-photon excitation to detect the inflammation severity through the visualization of blood vascular leakage. AIEgen with efficient reactive oxygen species (ROS) generation in aggregate state was

further designed and encapsulated into AIE dots for image-guided targeted cancer photodynamic therapy. At last, efforts were made to address the intracellular localization of AIE dots, where AIE dots with cellular and mitochondria dual-targeted capabilities were fabricated, showing enhanced photodynamic therapy compared to random distributed AIE dots in cytoplasm.

LIST OF FIGURES

Figure 1.1. Fluorescence photographs of A) DDPD with aggregation-caused quenching (ACQ) feature, and B) TPE and C) TPE-DDPD with aggregation-induced emission (AIE) characteristics in THF/water mixtures with different water fractions under UV illumination.[39] Copyright 2013 American Chemical Society. 5

Figure 1.2. Schematic illustration of AIE mechanisms: restriction of intramolecular motions (RIM): RIR for TPE and RIV and THBA.[46] Copyright 2014 Wiley-VCH. 7

Figure 1.3. Schematic illustration of Silica AIE dots formations: A) ORMOSIL dots encapsulating BDSA.[53] B) TPE-containing fluorescent silica AIE dots.[56] Copyright 2014 Royal Society of Chemistry and 2010 Wiley-VCH.....9

Figure 1.4. A) Chemical structures of TPE-CS, and the photograph of TPE-CS and FCS under light irradiation. B) SEM image of PTPEE dots. C) TEM image of Net-TPS-DMA dots. D) AFM image of cRGD-TPE-Pt-DOX dots.....13

Figure 1.5. A) Fluorescence image of HeLa cells stained by FSNPs at TPE concentration of 6 μM.[56] B) Two-photon excited fluorescence image of MCF-7 stained by folate functionalized AIE dots.[72] All the images share the same scale bar of 20 μm. Copyright 2010 Wiley-VCH and 2011 Royal Society of Chemistry. 20

Figure 1.6. A) Chemical structures of **1a** and **1b**, b) SEM image of **1a** aggregates formed in THF/water mixture. C) Fluorescence intensities and images of HeLa cell stained by 5 μM of **1b** and 200 nM MTG at different passages (Psg).[79] Copyright 2012 Wiley-VCH. 21

Figure 1.7. A) In vivo non-invasive fluorescence imaging of H22-tumor-bearing mice after intravenous injection of TPETPADCM loaded BSA dots. B) Ex vivo fluorescence imaging on tumor tissue and major organs of mice treated with BSA dots.[74] Copyright 2012 Wiley-VCH. 23

Figure 1.8. A) Schematic illustration of AIE dots. B) Fluorescence time-traces of four individual AIE dots with different brightness levels. C) In vivo fluorescence imaging of the mouse subcutaneously injected with 1×10^6 of C6 glioma cells labelled with C) AIE dots, or D) QD655.[76] Copyright 2013 Nature Publishing Group. 25

Figure 1.9. 3D reconstructed two-photon fluorescence images of blood vessels in A) brain (0–425 μm), B) bone marrow (0–108 μm), and C) mouse ear skin (0–132 μm) from the mouse injected with BTPEBT AIE dots. All images share the same scale bar of 20 μm.[82] Copyright 2013 Wiley-VCH. 26

Figure 1.10. Confocal fluorescence images of the distribution of TPED (TPE-mPEG 75 μM and DOX 5 μM) in MCF-7 cancer cells with different incubation time. All the

images share the same scale bar of 20 μm.[87] Copyright 2014 American Chemistry Society.....28

Figure 2.1. PL spectra of BTPEBT in THF/water mixtures with various water fractions, (A) f_w = 0 to 50 vol%, (B) f_w = 50 to 90 vol%. [BTPEBT] = 10 μM, λ_{ex} = 422 nm...45

Figure 2.2. (A) LLS result of AIE-Tat dots in aqueous solution, inset is TEM image of AIE-Tat dots. (B) Hydrodynamic diameter changes of AIE-Tat dots upon continuous incubation in 1×PBS at 37 ºC for 10 days. (C) Absorption and PL spectra of AIE-Tat dots in water at room temperature. (D) PL intensity changes of AIE-Tat dots at 547 nm in water at different pH. λ_{ex} = 420 nm. 46

Figure 2.3. (A) Representative wide field fluorescence image of individual AIE-Tat dots. (B) Corresponding fluorescence intensity histogram of AIE-Tat dots (1338 dots) emitted during 100s. (C) Fluorescence changes of individual AIE-Tat dots after 100s laser scanning.....48

Figure 2.4. Representative fluorescence time traces of A) two AIE-Tat dots and B) two QD Tracker 585 within 100s.....49

Figure 2.5. CLSM images of HEK 293T cells after incubation with AIE-Tat dots at different concentrations for 2 h. All the images share the same scale bar of 30 μm...50

Figure 2.6. A) Fluorescence, B) white field, and C) fluorescence/white field overlay images of HEK 293T cell after 2 h incubation with AIE dots (2 nM).....51

Figure 2.7. (A) CLSM images of HEK 293T cells after incubation with AIE-Tat dots (2 nM, 2 h) and Lysotracker Red DND-99 (75 nM, 30 min) in sequence. (B) 3D CLSM image of AIE-Tat dots treated HEK 293T cells. (C) Flow cytometry histograms of HEK293T cells stained by 2 nM AIE-Tat dots at 37 ºC for 24 h (red line), unstained cells (black line) and a mixture of AIE-Tat dot-stained HEK293T cells and unstained cells (1:1; blue line) after 2 days co-culture. The histograms were recorded after co-culturing for 2 days after mixing. 52

Figure 2.8. (A) Flow cytometry histograms of different cell lines after pMAX-GFP expression (red lines), AIE-Tat dots staining (blue lines) or without any treatment (black lines).....53

Figure 2.9. Fluorescence/transmission overlay images of pMAX-GFP expressed cells and AIE-Tat dots labelled cells. Insets are labelling rates measured by flow cytometry. All the images share the same scale bar.....54

Figure 2.10. A) Photostability of AIE-Tat dots and GFP in HEK293T cells. B) Cell viability of HEK293T cells after incubation with AIE-Tat dots at different concentrations for 24 and 48 h, respectively. 55

Figure 2.11. (A) Continuous monitoring of cell labelling rates by GFP or AIE-Tat dots for 10 days. (B) and (C) Flow cytometry histograms of HEK 293T cells after incubation with (B) 2 nM AIE-Tat dots or (C) 5 μg/well p-MAX-GFP plasmid overnight and then sub-cultured for designated times. (D) and (E) CLSM images of HEK293T cells labelled by (D) AIE-Tat dots or (E) pMAX-GFP at different days post-incubation. All the images share the same scale bar. 56

Figure 3.1. A) LLS result, and B) TEM image of AIE-Gd dots. C) Absorption and PL spectra of AIE-Gd dots before and after Gd chelation. D) Hydrodynamic size and fluorescence changes of AIE-Gd dots in 1× PBS buffer. 69

Figure 3.2. A) Luminescence image, B) luminescence intensity histogram, C) representative luminescence intensity time-traces of TPETPAFN loaded AIE dots. .. 70

Figure 3.3. Two-photon absorption spectrum of AIE dots in water. 71

Figure 3.4. Intravital TPFI of mouse ears A) without or B) with inflammation. The inflammatory ear was first treated with 1% croton oil (40 μL) for 3 h, followed by AIE-Tat dots injection, and immediate imaging. 72

Figure 3.5. Intravital TPFI of mouse ears A) without or B) with inflammation. The croton oil treatment and AIE dots injection were conducted as the same time. At 3 h post-injection, croton oil is removed, and the images were obtained. 74

Figure 3.6. A) Amount of Gd and B) absorption of Evans blue in inflammation and healthy ears after designated croton oil treatment. The AIE-Gd dots and Evans blue was injected at the starting time of croton oil treatment. 74

Figure 3.7. A) Time-lapse images of AIE-Gd dots treated mouse ear before and after laser burn. B) Fluorescence intensity changes of selected two areas before and after laser burn. The neutrophils are GFP genetically modified. 76

Figure 4.1. A) Chemical structure of TPETPADCM. B) PL spectra of TPETPADCM (λ_{ex} = 502 nm) in THF/water mixtures with different water fractions (f_w). 85

Figure 4.2. A) PL spectra of the mixture of TPETPADCM aggregates and DCFH. B) DCFH PL peak intensity changes under continuous light irradiation. 86

Figure 4.3. A) Size distribution and TEM image (inset), B) absorption and emission spectra, and C) ROS generation of TPETPADCM-cRGD dots. 88

Figure 4.4. Confocal images of A) MDA-MB-231, B) MCF-7, C) NIH 3T3 cells, and D) free cRGD (50 μM) pre-treated MDA-MB-231 cells upon incubation with TPETPADCM-cRGD dots (1 μg/mL) for 1 h. The blue fluorescence from the nuclei of cells is dyed by Hoechst 33342, the red fluorescence is from TPETPADCM-cRGD dots. All the images share the same bar of 20 μm. 90

Figure 4.5. Detection of intracellular ROS production by dichlorofluorescein diacetate (DCF-DA) in A) MDA-MB-231, A) MCF-7 and C) NIH 3T3 cells after incubation with TPETPADCM-cRGD dots (10 μg/mL) followed by light irradiation. All the images share the same scale bar of 50 μm. 91

Figure 4.6. Inhibition of MDA-MB-231, MCF-7 and NIH 3T3 cells growth in the presence of different concentrations of TPETPADCM-cRGD dots A) without or B) with light irradiation (0.25 W cm^{-1}, 2 min) followed by further incubation of the cells for 24 h. Data represent mean values ± standard deviation, n = 3. 92

Figure 4.7. Cell apoptosis imaging using FITC-tagged Annexin V in MDA-MB-231 (A), MCF-7 (B) and NIH 3T3 (C) cells incubated with TPETPADCM-cRGD dots after light irradiation. All images share the same scale bar of 20 μm. 93

Figure 5.1. A) PL spectra of **DPBA-TPE** (10 μM) in THF/water mixtures with different water fractions. B) PL spectra of **DPBA-TPE** (10 μM) and DCFH (2 μM) mixture in water with different white light irradiation time (250 mW cm^{-2}).....104

Figure 5.2. A) Absorption and PL spectra, and B) hydrodynamic diameters and surface zeta potentials of three AIE dots in water. TEM image of C) **AIE-FA**, D) **AIE-TPP**, and E) **FA-AIE-TPP** dots.....106

Figure 5.3. ROS generation of **FA-AIE-TPP** dots in aqueous solution at A) varied dot concentrations with a fixed light power of 250 mWcm^{-2}, and B) varied light powers with fixed dot concentration of 2 μg/mL upon irradiation for 300 s, using DCFH (2 μM) as ROS indicator. 108

Figure 5.4. Flow cytometry histograms of A) NIH-3T3 cells and B) MCF-7 cells after incubation with AIE dots (20 μg/mL) for 4 h. 109

Figure 5.5. CLSM images of A) MCF-7 cancer cells and B) NIH-3T3 normal cells after incubation with AIE dots (20 μg/mL) and MitoTracker Green (200 nM). AIE dots: E_x: 543 nm, E_m: > 650 nm; MitoTracker Green: E_x = 488, E_m = 505 – 525 nm. The scale bar size is 10 μm for all images. 110

Figure 5.6. Viabilities of MCF-7 cancer cells and NIH-3T3 normal cells after incubation with A) **AIE-TPP**, B) **AIE-FA**, C) **FA-AIE-TPP** dots at varied concentrations, followed by white light irradiation (250 mWcm^{-2}). D) and E) Annexin V labeled MCF-7 cells after incubation with **FA-AIE-TPP** dots (20 μg/mL) without (D) or with (E) light irradiations (250 mWcm^{-2}). D) and E) share the same scale bar. 111

Figure 5.7. A-C) MMP changes of **FA-AIE-TPP** dots (20 μg/mL) treated MCF-7 cancer cells measured by JC-1 (2 μg/mL) after light irradiation (100 mW cm^{-2}) for A) 0, B) 5, and C) 10 min. D) MMP changes of MCF-7 without FA-AIE-TPP dots treatment under light irradiation. All the images share the same scale bar. 113

Figure 5.8. A) White field image of **FA-AIE-TPP** dots treated NIH-3T3 and MCF-7 cells before (up) and after 72 h culture (bottom). Both cells were incubated with **FA-AIE-TPP** dots (20 μg/mL based on **DPBA-TPE** mass concentration) for 4 h, followed by light exposure (100 mW/cm^2) for 10 min. B) The effects of AIE dots treatment on migration of MCF-7 cells with and without light irradiation. 115

LIST OF SCHEMES

Scheme 1.1. Schematic illustration of organic AIE dots from A) self-assembly, and B) polymerization.[61] Copyright 2014 Royal Society of Chemistry. 12

Scheme 1.2. A) Chemical structure of TPETPAFN and its emission intensity changes in THF/water mixture. B) Schematic illustration of the fabrication of PLGA-PEG-Fol AIE dots eccentrically or homogeneously loaded with TPETPAFN.[73] Copyright 2012 Wiley-VCH. 17

Scheme 1.3. Chemical structure of Net-TPE-PEI-DMA and the schematic illustration of it as pH-responsive light-up AIE dots for targeted imaging and selective suppression of cancer cells.[68] Copyright 2015 Royal Society of Chemistry. 30

Scheme 2.1. A) Chemical structures of BTPEBT, DSPE-PEG_{2000}, and DSPE-PEG_{2000}-Mal. B) Schematic illustration of AIE-Tat dots formation. 44

Scheme 3.1. Chemical structures of DSPE-PEG_{2000}-NH_2, TPETPAFN and DOTA, and the schematic illustration of AIE-Gd dots formation. 67

Scheme 4.1. Schematic illustration of TPETPADCM-cRGD dots for image-guided photodynamic therapy. 87

Scheme 5.1. Chemical structure of **DPBA-TPE**. 103

Scheme 5.2. Schematic illustration of **FA-AIE-TPP** dots for specific targeting of FR-positive MCF-7 breast cancer cell mitochondria for image-guided PDT. 105

LIST OF SYMBOLS

AA	Arylic acid
ACQ	Aggregation-caused quenching
ADSCs	Adipose-derived stem cells
AFM	Atomic force microscopy
AIE	Aggregation-induced emission
APS	(3-Aminopropyl)triethoxysilane
BDSA	9,10-Bis[4-(4-aminostyryl)styryl]anthracene derivative
BMSCs	Bone marrow stem cells
BODIPY	Boron-dipyrromethene
BSA	Bovine serum albumin
CLSM	Confocal laser scanning microscopy
cRGD	Cyclic arginine−glycine−aspartic acid tripeptide
CS	Chitosan
CTAB	Cetyltrimethyl ammonium bromide
DCF-DA	Dichlorofluorescein diacetate
DCFH	Dichlorofluorescin
DCM	Dichloromethane
DDPD	N,N-dicyclohexyl-1,7-dibromo-3,4,9,10-perylenetetracarboxylic diimide
DL	Degree of labelling
DMA	Dimethylmaleic anhydride
DMEM	Dulbecco's Modified Eagle Medium
DMF	Dimethylformamide
DMSO	Dimethyl sulfoxide
DOX	Doxorubicin

DPBF	1,3-Diphenylisobenzofuran
DSPE-PEG$_{2000}$	1,2-distearoyl-sn-glycero-3-phosphoethanolamine-N-[methoxy(polyethylene glycol)-2000]
EPR	Enhanced pemearbility and retention
FA	Folic acid
FBS	Fetal bovine serum
FITC	Fluorescein isothiocyanate
FP	Fluorescent protein
FRET	Förster resonance energy transfer
Gd	Gadolinium
GFP	Green fluorescent protein
HPS	Hexaphenylsilole
IC_{50}	Half maximal inhibitory concentration
ICP-MS	Ionic coupled plasma mass spectrometry
LLS	Laser light scattering
MRI	Magnetic resonance imaging
NIR	Near infrared
NMP	N-Methyl-2-pyrrolidinone
NMR	Nuclear magnetic resonance
NPs	Nanoparticles
NPAFN	Bis(4-(*N*-(1-naphthyl) phenylamino)-phenyl)fumaronitrile
PBS	Phosphate buffer saline
PDT	Photodynamic therapy
PEG	Polyethylene glycol
PEG-*b*-PCL	Poly(ethylene glycol)-*b*-poly(e-caprolactone)
PEG-*b*-PS	Poly(ethyleneglycol)-*b*-poly(styrene)
PEI	Polyethyleneimie

PL	Photoluminescence
PLGA	Poly(lactide-*co*-glycolide)
PMAA-b-PS	Poly(methacrylic acid)-*b*-poly(styrene)
PSs	Photosensitizers
Pt	Cisplatin
PTPEE	Ppoly[(2-(4-vinylphenyl)ethene-1,1,2-triyl)tribenzene]
PVA	Poly(vinyl alcohol)
QDs	Quantum dots
RAFT	Reversible addition–fragmentation chain transfer
RES	Reticuloendothelial system
RIM	Restriction of motions
RIR	Restriction of rotation
RIV	Restriction of vibration
ROS	Reactive oxygen species
SEM	Scanning electron microscopy
St	Styrene
TEM	Ttransmission electron microscopy
TEOS	Tetraethsilane
THBA	Tetrahydro-bidibenzo-annulenylidene
THF	Tetrahydrofuran
TICT	Twisted intramolecular charge transfer
TPA	Two-photon absorption
TPE	Tetraphenylethene
TPEE	(2-(4-Vinylphenyl)ethene-1,1,2-triyl)tribenzene
TPE-ICT	1-[4-(Isothiocyanatomethyl)phenyl]-1,2,2-triphenylethene
TPFI	Two-photon fluorescence imaging

TPP	Triphenylphosphine
TPS	Tetraphenylsilole
VTES	Triethoxyvinylsilane
δ	Two-photon absorption cross section

CHAPTER 1

INTRODUCTION

1.1 Background

Biological imaging that provides direct visualized information of biological species or processes has become the most important modern tool for fundamental studies of live science and in the practical and clinical applications such as diagnosis, prognosis and therapy of cancer and other diseases.[1-6] Up to now, a large variety of imaging modalities have been developed and widely applied in the biological investigation from the macroscopic to microscopic, and further to sub-cellular levels. Among these advanced imaging techniques, such as computer tomography,[7, 8] magnetic resonance imaging (MRI),[9-11] ultrasound,[12] and photoacoustic imaging,[13, 14] fluorescence imaging technique has served as a reliable and vital indispensable platform for non-invasive bio-detection, bio-sensing and bio-imaging in the sub-cellular, cellular, tissue, and whole body levels due to their advantages in the regards of inexpensive materials, manoeuvrable equipment and high temporal-spatial resolution.[15-17] To achieve optimal physiological behaviour and reliable performance with high resolution contrast, high sensitivity, and minimal perturbation to biological interference, these fluorescent materials should possess high brightness, good photostability, and ease of functionalization.

The engineered expression of fluorescent proteins (FPs) inside cells has dominated the field of fundamental cell study, such as programmed cell death, cell linage commitment, and other biochemical processes.[18-21] However, the integration of FP genes into cells genomes is facing the safety issues of introduction of random insertional gene mutation,[22, 23] while non-viral approach exhibited unstable and cell-dependent FP transfections.[24, 25] Moreover, the existence of time lag between FP

expression and transcriptional, translational and post-translationally regulated processes will result in inconsistence when immediate signal readout is required.[26-28]

Conventional organic fluorescent dyes have been extensively used in various imaging related biological applications. Numerous organic fluorogens (e.g., rhodamine, fluorescein, and BODIPY) and their later modified derivatives have been developed and showed their own merits in cell imaging, cellular organelle detection, and cell dynamics studies. However, these traditional organic dyes suffer from intrinsic drawbacks which greatly hampered their biological applications. One of the particular drawbacks is their poor photo-resistance to irradiation which results in rapid diminished fluorescence under continuous excitation, making them not suitable for bio-imaging analysis over long period. On the other hand, their optical properties are largely susceptible to surrounding inferences and the unexpected interactions with random biomolecules and proteins in complex environment would most-likely mislead the experiment results when high sensitivity and resolution are required.

Encapsulation of the organic dyes into nanoparticles (NPs) or dots has been served as a promising strategy to increase their stability in both *in vitro* and *in vivo* applications. Various matrices have been developed for the dye encapsulation, such as lipids, polymers, and silica. These matrices prevent the unexpected interactions of the dye molecules with surrounding molecules or oxygen which improves the photostability and the resistance to surrounding stimuli changes. Moreover, the surface of these fluorescent NPs can be further functionalized with different ligands, functional molecules, adapters, peptides or antibodies for targeting and other specific purposes. However, the intrinsic narrow Stokes shifts still remain challenged for multiplex imaging applications. On the other hand, the fluorescence of conventional organic dyes

will be quenched at high concentration or in aggregated states, which is known as aggregation-caused quenching (ACQ).[29] The notorious ACQ phenomena not only forces the use of dilute solution of bio-probes, leading to poor sensitivity and reliability, but also results in weakened brightness when being encapsulated into NPs. For example, encapsulating Nile Red into NPs will result in almost zero fluorescence at high loading percentage,[30] largely compromising imaging contrast.

In the respect of brightness, photostability, and Stokes' Shifts, the fluorescent spherical semiconductor crystals known quantum dots (QDs) have shown their own merits in the field of optoelectronic devices and biomolecules detection and fluorescent imaging.[31, 32] The broad absorption and narrow emission spectra also make QDs especially suitable for multi-colour fluorescence imaging with single excitation wavelength to simultaneously monitoring different cellular activities. However, QDs exhibit fluorescence intermittency under excitation, known as 'blinking', which makes them not suitable for single particle tracing studies.[33] In addition, the inevitable fact that QDs are made up of heavy metal elements that are intrinsic toxic to cells, animals and human beings has greatly limited their practical applications and clinical studies.[34] ACQ phenomena also has been found on QDs.[35] As a consequence, novel fluorescent materials with high brightness, good photostability and less cytotoxicity are highly desirable for imaging-related biological applications.

1.2 AIE Fluorogens

As described in previous section, the ubiquitous ACQ effect has been compromising the detection sensitivity and imaging resolution contrast. Researchers have been forced to utilize diluted fluorogens in their studies, where the emission is often weak and the small amounts of dyes are easily and quickly photo-bleached under

harsh laser, which have led to poor sensitivities and caused many inconvenience and problems.[36-38] Since most fluorogens are hydrophobic, they tend to form cluster in the hydrophobic cavities or attach onto bio-molecule surface with diminished emission. In addition, despite of the rapid progresses of nanotechnology and nanoparticle systems, the notorious ACQ effect has greatly hampered the development of conventional organic dye based NPs for biological applications.

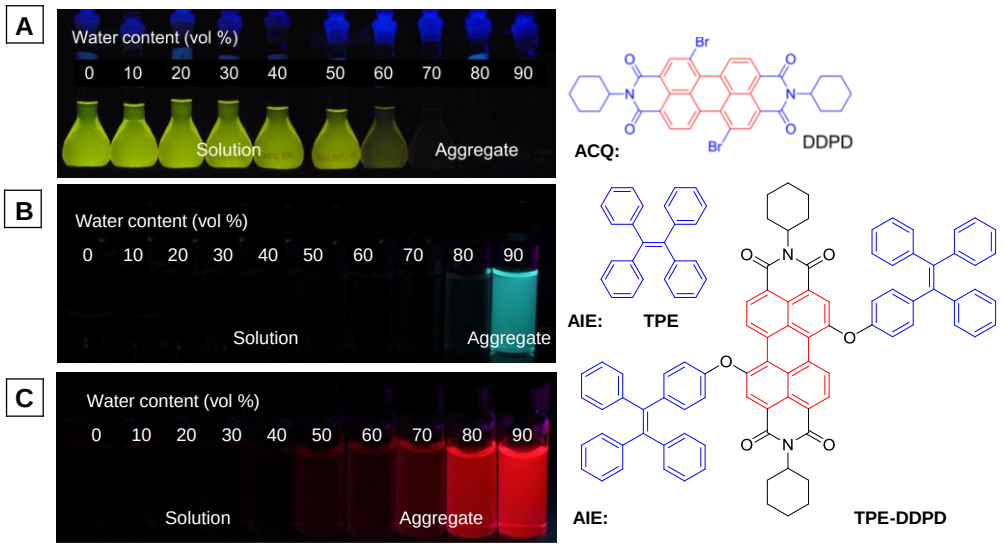

Figure 1.1. Fluorescence photographs of A) DDPD with aggregation-caused quenching (ACQ) feature, and B) TPE and C) TPE-DDPD with aggregation-induced emission (AIE) characteristics in THF/water mixtures with different water fractions under UV illumination.[39] Copyright 2013 American Chemical Society.

This inevitable ACQ phenomenon in biological detection and imaging has become a harmful photophysical effect and thorny obstacle in luminescence researches and practical applications. Taken N,N-dicyclohexyl-1,7-dibromo-3,4,9,10-perylenetetracarboxylic diimide (DDPD) as an example (Figure 1A), the structures of these conventional organic dyes are normally composed of planar aromatic rings.[39] In good solvent such as tetrahydyrofuran (THF), DDPD emits strong fluorescence under UV illumination. In poor solvent such as THF/water mixture with increased water fraction (70%), these disc-like DDPD molecules tend to form strong π-π stacking structures, which promote the excimer and exciplexes formation, resulting in obvious

ACQ phenomenon.[39] Many efforts and different chemical and physical approaches have been taken to mitigate the ACQ effects, but with limited success.[40-42]

In 2001, Tang and co-authors discovered and reported a new system of fluorogens, which is found to be non-fluorescence when molecularly dispersed in good solvent but become highly emissive in poor solvent or form aggregates.[43, 44] This novel and exciting phenomenon that is exactly opposite to ACQ effect is known as aggregation-induced emission (AIE). One of the typical AIE fluorogens (AIEgens) is tetraphenylethene (TPE) (Figure 1.1B), which is non-emissive when molecularly dispersed in THF solution but can be induced to emit strong blue emission when forming aggregates in THF/water mixture with high water fraction.[42] Along with the development of material science, more fluorogens with AIE characteristics have been discovered such as tetraphenylsilole (TPS), hexaphenylsilole (HPS) and other derivatives. Moreover, recent discovery that amalgamation of AIEgens with conventional ACQ fluorogens will efficiently transform ACQ fluorogens to AIEgens further enriched the class of AIEgens with more emission colours and applications. For example, conjugation TPE moieties to DDPD skeleton will achieve a new fluorogen TPE-DDPD, which is not emissive in THF but shows bright red emission in aggregate (Figure 1.1C).[45] This discovery of AIEgens can take the advantage of nature aggregate formation in biological system rather than tackling or fighting against it, which have much more promising potentials in practical implications.

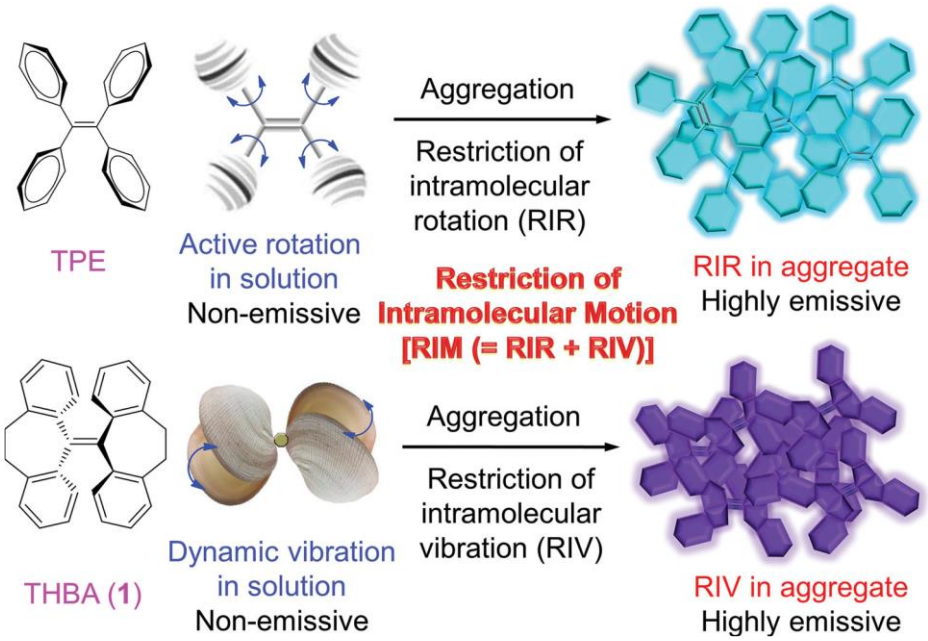

Figure 1.2. Schematic illustration of AIE mechanisms: restriction of intramolecular motions (RIM): RIR for TPE and RIV and THBA.[46] Copyright 2014 Wiley-VCH.

Along with its discovery, many efforts have been put into the study of AIE mechanism. Up to now, it has come to a clear picture of the AIE mechanism, which is the restriction of intramolecular motions (RIM).[46-48] The RIM includes two parts: restriction of intramolecular rotation (RIR) and restriction of intramolecular vibration (RIV). Taken TPE as an example, which exhibits non-planar propeller like structures. These four phenyl rings can undergo free rotation or twist when molecularly dispersed, which will transfer the photonic energy into heat or active intramolecular rotation through the non-radiative decay (Figure 1.2). Unlike conventional fluorogens, the π-π stacking of AIEgens in aggregated state is blocked, which also blocks the free rotation of molecular rotator and the non-radiative decay. As a consequence, the radiative pathways become dominated, which leads to intensified fluorescence. Similarly, aggregation can also block the free intramolecular vibration for some AIEgens (tetrahydro-bidibenzo-annulenylidene (THBA)) and modulate the relaxation non-radiative decay pathway to radiative pathways (Figure 1.2).[49, 50] The discovery and development of AIE fluorogens have provided great opportunities and showed unique

potentials in molecular sensing, protein detection, cellular imaging, bacteria imaging, and tissue imaging. Most recently, some AIEgens also have been found to be able to efficiently generate reactive oxygen species (ROS).[51,52] In addition, opposite to traditional photosensitizers (PSs), AIEgens showed efficient ROS generation in aggregate state, making them promising in photodynamic therapy (PDT) over conventional photosensitizers (PSs), which further expanded their biological applications.

This intensified fluorescence once in aggregated state inspired the design of various light-up probes based on binding or cleavage induced emission for detection of wide ranges of molecules, proteins or biological processes. Mostly important, it also means that the AIE feature of the novel class of fluorogens can be fully utilized by using their highly emissive aggregates to form NPs with ultrahigh brightness as efficient imaging contrasts for bio-imaging applications with much better imaging resolution and biocompatibility.

1.3 Synthesis of AIE Dots

Since its discovery by Tang et al, the research fields of AIEgens have been rapidly developed and attracted large number of researchers due to the unique and amazing merits of AIEgens. Up to now, various approaches and strategies have been reported for fabrication of AIE dots for different biological applications.[39, 53] In general, the synthesis of AIE dots involves the transferring molecularly dissolved AIE molecules from organic solvent to aggregates in water phase with stabilized morphology and size. Based on the material difference to synthesize AIE dots, the methods have been classified into two groups: silica AIE dots and organic AIE dots.

1.3.1 Silica AIE Dots

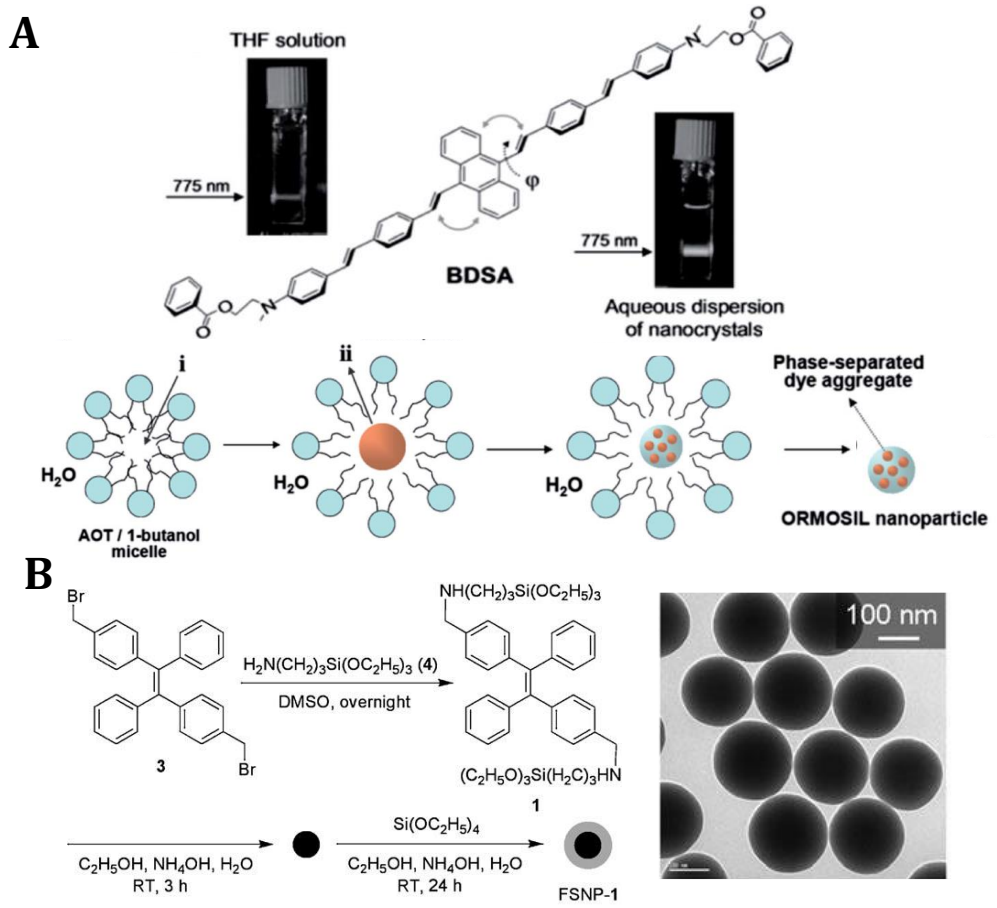

Figure 1.3. Schematic illustration of Silica AIE dots formations: A) ORMOSIL dots encapsulating BDSA.[53] B) TPE-containing fluorescent silica AIE dots.[56] Copyright 2014 Royal Society of Chemistry and 2010 Wiley-VCH.

The pioneer work of silica AIE dots is reported by Prasad *et al.*[54] In 2007, Prasad's group reported the encapsulation of a new AIEgen, 9,10-bis[4-(4-aminostyryl)styryl]anthracene derivative (BDSA) with organically modified silica (ORMOSIL) NPs for two-photon fluorescence imaging. This BDSA fluorogen showed dimed two-photon fluorescence when molecularly dissolved but was induced to bright two-photon emission in aggregate. To form the silica AIE dots, *N*-Methyl-2-pyrrolidinone (NMP) solution containing BDSA and triethoxyvinylsilane (VTES) was injected into aqueous micelle solution prepared by Aerosol OT (AOT) (Figure 1.3A). AIEgens encapsulation and ORMOSIL AIE dot formation were accomplished in the

nonpolar interior of AOT micelles in VTES sol by transient emulsification and spontaneous co-precipitation *via* solvent displacement process. The ORMOSIL AIE NPs showed excellent encapsulation performance of AIE aggregates, which showed intense fluorescence under two-photon excitation. With the presence of silanol moiety (≡ Si-OH and ≡ $Si-O^{-1}$) at surface, the silica AIE NPs are ease of surface functionalization with various targeting ligands, which was successfully demonstrated in *in vitro* two-photon imaging with low cytotoxicity. The same group also co-encapsulated the same AIEgen with a PS for photodynamic therapy.[55] The photosensitizer is indirectly excited by the energy transferred from the BDSA due to their close proximity, and this ORMOSIL AIE dots exhibited efficient *in vitro* anticancer effects by the generation of ROS under two-photon excitation.

In 2010, Tang et al. reported a new method for the fabrication of highly emissive silica AIE dots with core-shell structures by modified Stöber methods.[56] In this method, TPE was covalently conjugated with (3-aminopropyl)triethoxysilane (APS). The TPE-silica nano-cores are obtained after the sol-gel reaction in the presence of ammonium hydroxide in aqueous solution, which is further subjected to sol-gel reaction with tetraethylorthosilicate to yield FSNP-1 AIE dots with fluorescent TPE aggregates as the core and silica as the shell (Figure 1.3B). The resultant FSNP-1 dots are uniformly dispersed with tuneable sizes from 50 to 300 nm by controlling reaction conditions. The silica-AIE dots exhibit high emission, excellent colloidal stability, and low cytotoxicity, which can serve as excellent imaging regents for visualization of the cytoplasm of HeLa cells. Tang's group further introduced $–NH_2$ groups to FSNP-1 dot surfaces by using (3-aminopropyl)triethoxysilane, the resultant FSNP-1-NH_2 dots were further decorated with biotin for specific cancer cell detection and imaging.[57] A modified two-step Stöber method together with reverse micro-emulsion was also developed to covalently

immobilize of AIEgens on silica NPs.[58] Silica AIE dots with bright fluorescence and strong magnetization were further fabricated *via* surfactant-free sol–gel reaction of tetraethoxysilane and silole-functionalized siloxane in the presence of citrate-coated magnetic NPs.[59] In 2014, Wei's group reported a non-covalently encapsulation of AIEgens into silica dots.[53, 60] Instead of chemically melding AIEgens with silica precursors, octadecyltrimethoxysilane with long alkyne chain was used as the silicate precursor and structure-driving template to encapsulate AIEgens to fabricate the mono-dispersed silica AIE dots with excellent water dispersiblity, low cytotoxicity and excellent cellular internalization capability.

1.3.2 Organic AIE Dots

Organic AIE dots were mainly fabricated by polymers or oligomers encapsulation approaches. These amphiphilic polymers or oligomers tend to self-assemble into stable nano-aggregates in aqueous solution. When AIEgens were covalently linked or non-covalently mixed with these polymers, AIEgens doped NPs with bright fluorescence will be observed. Several methods have been developed to prepare these AIE dots, including self-assembly, polymerization, emulsion, and nano-precipitation. Through controlling amphiphilicity, matrix molecular weight, matrix to AIEgens ratio, and initial concentration, *et al.*, AIE dots with different sizes and properties can be fabricated to fulfil different biological applications.

1.3.2.1 Self-assembly

A typical procedure for self-assembly approach is shown in Scheme 1.1A. These AIE-containing polymers were firstly dissolved in a good organic solvent, which is miscible with the 'poor' solvent such as water. When they are transferred from the organic solvent to an excess amount of water, they tend to self-assemble to nano-

aggregates. The hydrophobic segments tend to collapse with each other to form the core, while hydrophilic segments will present as the shell to stabilize the core to form the organic dots.[61] The AIEgens can locate at the centre, terminal, or side-chains of these amphiphilic polymers or oligomers.

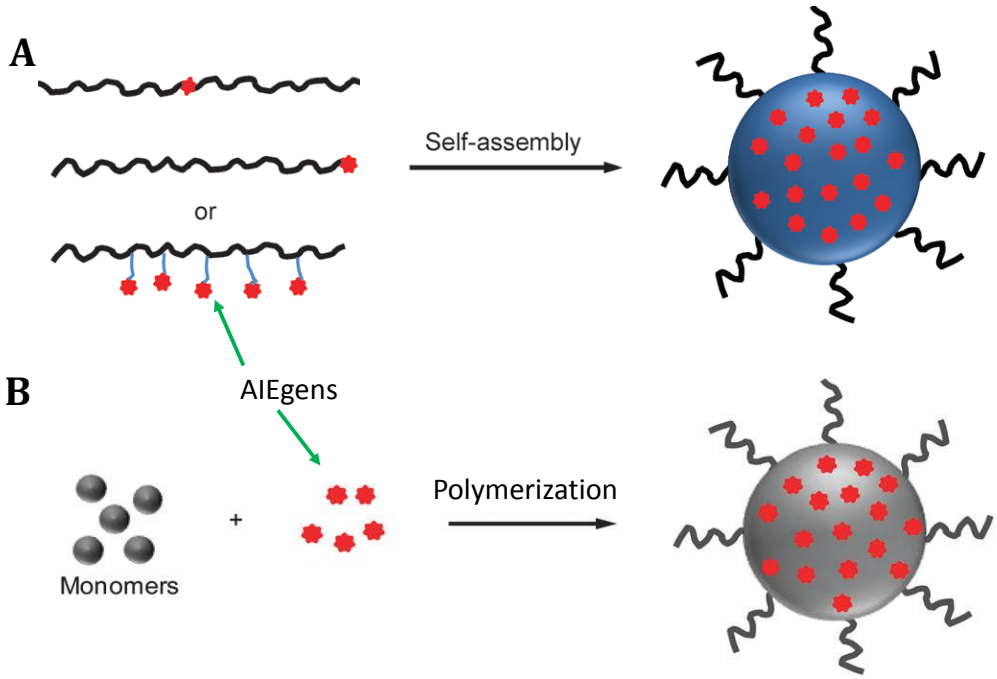

Scheme 1.1. Schematic illustration of organic AIE dots from A) self-assembly, and B) polymerization.[61] Copyright 2014 Royal Society of Chemistry.

The early works of AIE dots prepared from self-assembly were reported by Tang et al.[62, 63] In this demonstration, they synthesized a TPE derivate, 1-[4-(isothiocyanatomethyl)phenyl]-1,2,2-triphenylethene (TPE-ITC), which is also AIE-active, where its fluorescence intensity in THF/water mixture (water fraction of 90%) is ~36200-fold stronger than that in THF solution. TPE-ITC is then linked to the side chains of Chitosan (CS) to yield TPE-CS (Figure 1.4A). They also labeled CS side chains with fluorescein, a typical ACQ unit, to yield FCS for comparison. The solid powders of TPE-CS showed bright greenish-blue light, which is increased with the degree of labelling (DL) of TPE, while FCS at low DL showed yellow light, but the emission is drastically decreased with increased DL due to the ACQ effect (Figure

1.4A). The TPE-CS dots were synthesized by ionic gelation method, where sodium tripolyphosphate solution was dropwisely added into TPE-CS acetic acid aqueous solution under constant stirring. The TPE-CS dots were formed *via* the crosslinking of the amino groups on chitosan and the phosphate group on tripolyphosphate. The obtained AIE dots are spherical in shape and well dispersed in water with size of 170 nm. The suspension of TPE-CS dots emit strong blue fluorescence under laser illumination due to the AIE feature of TPE moiety. The TPE-CS dots were ready for cellular internalization and showed excellent cellular retention without contaminating co-cultured other cell lines.

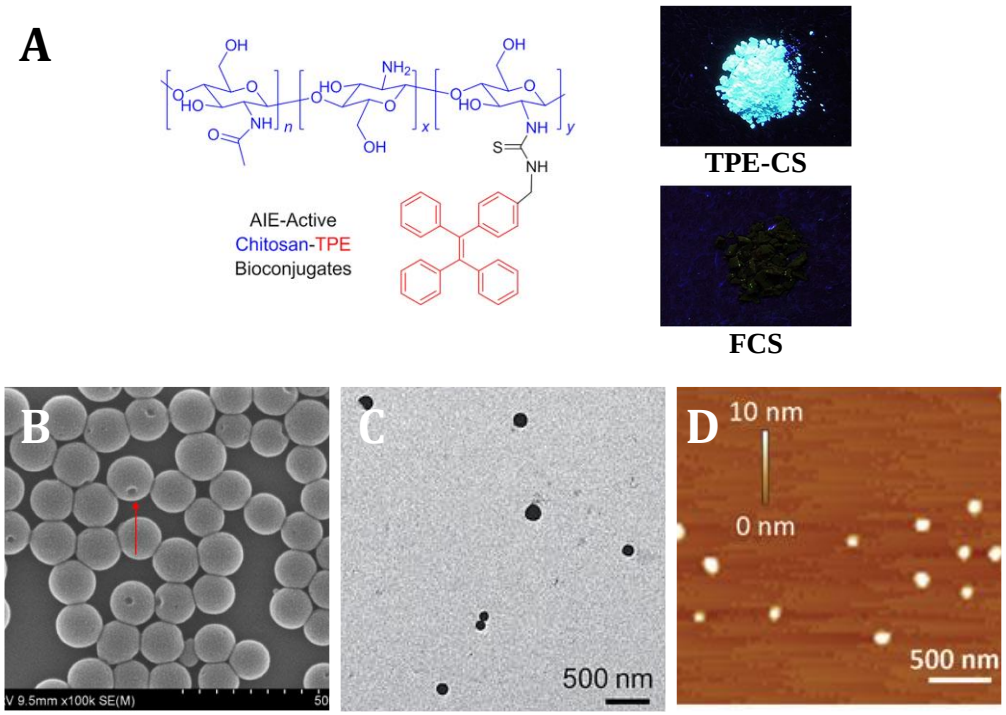

Figure 1.4. A) Chemical structures of TPE-CS, and the photograph of TPE-CS and FCS under light irradiation. B) SEM image of PTPEE dots. C) TEM image of Net-TPS-DMA dots. D) AFM image of cRGD-TPE-Pt-DOX dots.

In 2014, Xu and co-authors reported a new self-assembly approach to prepare AIE dots.[64] In this approach, AIE-based polymers were firstly prepared by the reversible addition–fragmentation chain transfer (RAFT) polymerization of (2-(4-

vinylphenyl)ethene-1,1,2-triyl)tribenzene (TPEE). The resultant poly[(2-(4-vinylphenyl)ethene-1,1,2-triyl)tribenzene] (PTPEE) showed typical AIE characteristics. To prepare the PTPEE dots, the polymer is transferred from THF to water under sonication to induce the self-assembly process to form AIE dots. Scanning electron microscope (SEM) was used to study the morphology of PTPEE dots, as shown in Figure 1.4B, these dots are spherical particles with one dimple observed on each particle. In addition, dot sizes can be controlled by the speed and sequence of THF addition. These AIE dots are very stable, no precipitation is observed after storage in solution for one week. Wei el al also reported the fabrication of AIE dots based on the similar concept of polymerization followed by self-assembly.[65, 66] Through controlling the degree of polymerization, the AIE dots size can be fine-tuned from 100 to 500 nm.[67]

Besides attaching AIEgens to polymers, modifying AIEgens with small hydrophilic ligands can also lead to self-assemble to form AIE dots.[68, 69] In 2014, Liu et al attached polyethyleneimine (PEI) to TPS, which was further modified with 2,3-dimethylmaleic anhydride (DMA) to afford Net-TPS-PEI-DMA. The Net-TPS-PEI-DMA showed particle size around 170 nm and spherical shapes as observed by transmission electron microscope (TEM) image (Figure 1.4C). The same group also attached two anticancer drugs, doxorubicin (DOX) and cisplatin (Pt) and targeting moiety cRGD to TPE, and the resultant cRGD-TPE-Pt-DOX can self-assembly into AIE dots with size around 120 nm as observed by atomic force microscopy (AFM) image (Figure 1.4D).

1.3.2.2 Polymerization

Utilizing the polymerization method to fabricate AIE dots, it requires the monomers and AIEgens are well dispersed into stable oil droplets in the aqueous solution, and hence the polymerization and self-assembly processes will happen

simultaneously (Scheme 1.1B) to afford the AIE dots after organic solvent evaporation. In 2014, Wei and co-workers reported the emulsion polymerization method for AIE dots fabrications.[70] In this method, they synthesize the polymerizable AIE dyes (**PhE**) with double bond as the end functional groups. **PhE** and two other monomers acrylic acid (AA) and styrene (St) were well dispersed as small oil droplets in organic solvent/water mixture in the presence of emulsifier sodium dodecyl benzene sulfonate (SDBS). The addition of APS as the initiator starts the polymerization to yield PhE-Pst dots. During the emulsion polymerization, hydrophobic **PhE** and St segments aggregated as the core while the hydrophilic AA segments served as the protective shell. PhE-Pst dots exhibited uniform spherical shape with size around 400 nm and zeta potential of -45 mV. The PhE-Pst dots exhibited strong orange emission under UV lamp illumination, which were able to label HeLa cells with excellent biocompatibility.

1.3.2.3 Polymer Encapsulation

Silica AIE dots are suffering from the non-biodegradable nature, while self-assembly and polymerization approaches required tedious chemical synthetic work. In this regard, encapsulation of AIEgens by polymeric matrices seems to be a promising approach for fabrication of AIE dots, which not only helps to minimize the inference from surrounding environment, but also exhibits excellent biocompatibility. Up to now, various polymeric matrices, including block-copolymers, lipids, and proteins have been reported for AIE dots fabrication.

The early work of polymer encapsulated AIE dots was reported by Jen *et al.*[71] In their demonstration, three block copolymers, poly(ethylene glycol)-bpoly(e-caprolactone) (PEG-*b*-PCL), poly(ethyleneglycol)-b-poly(styrene) (PEG-*b*-PS), and poly(methacrylic acid)-b-poly(styrene) (PMAA-*b*-PS) were used as the encapsulation

matrices, while HPS was selected as the fluorescent AIE core. Upon transferring them from organic solvent to water, the block copolymers will form micelles, where the core will act at the reservoir for AIEgen aggregates, and the hydrophilic parts will act as the brush-like protective corona to stabilize the AIE micelles. The larger hydrophobic segments of the polymeric matrix and the higher loading ratio of AIEgens will lead to increased AIE micelle sizes. In addition, the quantum yield of HPS loaded PMAA-*b*-PS micelles can reach to 62% at HPS loading ratio of 30%, which is much higher than that of HPS aggregates in poor solvent (22%), due to that the micelle encapsulation not only confines the spatial movement of HPS aggregates, but also prevents the direct contact of AIEgens with water media. In addition, they also demonstrated that the co-encapsulation of HPS and bis(4-(*N*-(1-naphthyl) phenylamino)-phenyl)fumaronitrile (NPAFN) will result in efficient Förster resonance energy transfer (FRET) from HPS to NPAFN, leading to largely increased red fluorescence without affecting the size and surface morphology of the micelles. However, the instability of micelle in aqueous solution still remain a big challenge for long term storage and use of AIE micelles.

In 2011, Liu *et al*. reported a modified nano-precipitation method for the fabrication compact AIE dots.[72] Block copolymer lipid-PEG was chosen as the encapsulation matrix. To form AIE dots, the THF mixture of lipid-PEG and AIEgens was added into MilliQ water and followed by the ultrasound sonication. Instead of forming micelles, hydrophobic lipid segments intertwine with AIEgens to form the compact core while PEG segments extend outside towards water phase to stabilize AIE dots. Through controlling the length of PEG segments, the AIE dot sizes can be controlled from 30 nm to 100 nm. AIE dot surfaces can also be rendered with different functional groups through the modification of the end groups of PEG chain.

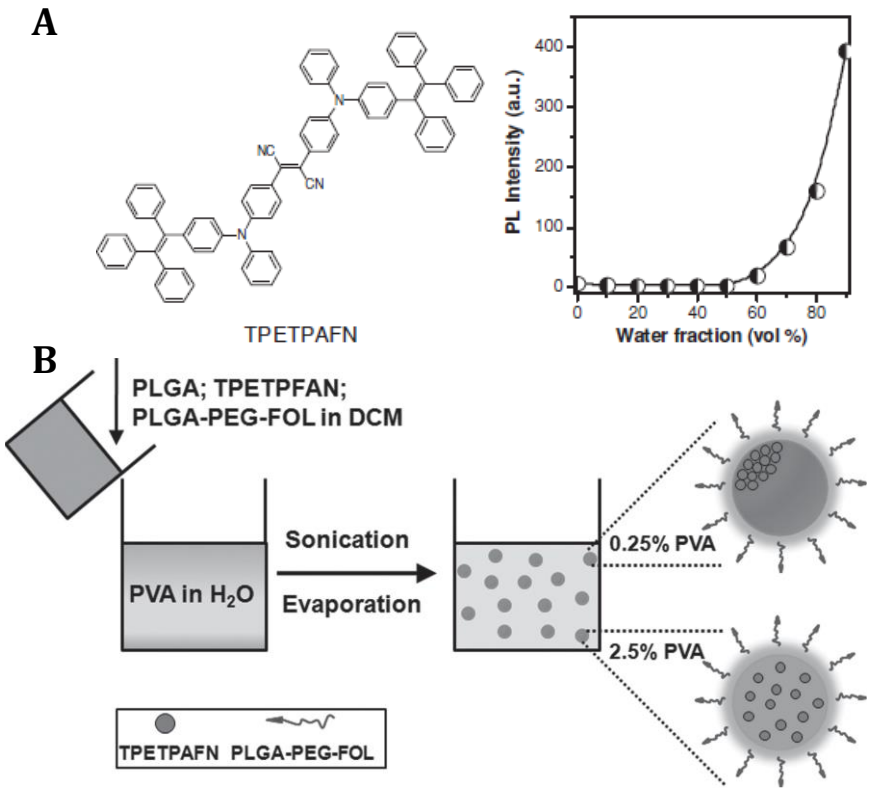

Scheme 1.2. A) Chemical structure of TPETPAFN and its emission intensity changes in THF/water mixture. B) Schematic illustration of the fabrication of PLGA-PEG-Fol AIE dots eccentrically or homogeneously loaded with TPETPAFN.[73] Copyright 2012 Wiley-VCH.

In 2012, Liu's group reported the emulsion approach to fabricate poly(DL-lactide-*co*-glycolide) (PLGA) loaded AIE dots for targeted cellular imaging.[73] In this method, dichloromethane (DCM) that is immiscible with water was chosen as the organic solvent, and polyvinyl alcohol (PVA) was selected as the emulsifier. 2,3-Bis(4-(phenyl(4-(1,2,2-triphenylvinyl)phenyl)amino)-phenyl)fumaronitrile (TPETPAFN) with almost zero fluorescence in THF but largely intensified red fluorescence in aggregates was used as the AIEgen (Scheme 1.2A). To fabricate the AIE dots, TPETPAFN, PLGA, and poly([lactide-*co*-glycolide]-*b*-folate[ethylene glycol]) (PLGA-PEG-folate) were fully dissolved in DCM solution, which was further poured into aqueous solution containing PVA as the emulsifier, followed by ultrasound sonication (Scheme 1.2B). The size of PLGA AIE dots is around 200 nm with high uniform distribution. They also demonstrated that TPETPAFN molecules tend to

eccentrically aggregate at one side of the PLGA dots prepared from low PVA concentration (0.25%), while homogeneous distribution of TPETPAFN was observed for PLGA dots prepared from high PVA concentration (2.5%). In addition, this eccentric aggregation showed higher fluorescence quantum yield (32%) over homogeneous distribution (24%), which was utilized for cell imaging applications.

In 2012, Liu's group reported the encapsulation AIEgens into protein dots for *in vitro* and *in vivo* bio-imaging.[74] The new AIEgen, 2-(2,6-bis((*E*)-4-(phenyl(4'-(1,2,2-triphenylvinyl)-[1,1'-biphenyl]-4-l)amino)styryl)-4*H*-pyran-4-ylidene)malononitrile (TPETPADCM) was encapsulated by bovine serum albumin (BSA) protein. To form BSA dots, the THF solution of TPETPADCM was added into BSA aqueous solution. Upon mixing, TPETPADCM aggregated and entangled at the hydrophobic parts of BSA, and the BSA will gradually undergo phase separation and self-assembly to form BSA dots, which were further stabilized *via* cross-linking by glutaraldehyde. The BSA dots showed uniformly distributed spheres with size around 100 nm and high fluorescence, suitable for bio-imaging applications.

Hereafter, various polymeric matrices with different hydrophobicity have been developed for encapsulation of AIE aggregates into AIE dots with amendable surface functional groups.[75-77] This non-covalent encapsulation of AIEgens does not require the chemical modification of AIEgens, and the rapid development of polymer materials and nanotechnology also further expanded the fabrication methods of AIE dots.

1.4 AIE Dots for Biological Applications

Together with the rapid and extensive development of AIE dots, their biological applications have been widely investigated and reported by different researchers. Different from conventional fluorogen based NPs, which often result in quenched

fluorescence due to the notorious ACQ phenomenon, AIE dots with high brightness, good photostability, excellent biocompatibility and ease of surface functionalization have shown their merits and potentials in different biological applications such as *in vitro* imaging, *in vivo* imaging and therapy.

1.4.1 *In Vitro* Imaging

The early application of AIE dots in bio-imaging was mainly focused on non-targeted *in vitro* cellular imaging. For example, in 2010, Tang and co-authors reported the fabrication of fluorescent silica NPs (FSNPs) with controllable size from 50 to 300 nm. The fluorescence quantum yields of FSNPs increase along with the increase in AIEgens loading percentage. The obtained FSNPs could nonspecific internalize into living HeLa cells through endocytosis where FSNPs were enclosed by membrane to form small vesicles first, followed by internalization and releasing from endosomes and lysosomes to cytoplasm (Figure 1.5A).[56] Another type of AIE dots prepared by polymer encapsulation also has been studied in non-targeted cellular imaging by Jen et al.[71] In this contribution, HPS-encapsulating PMAA-*b*-PS micelles showed much higher fluorescence in RAW cells while bulk HPS aggregates without block copolymer encapsulation did not show significant internalization into cells. These studies clearly demonstrated the importance of polymer encapsulation in facilitating the stable dispersion of AIE aggregates in biological environment and the enhanced cellular internalization. This study also revealed that the hydrophobicity of the chosen block copolymer matrix also plays importance roles in determining the brightness and the cellular uptake.

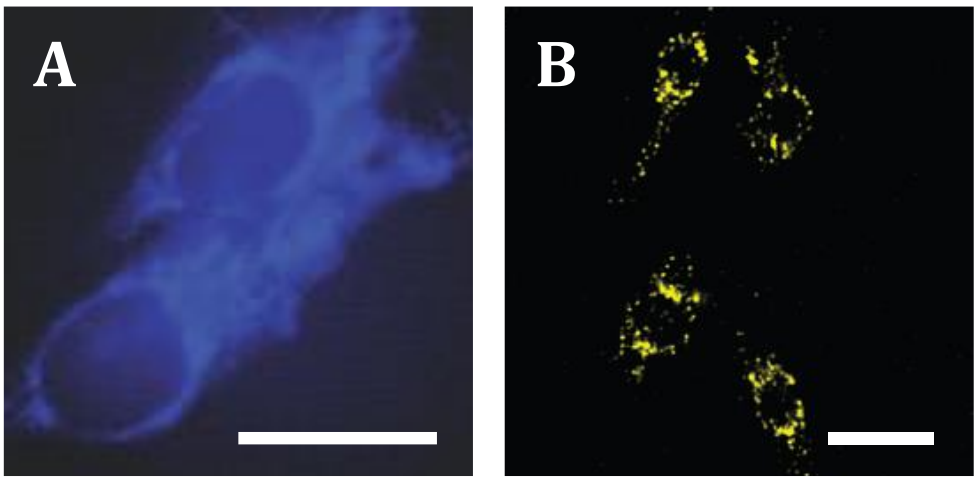

Figure 1.5. A) Fluorescence image of HeLa cells stained by FSNPs at TPE concentration of 6 μM.[56] B) Two-photon excited fluorescence image of MCF-7 stained by folate functionalized AIE dots.[72] All the images share the same scale bar of 20 μm. Copyright 2010 Wiley-VCH and 2011 Royal Society of Chemistry.

Besides nonspecific cellular imaging, the AIE dot surfaces were further functionalized with targeting ligands such as folate or targeting peptides to enhance the cellular uptake towards specific cells. One of the particular examples of targeted cellular imaging for AIE dots is demonstrated by Liu's groups in 2011.[72] The AIEgen with high two-photon absorption (TPA) was encapsulated by 1,2-distearoyl-sn-glycero-3-phosphoethanolamine-N-[folate(polyethylene glycol)-2000] (DSPE-PEG-Folate), the TPA cross section is over 500 GM for the resultant AIE dots, which is higher than most water-soluble TPA materials. After 2 h incubation, bright fluorescence was observed in the cytoplasm of MCF-7 cells with overexpressed folate receptor (Figure 1.5B), while only very weak fluorescence was detectable from NIH-3T3 fibroblast cells due to the lack of folate receptor at cell surface. In addition, the AIE dots showed low cytotoxicity with ~100% cell viability after 72 h incubation. Later in 2012, the same groups further studied the uptake mechanism of DSPE-PEG-Folate encapsulated AIE dots.[78] Blocking the folate receptor by free folic acid or lowering the incubation temperature to 4 ℃ will largely suppress the cellular uptake of AIE-Folate dots, confirming the receptor-mediate endocytosis pathway for FA decorated AIE dots. A

series of inhibitors were further applied, which revealed that uptake of AIE-Folate dots is mainly involved in caveolae-mediated endocytosis while clathrin-mediate endocytosis and micropinocytotsis are not involved. Tang and co-authors also reported targeted cellular imaging towards cancer cells with biotin-receptor overexpression using biotin decorated silica AIE dots.[57]

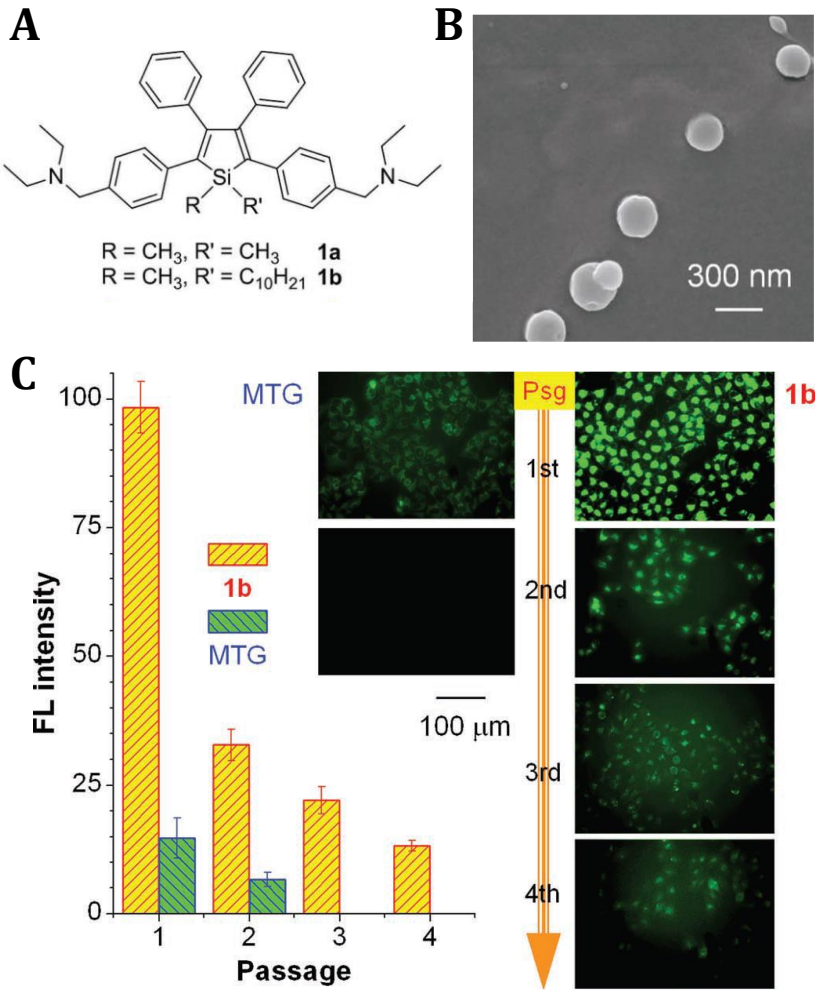

Figure 1.6. A) Chemical structures of **1a** and **1b**, b) SEM image of **1a** aggregates formed in THF/water mixture. C) Fluorescence intensities and images of HeLa cell stained by 5 μM of **1b** and 200 nM MTG at different passages (Psg).[79] Copyright 2012 Wiley-VCH.

These optical properties such as high bright, good photostability, low cytotoxicity and excellent cellular retention make AIE dots an excellent cell tracker to visualize complex biological processes such as proliferation, division, and metastasis of cancer cells. The pioneer work of cell tracing with AIE dots was reported by Tang *et al*. In 2011, they reported the cytophilic silole aggregates (**1a** and **1b**) (Figure 1.6A)

for tracing the activity of HeLa cells over four passages.[79] The silole derivatives are able to self-assemble into dots with size around 300 nm (Figures 1.6B) and quantum yield of ~40%. This **1b** AIE aggregates showed excellent biocompatibility with ~100% cell viability even after incubation at 5 μM, while incubation HeLa cells with the commercial available MitoTracker Green (MTG) at 2 μM showed damaged mitochondria structures. In addition, the fluorescence intensity of HeLa cells increases with the **1b** concentration, while using concentrated MTG does not guarantee the high brightness. The **1b** AIE dots inside HeLa cells firmly retained inside the cytoplasm during the cell proliferation and can be passed to daughter cells over four passages, while the MTG fluorescence was not detectable even in the 2nd passage (Figure 1.6C).

AIE dots with longer cell tracing time were further developed by Liu's group.[75, 76] The DSPE-PEG loaded AIE dots were surface functionalized with cell penetration peptide derived from HIV-1 transactivator of transcription (Tat) protein. The Tat modified AIE dots showed much improved cellular uptake and retention, which can track the cell activity over 10 passages. While commercial QD tracker can only track cell activity for 4 passages. Liu's group also reported the dual colour cell tracing,[77] two AIE dots with distinct emission spectra can be simultaneously excited by single-wavelength. Through labelling cells with different emission colours, the cellular interactions during cancer metastasis can be clearly visualized.

1.4.2 *In Vivo* Imaging

The development of AIEgens in the far-red/near-infrared (FR/NIR) regions further makes them the attractive reagents for *in vivo* imaging due to their high penetration depth, low background signal interference and low photodamage to biological species at the low-energy NIR region.

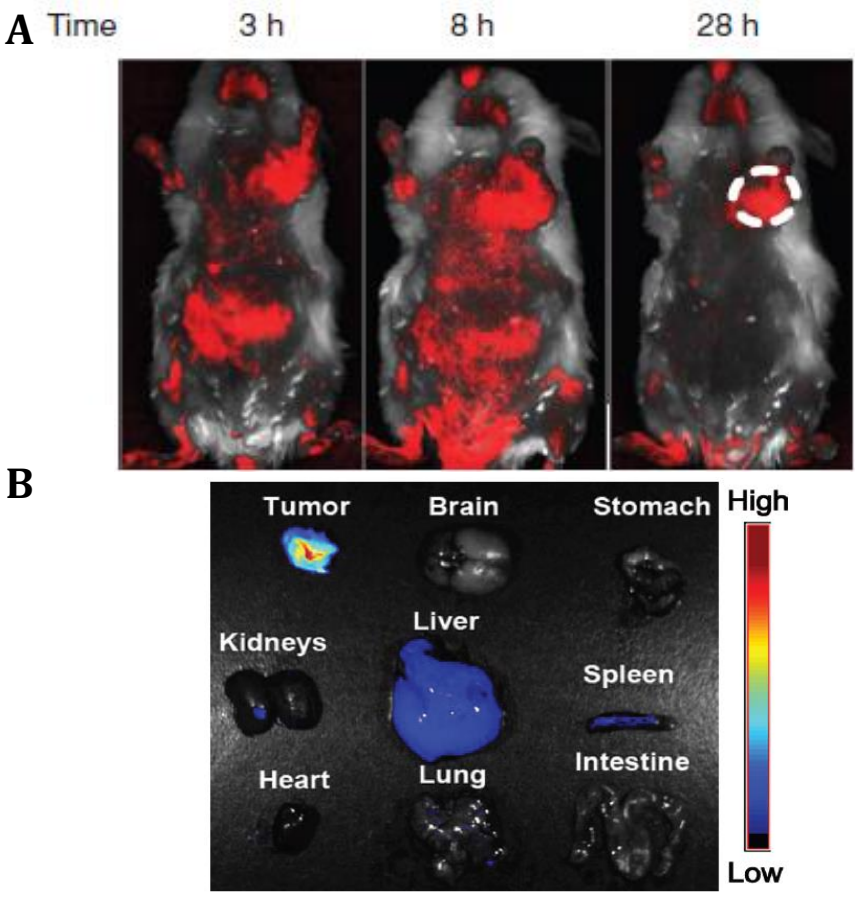

Figure 1.7. A) *In vivo* non-invasive fluorescence imaging of H22-tumor-bearing mice after intravenous injection of TPETPADCM loaded BSA dots. B) *Ex vivo* fluorescence imaging on tumor tissue and major organs of mice treated with BSA dots.[74] Copyright 2012 Wiley-VCH.

The early example of AIE dots for *in vivo* imaging was demonstrated by Liu and Tang *et al.*[74] They encapsulated TPETPADCM into BSA dots. Possessing the twisted intramolecular charge transfer (TICT) phenomenon and AIE feature of TPETPADCM, the obtained BSA dots showed bright red fluorescence centred at 668 nm in aqueous solution. Increasing TPETPADCM loading ratio results in increased quantum yield which reaches the maximum of 12.5%. The *in vivo* tumour imaging by BSA AIE dots was examined on Murine hepatoma-22 (H_{22})-transplanted tumor-bearing ICR mice through intravenous injection. Intense red fluorescence in the tumour tissue was observed at all the imaging times, and at 28 h post-injection, strong fluorescence in tumour in sharp contrast to weak fluorescence in other part indicated the promising performance of AIE dots for cancer diagnosis (Figure 1.7A). The tumour accumulation

of BSA AIE dots is attributed to the passive tumour targeting EPR effects originated from the uniform dot size of 100 nm. The occurrence and disappearance of fluorescence in the liver and abdomen area also indicated that BSA AIE dots can be uptaken by the reticuloendothelial system (RES) organs, and followed by body clearance through biliary pathway. This tumour diagnosis was also demonstrated using *ex vivo* fluorescence imaging, where tumour tissue provided the highest fluorescence as compared to other major organs of the scarified mouse (Figure 1.7B). The same group further co-encapsulated conjugated polymers, poly[9,9-bis(2-(2-(2-methoxyethoxy)ethoxy)ethyl)fluorenyldivinylene] (PFV) and TPETPADCM into the same BSA dots to utilize the large molecular absorption of PFV and FRET to enhance the FR/NIR brightness of the AIE dots for *in vivo* tumour imaging.[80]

The excellent biocompatibility and *in vitro* cell tracing performance of AIE dots also inspired the *in vivo* tracing applications.[76] To demonstrate this, Liu *et al.* encapsulated TPETPAFN by DSPE-PEG to form AIE dots to track the *in vivo* tumour growth (Figure 1.8A). The formed AIE dots showed high brightness with quantum yield of 24%, and uniform size of 30 nm. Under single nanoparticle fluorescence imaging, the AIE dots showed average 1.18×10^6 counts of photon emitted per 100 s, which is 4-fold higher than QD655 tracker. TPETPAFN dots showed excellent photostability under continuous laser scanning. In addition, different from QDs, TPETPAFN AIE dots showed stable fluorescence without intermittency (Figure 1.8B). The AIE dots labelled C6 glioma cells were subcutaneously injected into the mice flank. The bright red fluorescence originated from AIE dots clearly indicates the location and growth of tumour cells in mice body, which is traceable up to 21 day (Figure 1.8C), while in the parallel experiment, QD tracker 655 can only trace the tumour growth for 7 day (Figure 1.8D). This report demonstrated the superior advantage of AIE dots *in vivo* tumour

tracing. In a more recent study, Liu et al. further demonstrated AIE dots for precisely long-term tracking of adipose-derived stem cells (ADSCs) and monitoring their regenerative capability in an ischemic hind limb bearing mouse model.[81]

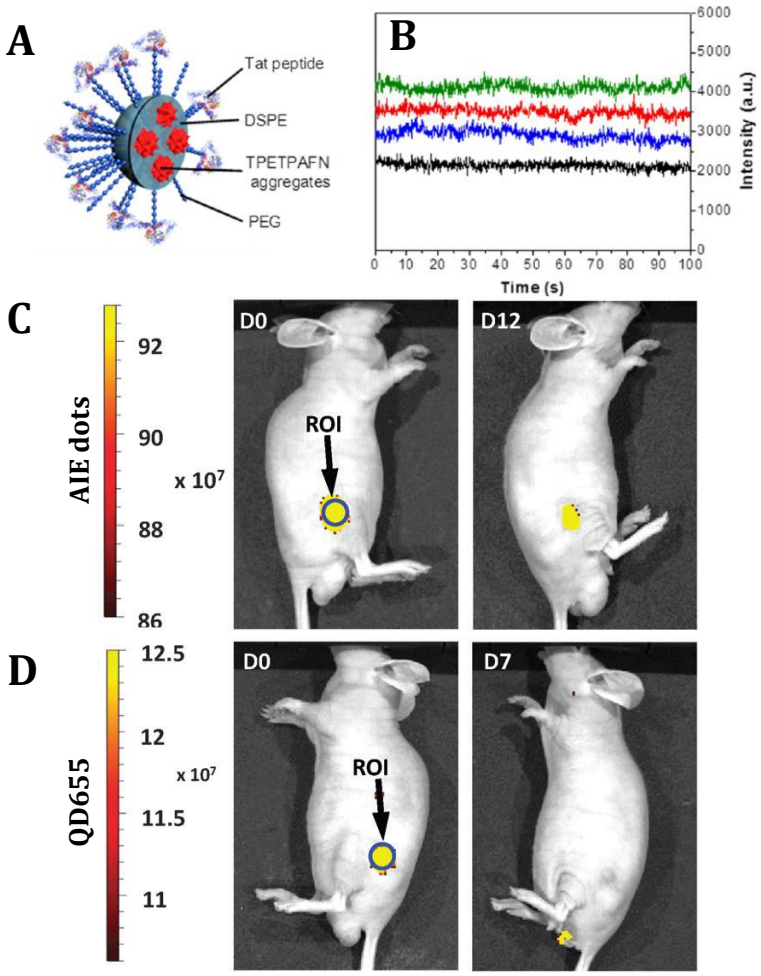

Figure 1.8. A) Schematic illustration of AIE dots. B) Fluorescence time-traces of four individual AIE dots with different brightness levels. C) *In vivo* fluorescence imaging of the mouse subcutaneously injected with 1×10^6 of C6 glioma cells labelled with C) AIE dots, or D) QD655.[76] Copyright 2013 Nature Publishing Group.

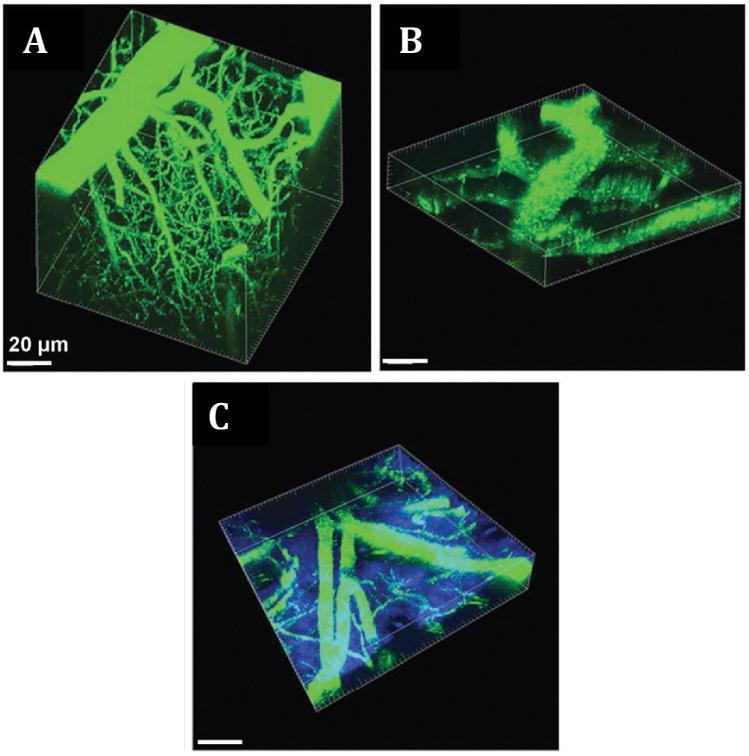

Figure 1.9. 3D reconstructed two-photon fluorescence images of blood vessels in A) brain (0–425 μm), B) bone marrow (0–108 μm), and C) mouse ear skin (0–132 μm) from the mouse injected with BTPEBT AIE dots. All images share the same scale bar of 20 μm.[82] Copyright 2013 Wiley-VCH.

In addition to one-photon *in vivo* imaging, the potential of AIE dots as two-photon fluorescence imaging (TPFI) reagents also has been demonstrated. Liu *et al.* reported the AIE dots encapsulating 4,7-bis[4-(1,2,2-triphenylvinyl)phenyl]benzo-2,1,3-thiadiazole (BTPEBT) for intravital TPFI of blood vessel.[82] The fabricated AIE dots showed high quantum yield of 62%, and a high TPA cross section of 1.02×10^5 GM per dot at 820 nm which is much higher than most commercial available TPFI reagents. The AIE dots are further applied in the real-time blood vascular imaging in live mice. With the bright green emission of BTPEBT AIE dots under two-photon excitation, these small capillaries in the pia mater, microvasculature deep in the brain, as well as these blood vascular in skull bone marrow and ear skin of mouse can be clearly observed with high resolution (Figure 1.9). Without shown obvious toxicity to mice, these results demonstrated that AIE dots can be used as safety contrast agents for

in vivo visualization not only tumour growth, stem cell regeneration, but also blood vessel inside various organs.

1.4.3 Theranostic Applications

In addition to imaging, the simultaneous utilization of AIE dots in cancer therapy and biological imaging also has been reported in recent years. The pioneer work was demonstrated by Prasad *et al.*. In 2007, Prasad's reported the BDSA and 2-devinyl-2-(1-hexyloxyethyl)pyropheophorbide (HPPH) co-encapsulated ORMOSIL dots for PDT.[55] PDT utilize PSs to produce reactive oxygen species (ROS) that are toxic to tumour in the presence of oxygen and light has been served as a promising approach for cancer therapy.[83] The size of the co-encapsulated ORMOSIL dots is less than 30 nm, and the fluorescence spectrum of BDSA overlaps well with the absorption spectrum of HPPH, which ensures the efficient intra-particle FRET between BDSA and HPPH. Upon two-photon excitation, the up-converting energy of NIR light absorbed by BDSA can be efficiently transferred to HPPH, which resulted in enhanced singlet oxygen generation for photodynamic cancer therapy. The two-photon excitation at NIR region also ensures the deep tissue penetration, improving the treatment of deeper tumours. However, the conventional PSs still suffered from ACQ effect, which leads to largely decreased ROS production at high concentration or in aggregates, which largely compromises the PDT efficiency.[84-86] Other silica AIE dots also has been reported for cancer therapy. In 2013, Wei et al synthesized the fluorescent mesoporous silica AIE dots using cationic surfactant cetyltrimethyl ammonium bromide (CTAB) as the structure-directed template.[60] Since CATA is a broad-spectrum antiseptic agents for tumor treatment, the resultant mesoporous silica AIE dots can also serve as an efficient imaging and anticancer reagents for visualizing and killing of cancer cells.

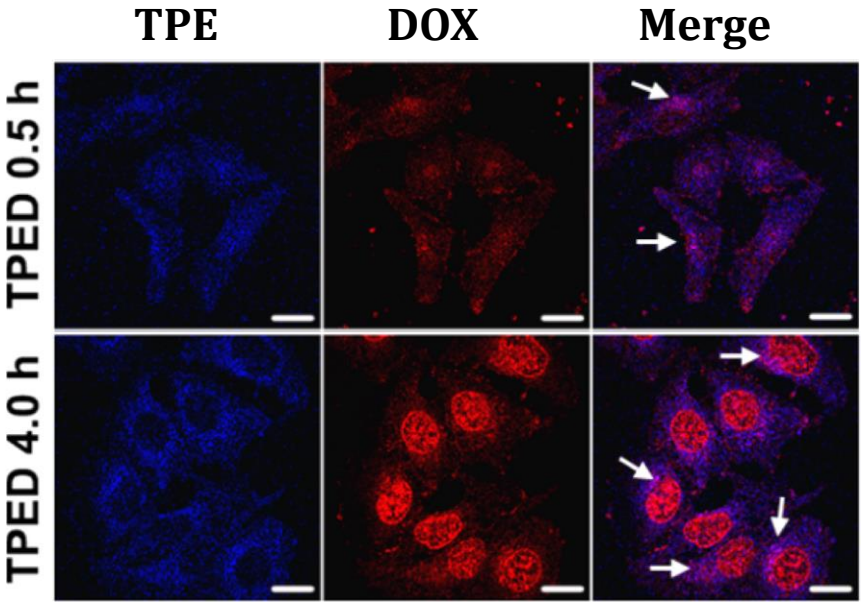

Figure 1.10. Confocal fluorescence images of the distribution of TPED (TPE-mPEG 75 μM and DOX 5 μM) in MCF-7 cancer cells with different incubation time. All the images share the same scale bar of 20 μm.[87] Copyright 2014 American Chemistry Society.

In 2014, Liang and Zou *et al.* reported the imaging of intracellular anticancer drug delivery using AIE micelles.[87] In this contribution, TPE was conjugated with a hydrophilic arm, amino-methoxypolyethylene glycol ($mPEG_{2000}$−NH_2) to yield TPE-mPEG. Due to the amphiphilic chemical structure, TPE-mPEG is able to self-assemble into micelles (TPEM) in aqueous solution. Benefiting from AIE feature of TPE, these 30 nm micelles are able to emit strong blue fluorescence under laser excitation, and they exhibited much high photostability as compared to fluorescein isothiocyanate (FITC), a traditional ACQ fluorogen. These TPE micelles are further utilized as the carriers for intracellular delivery of DOX, a commonly used anticancer drug. The DOX-loaded TPE micelles (TPED) were 30 nm spheres with high encapsulation efficiency (98.4%), drug loading percentage (15.4%), and good water dispersion. Upon excitation at 330 nm, the blue emission from TPE and the red emission from DOX can be observed, where these two channels should provide the opportunity for real time tracing of intracellular DOX delivery. Upon incubation MCF-7 breast cancer cells with TPED micelles for 0.5 h, the blue and red emission can be clearly observed and well

overlapped in the cytoplasm indicating that the DOX is still encapsulated in the micelles. After 4 h incubation, most of the red fluorescence is detected in the nucleus, indicating the successful release of DOX from TPED micelles to the nucleus. The increased blue and red fluorescence also indicate the increased cellular uptake of TPEM along with time (Figure 1.10). TPEM micelles showed excellent biocompatibility where almost 100% cell viability was observed at TPEM concentration of 0.1 mM, while loading DOX makes these micelles an efficient anticancer reagent. The decreased half maximal inhibitory concentration (IC_{50}) value of TPED (~1.2 μM) as compared to free DOX (~3.0 μM) also indicates enhanced anticancer effects by encapsulation DOX with TPE micelles due to the enhanced cellular uptake.

In a more recent study, Liu *et al.* reported a targeted AIE dots system for targeted and real-time tracking of dual-drug delivery.[69] In this demonstration, the blue emissive TPE molecule was covalently conjugated with two anticancer drugs, cisplatin (Pt) and DOX. The conjugate was further modified with cRGD peptide, and the resulted cRGD-TPE-Pt-DOX is able to selectively accumulate in cancer cells with $\alpha_3\beta_3$ integrin overexpression through receptor-mediated endocytosis. The cRGD-TPE-Pt-DOX pro-drug is able to self-assemble into nanoparticles with size around 120 nm. Due to the energy transfer from TPE to DOX, cRGD-TPE-Pt-DOX dots showed negligible blue fluorescence but intense red fluorescence under excitation. Due to the reduction regents such as ascorbic acid present in cells, both Pt and DOX will be released in the targeted cancer cells, which will disconnect the FRET pair of TPE and DOX. Hence the blue emission will be observed and intensified in the cytoplasm, and the red emission will be accumulated at the nucleus along with the drug release, providing the chance for real time tracking of DOX release. Moreover, this covalent connection of dual drugs in one

molecule also showed enhanced cancer cell killing performance with synergistic combination effects.

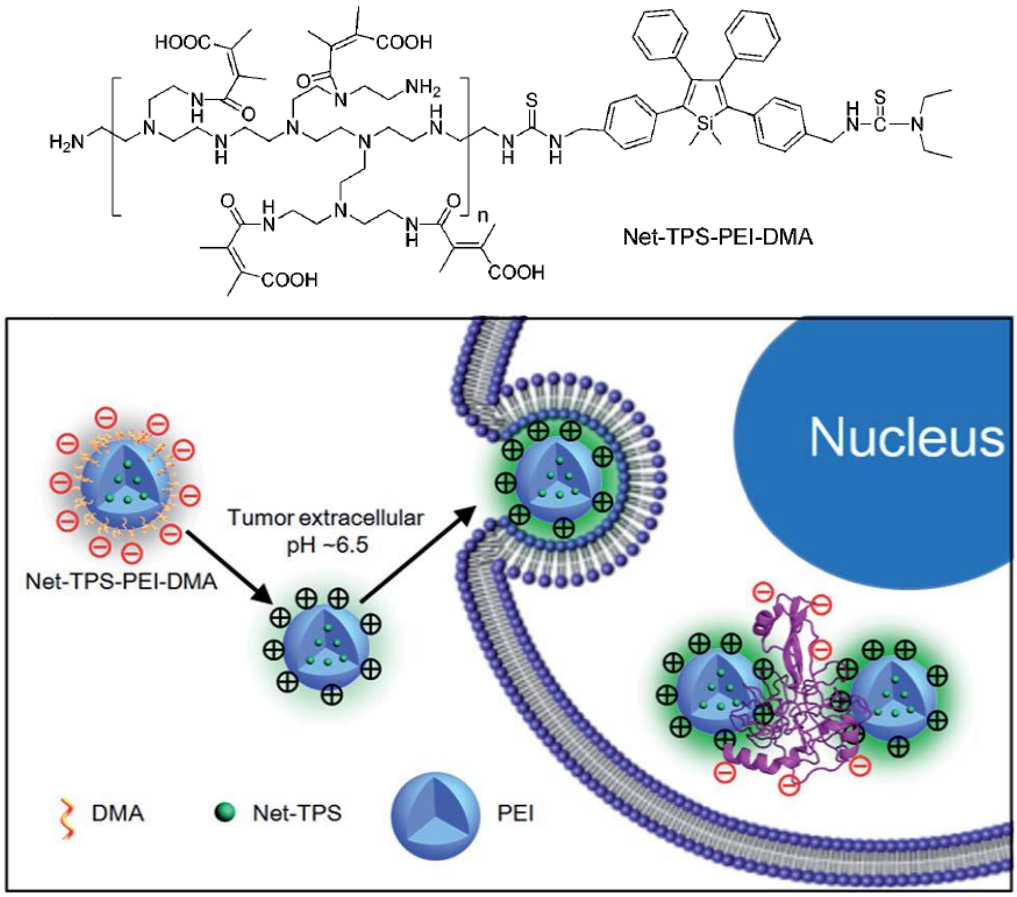

Scheme 1.3. Chemical structure of Net-TPE-PEI-DMA and the schematic illustration of it as pH-responsive light-up AIE dots for targeted imaging and selective suppression of cancer cells.[68] Copyright 2015 Royal Society of Chemistry.

In 2014, Liu and Tang *el al.* reported pH-responsive light-up AIE dots for targeted imaging and selective suppression of cancer cells.[68] The AIE probe Net-TPE-PEI-DMA is able to self-assemble into stable AIE dots with size around 170 nm as described in previous sections. The AIE dots initially exhibited negative surface with zeta potential of -10 mV. At acid microenvironment (pH_e ~6.5), the amide bound between the amine groups on PEI and DMA will be cleaved, which will result in Net-TPS-PEI NPs with positive surface zeta potential of 6 mV, facilitating the cellular uptake. In addition, the C=C bonds in DMA can quench the fluorescence of TPS, and the clearage of DMA in acid environmental will result in the resume of the TPS

fluorescence. Since tumour tissue possesses acidic extracellular microenvironment, the Net-TPS-PEI-DMA severed as a pH-responsive light up probe for *in vivo* targeted imaging of cancer cells (Scheme 1.3). In addition, the surface charge switch of AIE dots showed significant cytotoxicity to cancer cells, revealing the anticancer effects of this kind of AIE dots.

1.5 Research Objectives

As a novel generation of fluorescence materials, the discovery and development of AIEgens have inspired the innovation of molecular probes and NPs with AIE characteristics for biological sensing, detection, imaging, and theranostic applications. As compared to AIE-based small molecular probes, the fabrication of AIE dots that could fully utilize its largely enhanced bright fluorescence in the aggregate state is a more general and feasible approach for imaging related biological applications, which has just taken-off. The optical and physical properties of AIE dots can be precisely controlled *via* the chemical structure modification of AIEgens and different dot fabrication strategies, which bestow AIE dots promising potentials to fulfil these requirements in various biological applications. Moreover, the development of surface chemistry also facilitates the conjugation of AIE dots with different targeting moieties or biomolecules for targeted or multimodality imaging and other biological applications. However, the non-specific cellular imaging has dominated biological applications in these initial studies of AIE dots, and limited efforts have been made on the development of AIE dots with targeting capabilities, especially with subcellular organelle targeting abilities. In addition, the exploration of AIE dots in cancer therapy has been relied on other regents to provide therapeutic effects. Although several AIE probes have been reported with efficient ROS generation for photodynamic therapy (PDT),[52, 88] the applications of AIE dots inherently born with therapeutic ability still remain unexplored.

As such, this thesis aims to develop a group of highly versatile AIE dots with desired optical properties that are ready for *in vitro* and *in vivo* bio-imaging, and theranostic applications. It firstly aims to develop a general and feasible approach for synthesis of AIE dots with amendable surface functional groups. After demonstration of AIE dots in cell imaging and tracing, as well as blood vascular leakage detection, AIE dots with efficient ROS generation will be investigated, and the intracellular localization of AIE dots inside targeted cancer cells and its effects on PDT will be further evaluated.

The specific objectives of this Ph.D. thesis are summarized as follows.

1. To develop a general and feasible approach to fabricate biocompatible ultra-bright organic AIE dots with amendable surface functional group in one step through a modified nano-precipitation method using encapsulating matrix with different terminal functional groups.
2. To demonstrate the application of AIE dots in *in vitro* cell labelling and long term tracking by introducing specific ligands such as cell penetration peptide to AIE dot surface.
3. To introduce MRI regents gadolinium to AIE dot surface and use it as a dual modal toolbox for *in vivo* imaging of blood vascular leakage under inflammation and quantitatively analysis inflammation severity.
4. To apply AIE dots inherently born with bright fluorescence and efficient ROS generation capability for targeted image-guided cancer photodynamic therapy through surface modification with targeting peptide.
5. To further address the intracellular localization of AIE dots in targeted cells such as mitochondria for enhanced photodynamic therapy.

1.6 Thesis Outline

This thesis consists of six chapters. Chapter 1 provides a general research background of fluorescence bio-imaging, the progress of AIEgens in literatures and the objectives of this Ph.D. project. In Chapter 2, a general and facile strategy to fabricate colloidal stable and ultra-bright AIE dots with amendable surface functional groups is illustrated, which also provides AIE dots design and functionalization guidelines for following chapters. The as-prepared AIE dots are further functionalized with cell penetration peptides to enhance cellular uptake and cell retention, which is subsequently used for staining different types of cell lines and long term cell tracing using GFP transfection method as the benchmark. In Chapter 3, new AIE dots with bright fluorescence under two-photon excitation were synthesized, and gadolinium was further chelated onto the AIE dots surface for visualization and detection of blood vascular permeability change during inflammation or infection. The amount of gadolinium in the tissue provides the quantitative analysis of the severity of inflammation. Chapter 4 develops AIE dots with bright red fluorescence and efficient ROS production under irradiation for image-guided photodynamic therapy. The dot surface is conjugated with a specific targeting moiety, cyclic-RGD, to achieve specific discrimination and killing of transferrin overexpressed cancer cells. In Chapter 5, subsequent efforts were made to address the intracellular localization of AIE dots in targeted cells. A general strategy by introduction two different targeting moieties to one AIE dot is developed, which showed accumulation in mitochondria of targeted cancer cells. With efficient ROS production, the dual targeted AIE dots showed enhanced anticancer effects under light irradiation. Chapter 6 concludes the Ph.D. thesis and proposes recommendations for further improvement.

CHAPTER 2

GENERAL STRATEGY OF PREPARING ULTRA-BRIGHT ORGANIC DOTS WITH AGGREGATION-INDUCED EMISSION CHARACTERISTICS AS A FACILE CELL TRACKER

2.1 Introduction

During the past decades, fluorescence bioimaging has been extensively utilized in visualizing various biological species and progresses,[15-17] such as cell organelles,[89, 90] programmed cell death,[91] and cell lineage commitment,[92] Among these applications, continuous non-invasive cell tracing by fluorescence over a long period of time is pivotal to extract critical spatiotemporal cellular information of physiological displacement, translocation and the fate of cancer and stem cells. This information facilitates the understanding of cancer or stem cell development and intervention, providing insights for basic oncological researches and development of preclinical cell based therapies.[22, 93-95]

As one of the major class of fluorescent materials, green fluorescent protein (GFP) and its variants have been widely applied in cell transplantation and tracing.[18, 20, 27, 96, 97] This approach capitalizes on the cells innate machinery to produce proteins and requires the reporter gene to be transfected into the cells and subsequently translated into fluorescent proteins.[20, 21, 98, 99] However, viral transduction by integration of GFP gene into cell genome suffers from high cost and safety issues due to the introduction of random insertional mutation at integration sites.[22, 23, 25, 100] While non-viral plasmid transfection by expressing the GFP plasmid directly from the cytoplasm only works well for short-lived experiments within couples of days.[98, 101] In addition, the non-viral method presents low and cell type dependent transfection efficiencies.[24] Moreover, the time lag between GFP expression and gene introduction can result in an inconsistent and sometimes even cyclical net amount of fluorescent signal even when actual intracellular plasmid concentration is high.[26-28]. Therefore, new cell tracking methods that are able to attain reliable, stable and efficient cell labelling over a long time is highly desirable.

Direct cell labelling by organic or inorganic nanomaterials for tracing has drawn great attentions recently, which is fairly straightforward and does not involve genetic modification of the cells.[22, 93, 102-105] However, QD based cell trackers contain toxic heavy metals, while small organic molecules suffer from small Stokes' shifts, rapid photobleaching and cytoplasm leaking upon cell proliferation.[33, 106, 107] Researchers recently showed that organic nanoparticles (NPs) possess longer cellular retention time and lower exocytosis rate as compared to their discrete molecular counterparts.[107, 108] However, the notorious aggregation-caused quenching (ACQ) effects[109] of conventional organic molecules often lead to weakened or even annihilated fluorescence in NPs. We have recently reported a series of novel organic fluorophores with aggregation-induced emission (AIE) characteristics, which are highly emissive when aggregated.[42, 110-114] Based on these AIE fluorogens (AIEgens), we and others have successfully reported light-up probes for bio-sensing, detection, and imaging. Recently, several AIEgen based nanoparticles were also reported with high fluorescence, excellent photostability and biocompatibility,[72, 77, 82, 115] revealing their great potentials to overcome the obstacles possessed by the currently used cell trackers for cell tracing.

In this chapter, a facile strategy for fabrication of surface functionalized green emissive AIE dots for long-term cell tracing was developed. 4,7-Bis[4-(1,2,2-triphenylvinyl)phenyl]benzo-2,1,3-thiadiazole (BTPEBT) with strong green emission in aggregates was selected as the AIEgen core. A mixture of 1,2-distearoyl-sn-glycero-3-phosphoethanolamine-N-[methoxy(polyethylene glycol)-2000] (DSPE-PEG_{2000}) and its maleimide terminated derivative, DSPE-PEG_{2000}-Mal, was chosen as the encapsulation matrices to endow BTPEBT into AIE dots with biocompatibility and surface maleimide groups. A cell penetrating peptide derived from HIV-1 transactivator

of transcription protein (Tat) was further conjugated to the dot surface to yield AIE-Tat dots with high cellular internalization efficiency. The AIE-Tat dots show an emission maximum at 547 nm, similar to GFP, but with a high quantum yield of 63%. The AIE-Tat dots also have stable green fluorescence under different pH conditions or after long time incubation in buffer solution for over 10 days. The cell labelling performances of the AIE-Tat dots in the *in vitro* studies were compared to the classical calcium phosphate mediated pMAX-GFP transfection method under similar experimental conditions. It was found that the AIE-Tat dots have the capability to label all the tested human cell lines with ultrahigh brightness and ~100% labelling efficiencies, significantly outperforming the GFP plasmid transfection approach which shows varied and low GFP labelling efficiencies. Moreover, in the cell tracing experiment, AIE-Tat dots are capable to trace the activity of HEK293T cells for over 10 days, while pMAX-GFP can only trace the cell population for a maximum of 3 days. This successful demonstration of the AIE dots for *in vitro* long-term cell tracing offers new opportunities and bright prospects in the areas of cancer research, real-time monitoring of stem cell transplantation and other cell-based therapies.

2.2 Experimental

2.2.1 Materials

1,2-Distearoyl-sn-glycero-3-phosphoethanolamine-N-[methoxy(polyethylene glycol)-2000] (DSPE-PEG_{2000}) and 1,2-distearoyl-sn-glycero-3-phosphoethanolamine-N-[maleimide(polyethylene glycol)-2000] (DSPE-PEG_{2000}-Mal) were purchased from Avanti Polar Lipids, Inc. Qtracker® 585 cell labelling kit was purchased from Life Technologies, Invitrogen, Singapore. Fluoromount® aqueous mounting medium, Dulbecco's Modified Eagle Medium (DMEM), tetrahydrofuran (THF), 3-(4,5-dimethylthiazol-2-yl)-2,5-diphenyl tetrazolium bromide (MTT), penicillin-

streptomycin solution, fetal bovine serum (FBS) and trypsin-EDTA solution were purchased from Sigma-Aldrich. Cell penetrating peptide derived from transactivator of transcription proteins, HIV-1 Tat (49-57) with C-terminus modified with cysteine (RKKRRQRRRC), was a commercial product customized by GenicBio, China. Milli-Q water was supplied by Milli-Q Plus System (Millipore Corporation, Breford, USA).

2.2.2 Fabrication of AIE Dots

BTPEBT was synthesized by Dr. Liu Jie according to literature.[82, 116] To synthesize AIE dots, a THF solution (1 mL) containing BTPEBT (0.5 mg) and DSPE-PEG_{2000} (0.5 mg) and DSPE-PEG_{2000}-Mal (0.5 mg) was poured into water (10 mL) under sonication using a microtip probe sonicator at 12 W output (XL2000, Misonix Incorporated, NY). The mixture was further placed in dark in fume hood for THF evaporation at 600 rpm overnight. The AIE dot suspension was further purified by filtering through a 0.2 μm syringe driven filter

2.2.3 Fabrication of AIE-Tat Dots

Tat was conjugated to AIE dots surface through the efficient click reaction between the thiol group on Tat and the maleimide group on AIE dot surfaces. The AIE dots (1.8 mL) was mixed and reacted with Tat peptide (3×10^{-5} M, in DMSO). After reaction for 4 h at room temperature, the solution was dialysed against MilliQ water using membrane with cut-off of 6-8 kDa for 2 days to eliminate the excess peptide and DMSO. The AIE-Tat dots were filtered through 0.2 μm syringe filter and collected for further use.

2.2.4 Characterization

UV-vis spectra were recorded on a Shimadzu UV-1700 spectrometer. Photoluminescence (PL) spectra were recorded on a Perkin-Elmer LS 55

spectrafluorometer. Average particle size and size distribution of the samples were measured by laser light scattering (LLS) with a particle size analyser (90 Plus, Brookhaven Instruments Co. USA) at a fixed angle of 90 ° at room temperature. The morphology of the samples was studied by high resolution transmission electron microscopy (HR-TEM, JEM-2010F, JEOL, Japan).

2.2.5 Calculation of AIE Dot Concentration

Freeze-drying of the AIE-Tat dot stock solution (2 mL) yielded 0.34 mg of powders. As the AIE-Tat dots are stable in water, the density of the dot suspension could be estimated as ~1 g/cm^3. As the average size of AIE-Tat dots determined from HR-TEM is ~30 nm, the concentration of the AIE-Tat dots in stock can be calculated from the following equation:

$$\text{Total number of AIE-Tat dots in 2 mL of suspension} = \frac{\text{Total Volume of Tat-AIE dots}}{\text{Average Volume of Each dot}} = \frac{\frac{0.34\times10^{-3}\,\text{g}}{1\,\text{g/mL}}}{\frac{4}{3}\pi\times(15\times10^{-7})^3\,\text{mL}} = 2.41\times10^{13}$$

Finally, the concentration of AIE-Tat dots in stock solution was calculated as following: $[\text{AIE-Tat dots}] = \frac{\frac{2.3\times10^{13}}{6.02\times10^{23}\,\text{mol}^{-1}}}{2\times10^{-3}\,\text{L}} = 20\,\text{nM}$

2.2.6 Single Particle Fluorescence Imaging

Fluorescence imaging of individual AIE-Tat dot was performed with a custom-built Wide-Field Microscope (WFM) based on a Nikon ECLIPSE Ti-U inverted microscope frame. Light from a CW multi-line Ar ion laser (Melles Griot, CA, USA) was fiber-coupled to a Nikon TIRF attachment and focused on the back aperture of a high NA objective (Nikon TIRF Apo 100×, NA = 1.49, oil immersion). Immersion oil

(n_D = 1.4790, Cargille, USA) was added between the high NA objective and the cover slip for index matching. The luminescence was collected by the same objective. After passing through the dichroic mirror and the emission filter, the luminescence was directed onto an iXonEM+897 EMCCD camera (512 × 512 pixels, 150 nm per pixel resolution, Andor Technology, Northern Ireland) connected to the side port of the microscope. A filter set consisting of a z488/10× excitation filter, Z488RDC dichroic mirror, and HQ500LP emission filter was used for imaging. The camera was connected to a computer furbished with camera-dedicated software to control the imaging parameters, and for data acquisition. The samples were prepared by depositing a droplet of NP solutions on a glass cover slide, waiting for 30s for particles adsorption to the substrate, removing excess of liquid and drying under N_2. Fluorescence intensity time-traces were obtained by acquiring 1000 consecutive frames at a rate of 10 frames per second (100 ms exposure time, 100 s time-traces) and extracting the number of counts per particle at each frame. The images were analysed using Andor Solis (ver. 4.14.30001.0, Andor Technology, Northern Ireland) and NIS Elements Ar 4.10.00 (Nikon, Japan) software. The fluorescence intensity time-traces were analyzed by subtracting the background and integrating all the remaining photon counts using a customized analysis software written in LabView (National Instruments).

2.2.7 Cell Culture

Human colon adenocarcinoma SW480 cells, human colon adenocarcinoma DLD-1 cells, normal human colon mucosal epithelial NCM460 cells, normal-human primary dermal fibroblast (NHDF) cells, and human embryonic kidney 293T (HEK 293T), and human bone marrow derived stem cells (BMSCs) (ATTC, USA) cells were cultured in Dulvecco's modified Eagle's medium (DMEM) supplemented with 10%

fetal bovine serum (FBS) and 1% penicillin/streptomycin solution. Cell culture was maintenance at 37 ℃ under humidified air containing 5% CO_2.

2.2.8 Cell Labelling by AIE-Tat Dots

HEK 293T cells were cultured in chamber (LAB-TEK, Chambered Coverglass System) at 37 ℃. After 80% confluence, the medium was removed; the adherent cells were washed twice with 1× PBS buffer. AIE-Tat dots with different concentrations (1 pM, 5 pM, 10 pM, 200 pM, 1 nM, and 2 nM) suspended in cell culture medium were then added into the chamber. After 2 h incubation, the cells were washed twice with 1× PBS buffer. To label lysosome, the cells were further incubated with LysoTracker Red DND-99 (Life Technology, 75 nM) for 30 min. After washing twice with 1× PBS buffer, the cells were immediately imaged by confocal laser scanning microscope (CLSM). For comparison with GFP transfection method, SW480, DLD-1, NCM460, NHDF cells, and HEK293T cells were cultured in 6-well plate. After 80% confluence, the adherent cells were washed twice with 1× PBS, AIE-Tat dots (2 nM) suspended in cell culture media were then added into each well. After overnight incubation, the cells were washed twice with 1× PBS buffer, trypsinalized and then analyzed by flow cytometry measurements using Cyan-LX (DakoCytomation) and the histogram of each sample was obtained by counting 10,000 events. For confocal image studies, the cells were cultured in a 6-well plate containing cell culture coverslip. After being labeled by 2 nM AIE-Tat dots, the cells were washed twice with 1× PBS buffer and then fixed by 4% formaldehyde for 20 minutes. The coverslips were sealed with mounting medium and the fluorescence images were studied by CLSM. To study cell retention of AIE-Tat dots, two groups of HEK293T cells were used. The sample group was incubated with 2 nM AIE-Tat dots overnight at 37 ^{o}C while the control group remains untreated. After incubation and detachment, 2 mL of AIE-Tat-stained cells and 2 mL of control cells

with the same density (40000 cells/mL) were mixed and subcultured in culture flasks for 2 days. Meanwhile, the control and sample cells were also subcultured for 2 day. The three batches of cells were then trypsinalized and tested using flow cytometry. In all flow cytometry tests, blank cells without any treatment were used as the control.

2.2.9 Cytotoxicity of AIE-Tat Dots

Methylthiazolyldiphenyltetrazolium bromide (MTT) assay was used to evaluate the metabolic activity of HEK 293T cells. HEK 293T cells were seeded in 96-well plates (Costar, IL, USA) at a density of 4×10^4 cells/mL, respectively. After 24 h incubation, the old medium was replaced by AIE-Tat dots suspension at concentrations of 2, 5, and 10 nM, and the cells were then incubated for 24 h and 48 h, respectively. The wells were then washed with 1 × PBS buffer and 100 μL of freshly prepared MTT (0.5 mg/mL) solution in culture medium was added into each well. The MTT medium solution was carefully removed after 3 h incubation. Filtered DMSO (100 μL) was then added into each well and the plate was gently shaken for 10 min at room temperature to dissolve all the precipitates formed. The absorbance of MTT at 570 nm was monitored by a microplate reader (Genios Tecan). Cell viability was expressed by the ratio of the absorbance of the cells incubated with AIE-Tat dots to that of the cells incubated with culture medium only.

2.2.10 Cell Labelling by GFP

HEK 293T, SW480, DLD-1, NCM460, and NHDF and BMSCs were grown to 80% confluence in a 6-well plate format prior to transfection. Standard calcium phosphate transfection method was employed to transfect the cells with the pMAX-GFP plasmid (5 μg/ well, Amaxa Biosystems, USA), that drives the expression of the GFP from copepod Pontellina p. Briefly, HEPES buffer solution was added to the

plasmid DNA in $CaCl_2$ solution (250 mM) while vortexing and the mixture was allowed to stand at room temperature for 5 min. Transfection mixture was then added dropwise to the chamber and incubated overnight before the cells were washed three time with 1× PBS buffer and trypsinalized. The fluorescence intensities of cells were then analyzed by flow cytometry measurements using Cyan-LX (DakoCytomation). The histogram of each sample was obtained by counting 10,000 events. For confocal image studies, the cells were cultured in 6-well plate containing cell culture coverslip. After being labeled by pMAX-GFP, the cells were washed twice with 1× PBS buffer and then fixed by 4% formaldehyde for 20 minutes. The coverslips were sealed with mounting medium and the fluorescence images were studied by CLSM.

2.2.11 *In Vitro* Cell Tracing

The HEK 293T cells were cultured in 6-well plates. After reaching 80% confluence, the cells were labeled by AIE-Tat dots or transfected by pMAX-GFP plasmid. After labeling, the cells were diluted in to 6-well plates for designated times (1 to 12 days with an interval of 1 day). After designated time intervals, the cells were washed twice with 1× PBS buffer and then trypsinalized to suspend in 1× PBS buffer. The fluorescence intensities of cells were then analyzed by flow cytometry. For confocal image studies, the labeled cells were diluted in 6-well plates containing cell culture coverslips for designated time intervals. Upon reaching the time interval, the cells were washed twice with 1× PBS buffer and then fixed by 4% formaldehyde for 20 minutes. The coverslips were sealed with mounting medium and the fluorescence images were studied by CLSM. The laser at 514 nm was adopted to obtain the one-photon excited fluorescence images with a 550–780 nm bandpass filter.

2.3 Results and Discussion

2.3.1 Fabrication of AIE-Tat Dots

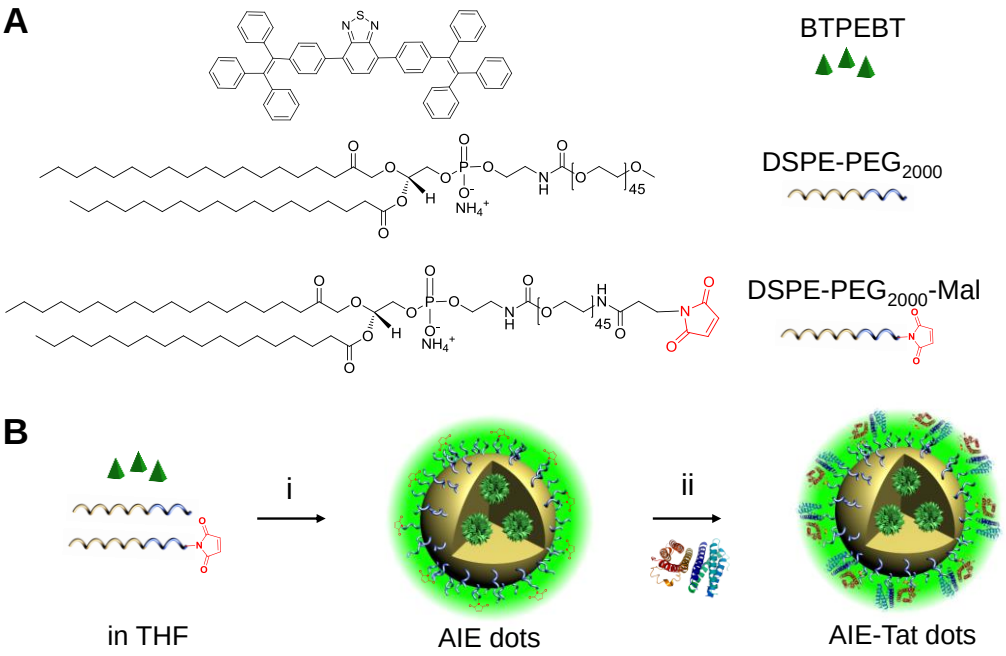

Scheme 2.1. A) Chemical structures of BTPEBT, DSPE-PEG$_{2000}$, and DSPE-PEG$_{2000}$-Mal. B) Schematic illustration of AIE-Tat dots formation.

To demonstrate the fabrication of AIE dots, BPTEBT (Scheme 2.1A) was selected and synthesized *via* Suzuki coupling reaction according to previous report.[82, 116] The AIE effect of BTPEBT was studied by measuring its photoluminescence (PL) spectra in tetrahydrofuran (THF)/water mixture with different water fraction (f_w). Along with increasing f_w, BTPEBT initially showed gradually quenched fluorescence, followed by fluorescence recovery (Figure 2.1). The fluorescence quenching represents twisted intramolecular charge transfer (TICT) caused by solvent polarity increase due to the donor and accepter structure of BTPEBT.[117] Upon further increasing f_w to 50% or high, BTPEBT started to form nano-aggregates, which is companied with the fluorescence recovery, indicating that AIE plays the dominant role for the bright fluorescence in aggregate state. Such a special molecular structure makes BTPEBT a perfect candidate for construction of ultra-bright NPs for biological applications.

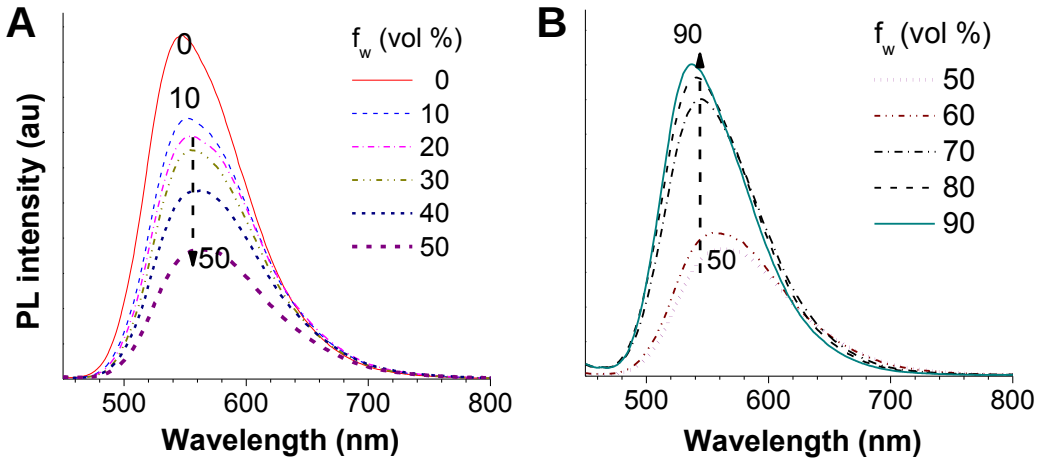

Figure 2.1. PL spectra of BTPEBT in THF/water mixtures with various water fractions, (A) f_w = 0 to 50 vol%, (B) f_w = 50 to 90 vol%. [BTPEBT] = 10 μM, λ_{ex} = 422 nm.

A modified nano-precipitation method is applied to fabricate the ultra-bright and biocompatible BTPEBT-loaded AIE dots. 1,2-Distearoyl-sn-glycero-3-phosphoethanolamine-N-[methoxyl-(polyethylene glycol)-2000] (DSPE-PEG_{2000}) and its maleimide ended derivative, namely DSPE-PEG_{2000}-Mal (Scheme 2.1A), were used as the encapsulation matrices to embed BTPEBT into the core of resultant AIE dots. Scheme 2.1B shows the schematic illustration of BTPEBT-loaded AIE dots formation, which is achieved by dropwise addition of the THF mixture of matrix polymer and BTPEBT into MilliQ water under ultrasound sonication. During the mixing and sonication, the hydrophobic DSPE segments will intertwine with BTPEBT molecules to form the core, and hydrophilic PEG chains extend towards aqueous phase to prevent AIE dots from further aggregation. The ultrasound energy will prevent the formation of large aggregates. The presence of PEG shells further stabilized the AIE dots by forming the protective shells. The PEG shells also minimize their nonspecific interaction with biological species and help provide functional groups for further chemical or biological conjugation. After THF evaporation, a cysteine modified cell membrane penetration peptide (RKKRRQRRRC) derived from HIV-1 transactivator

(Tat) of transcription protein[118, 119] was conjugated onto AIE dots through click reaction between surface maleimide and the thiol groups of the peptide to yield AIE-Tat dots.

2.3.2 Characterization of AIE-Tat Dots

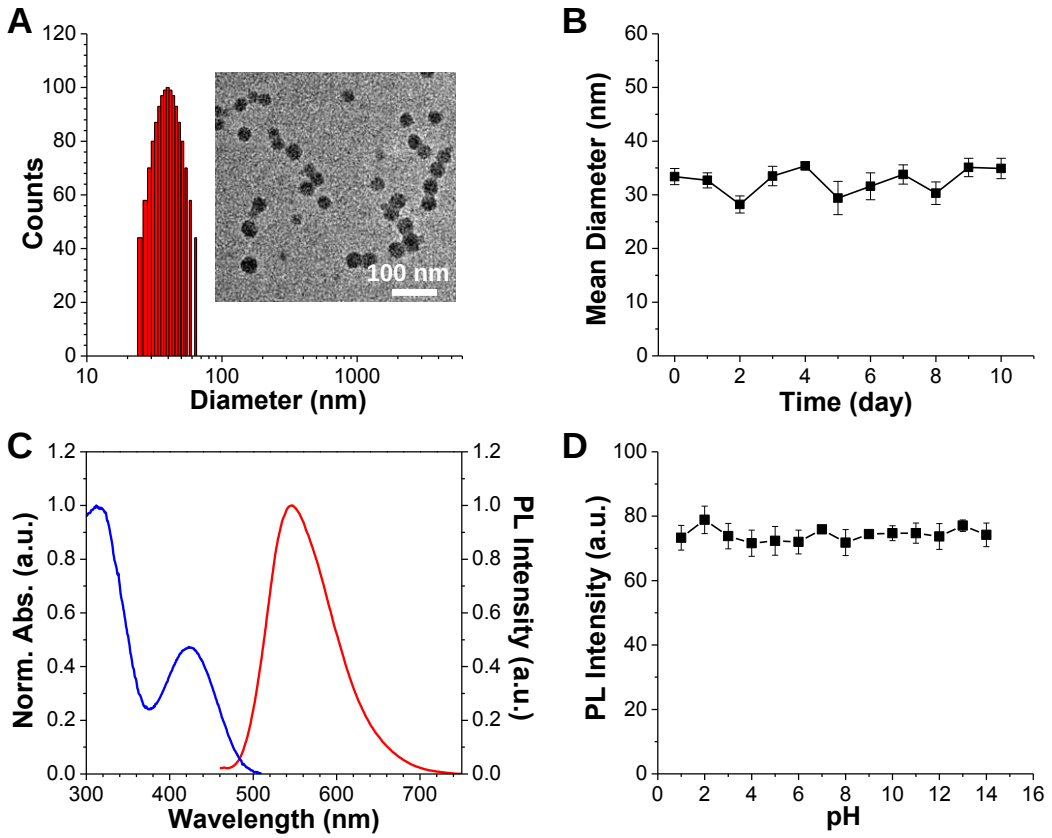

Figure 2.2. (A) LLS result of AIE-Tat dots in aqueous solution, inset is TEM image of AIE-Tat dots. (B) Hydrodynamic diameter changes of AIE-Tat dots upon continuous incubation in 1×PBS at 37 ºC for 10 days. (C) Absorption and PL spectra of AIE-Tat dots in water at room temperature. (D) PL intensity changes of AIE-Tat dots at 547 nm in water at different pH. λ_{ex} = 420 nm.

Laser light scattering (LLS) was applied to study the size distribution of AIE-Tat dots, which revealed an average hydrodynamic diameters 33.9 ± 1.4 nm, with narrow size distribution and a polydispersity of ~0.10 (Figure 2.2A). The AIE-Tat dots are spherical with a diameter of ~30 nm under transmission electron microscopy (TEM) (Figure 2.2A, inset). It should be noted that the AIE dots are compact packed rather than forming micelles, as evidenced by the black dots in TEM due to high electron density of AIEgen, and the stable hydrodynamic sizes during the dilution of AIE dots

with water. The colloidal stability of AIE-Tat dots in biological environment was also studied by incubating the AIE-Tat dots in 1× phosphate buffered saline (PBS) at 37 ℃ for ten days. LLS results showed similar hydrodynamic diameters within the tested period (Figure 2.2B). Moreover, the AIE-Tat dots suspension remained clear and no precipitation was observed after storage for 3 month, indicating high colloidal stability.

Figure 2.2C shows the UV-vis and PL spectra of AIE-Tat dots in aqueous suspension. The AIE-Tat dots have two absorption peaks centred at 318 and 422 nm, with a molar extinction coefficient of 5.9×10^7 $M^{-1}cm^{-1}$ at 422 nm on the basis of dot concentration. The AIE-Tat dots show an emission maximum at 547 nm, with a large Stokes shift of 125 nm and a high fluorescence quantum yield of 63 ± 2%, measured using Rhodamine 6G in methanol as the standard (quantum yield = 93%). The high quantum yield arises from the AIE feature of BTPEBT, where BTPEBT fluorogens form strong emissive aggregates in the NPs. Such a large Stokes shift should minimize the signal interference from excitation laser source. It should be the AIE-Tat dots exhibited high resistance to surrounding environment pH changes, where the brightness is not affected upon varying the suspension pH value from 1 to 14, as shown in Figure 2.2D.

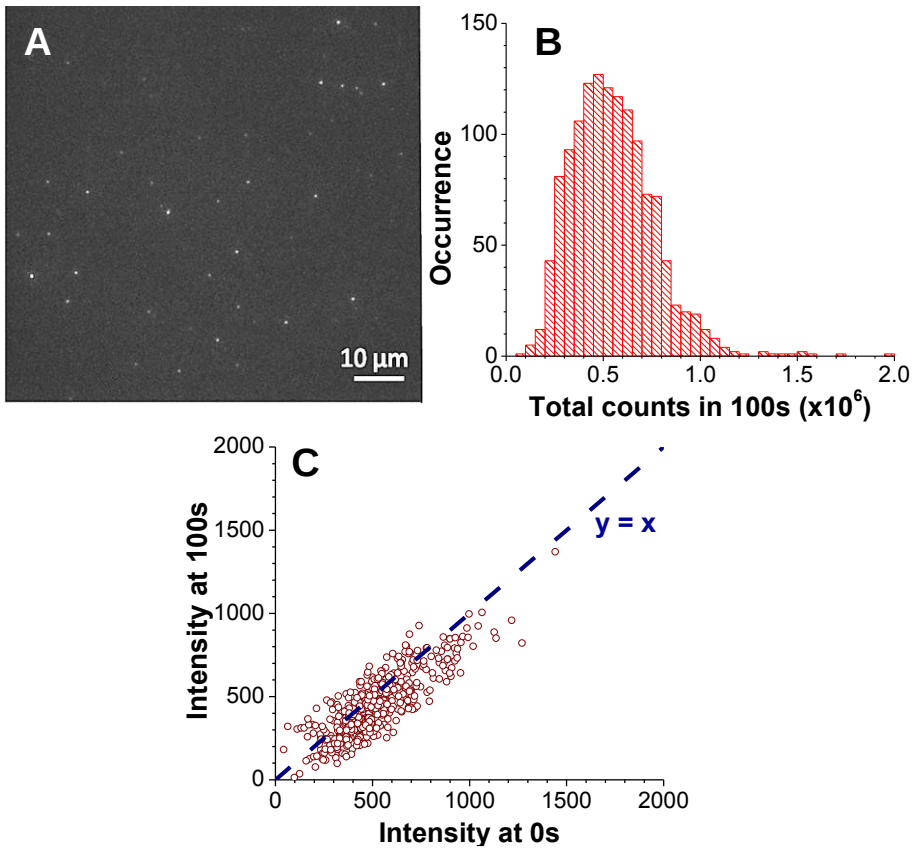

Figure 2.3. (A) Representative wide field fluorescence image of individual AIE-Tat dots. (B) Corresponding fluorescence intensity histogram of AIE-Tat dots (1338 dots) emitted during 100s. (C) Fluorescence changes of individual AIE-Tat dots after 100s laser scanning.

Wide-field fluorescence microscopy was further applied to evaluate the photophysical properties of individual AIE-Tat dots. Figure 2.3A represents a luminescence image of individual AIE-Tat dots under 488 nm laser excitation, and Figure 2.3B summarizes the corresponding histograms of total number of photons emitted by these 1388 representative AIE-Tat dots within 100s. The AIE-Tat dots show an average emitted photon number of 6.07×10^5 counts under excitation of 488 nm laser, indicating the high brightness of AIE-Tat dots, which is much higher than QD Tracker 585. Photo-bleaching of the representative dots is shown in Figure 2.3C, by plotting the final intensity of each dot after 100s exposure versus its initial intensity. The extent of difference would give the magnitude of photobleaching. A line with a slope of 1 is drawn as reference, representing no change in the intensity within 100s.

The dots lying close to or above the reference line are considered as non-bleaching due to the inevitable intensity signal fluctuation. Even though some dots become slightly faded, the majority lies around the diagonal line, indicating high photostability of the AIE-Tat dots.

In addition, the fluorescence intensity changes of individual AIE dots under continuous excitation for 100 s were also studied. Figure 2.4 shows representative fluorescence intensity time-traces of two individual AIE-Tat dots and two QD tracker 585. It is observed that AIE dots have stable fluorescence within the test period, without intermittency, known as characteristic blinking for QDs. This offers great advantages and opportunities for AIE-Tat dots in real-time single dot tracing studies.

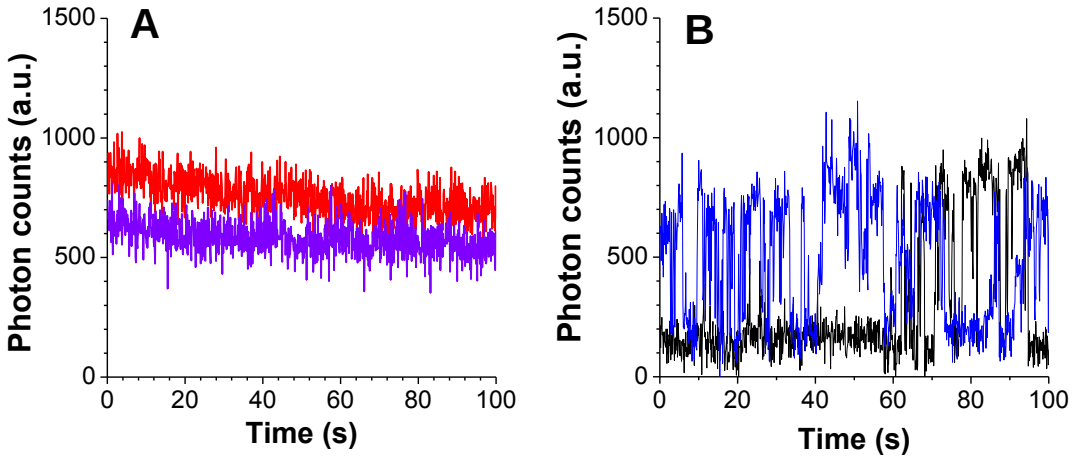

Figure 2.4. Representative fluorescence time traces of A) two AIE-Tat dots and B) two QD Tracker 585 within 100s.

2.3.3 *In Vitro* Cellular Imaging by AIE-Tat Dots

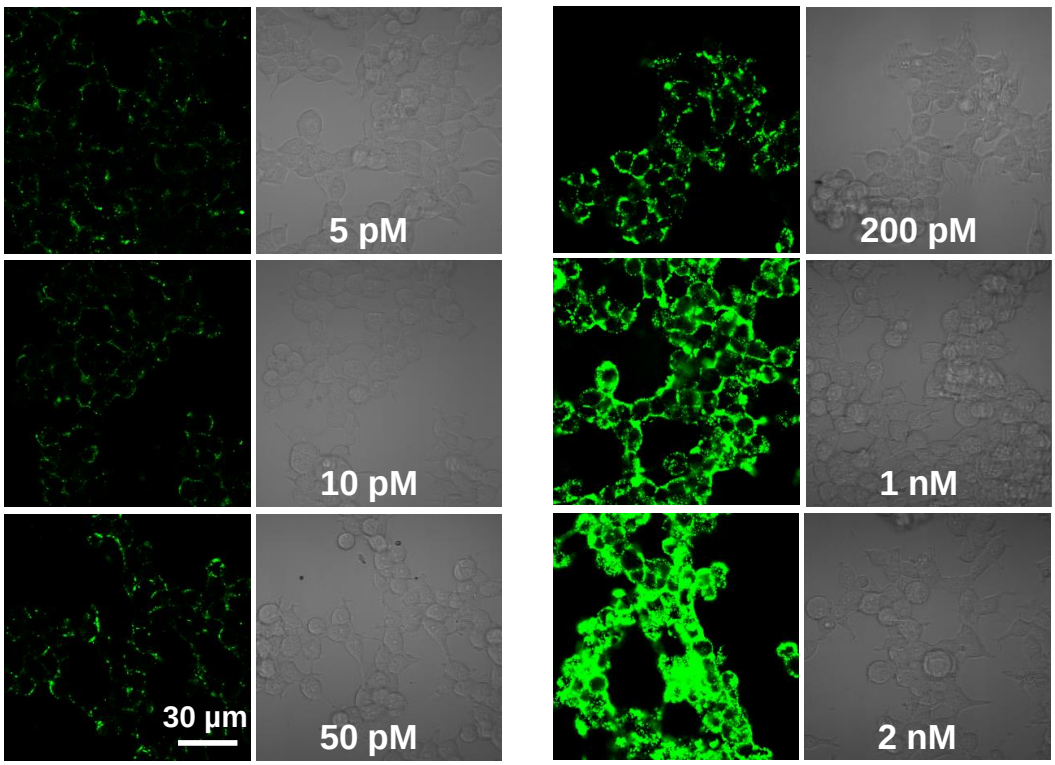

Figure 2.5. CLSM images of HEK 293T cells after incubation with AIE-Tat dots at different concentrations for 2 h. All the images share the same scale bar of 30 μm.

The *in vitro* cellular imaging performance of AIE-Tat dots was evaluated using human embryonic kidney 293T (HEK 293T) cells as a model. AIE-Tat dots are passively loaded into adherent HEK 293T cells by incubating them with AIE-Tat dots at different concentrations (0 to 2 nM). After 2 h incubation, the fluorescence images of HEK 293T cells were examined using CLSM with emission signal collected above 505 nm upon excitation at 488 nm. A progressive increase in green fluorescent signal from the cellular membrane to cytoplasm was observed along with increase in AIE-Tat dots concentrations (Figure 2.5). At low AIE-Tat dot concentration of 50 pM or lower, the AIE-Tat dots tend to bind to cell membrane, whereas negligble fluorescence was detected from the cytoplasm. However, at an incubation concentraion of 2 nM, the accumulation of green fluorescence in the cytoplasm is clearly observed. These results coincide well with literature, where Tat peptide mediated cell uptake mechanism occurs

in two stages: binding to membrane surface before a threshold surface coverage is reached, followed by disintegration of membrane and internalization into the cytoplasm.[118] While without Tat functionalization, the AIE dots can hardly internalize into cells, where only very weak fluorescence can be observed inside HEK 293T cells (Figure 2.6). This is due to the suppressed nonspecific internalization by the presence of PEG protective shells, which also indicates that this formulation can be further functionalized with specific targeting ligands for targeted cellular imaging with high selectivity and sensitivity.

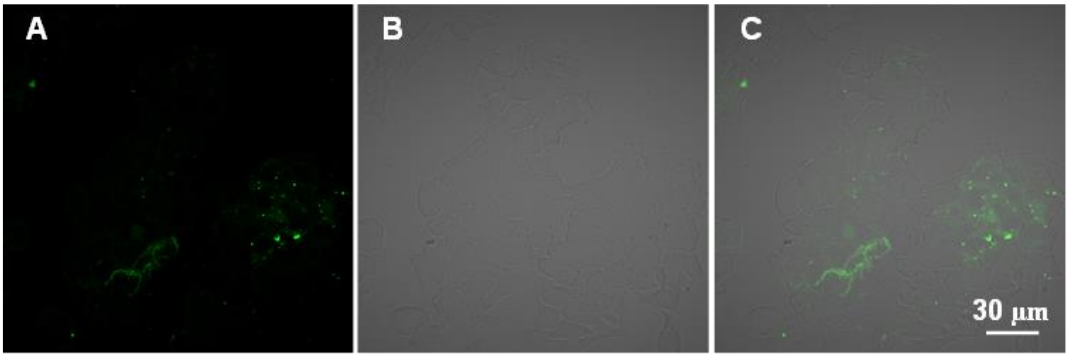

Figure 2.6. A) Fluorescence, B) white field, and C) fluorescence/white field overlay images of HEK 293T cell after 2 h incubation with AIE dots (2 nM).

The HEK 293T cells were further co-stained with LysoTracker Red DND-99 which selectively stains the lysosomes to determine the subcellular distribution of AIE-Tat dots. The results are shown in Figure 2.7A, besides labelling the lysosome vesicles, the AIE-Tat dots are also able to stain almost everywhere else in the cytoplasm, providing insights into the sub-cellular distribution of the AIE-Tat dots. In addition, 3D fluorescence image of HEK 293T cell revealed a homogeneous distribution of AIE-Tat dots inside the cells (Figure 2.7B). This indicates the excellent colloidal stability of AIE-Tat dots in the cytoplasm, which promotes the equal distribution of AIE-Tat dots in daughter cells during cell division. Moreover, we also mixed equal number of unstained HEK 293T cells with AIE-Tat dots labelled cells. After 2 days co-culture, the

mixed cells showed similar flow cytometric spectrum to that of AIE-Tat dots labelled cells (Figure 2.7C), indicating the high cell retention of AIE-Tat dots during cell proliferation. The equal distribution of positively stained and negative stained cells also hints that cell cycle is not affected by AIE-Tat dots. These properties are highly promising for long term tracking of cell migration, among other tracing related applications.

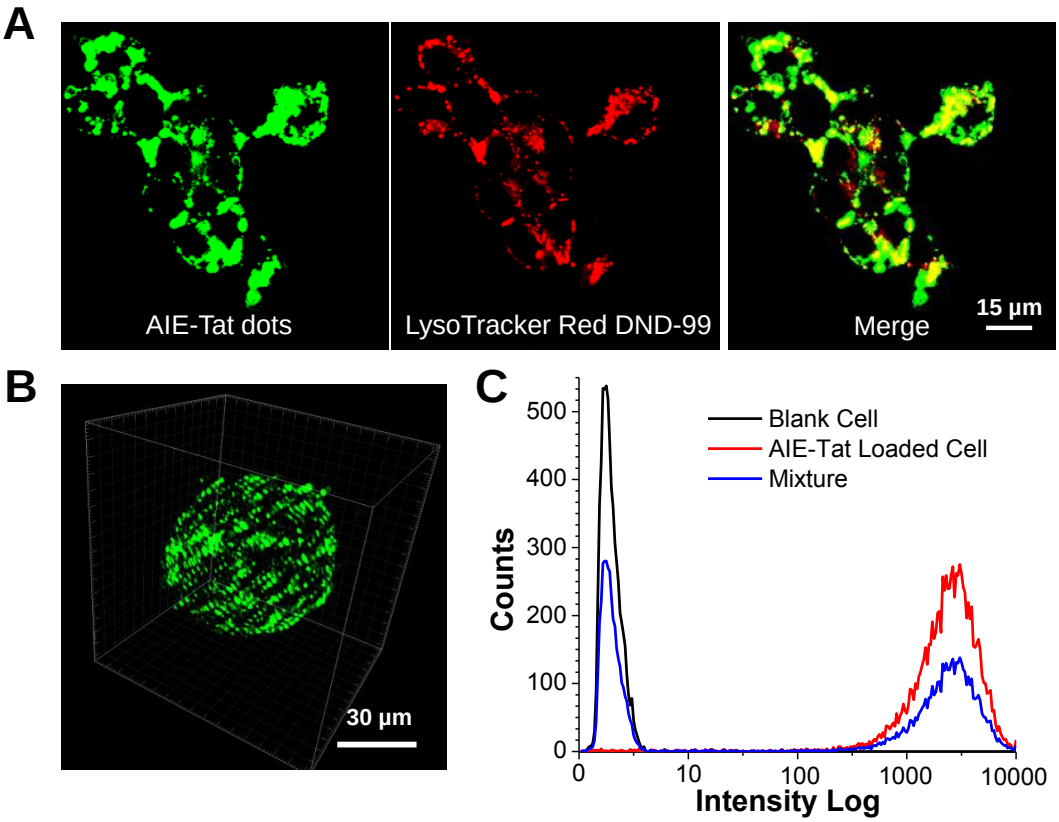

Figure 2.7. (A) CLSM images of HEK 293T cells after incubation with AIE-Tat dots (2 nM, 2 h) and Lysotracker Red DND-99 (75 nM, 30 min) in sequence. (B) 3D CLSM image of AIE-Tat dots treated HEK 293T cells. (C) Flow cytometry histograms of HEK293T cells stained by 2 nM AIE-Tat dots at 37 ºC for 24 h (red line), unstained cells (black line) and a mixture of AIE-Tat dot-stained HEK293T cells and unstained cells (1:1; blue line) after 2 days co-culture. The histograms were recorded after co-culturing for 2 days after mixing.

2.3.4 *In Vitro* Cell Labelling Comparison between GFP and AIE-Tat Dots

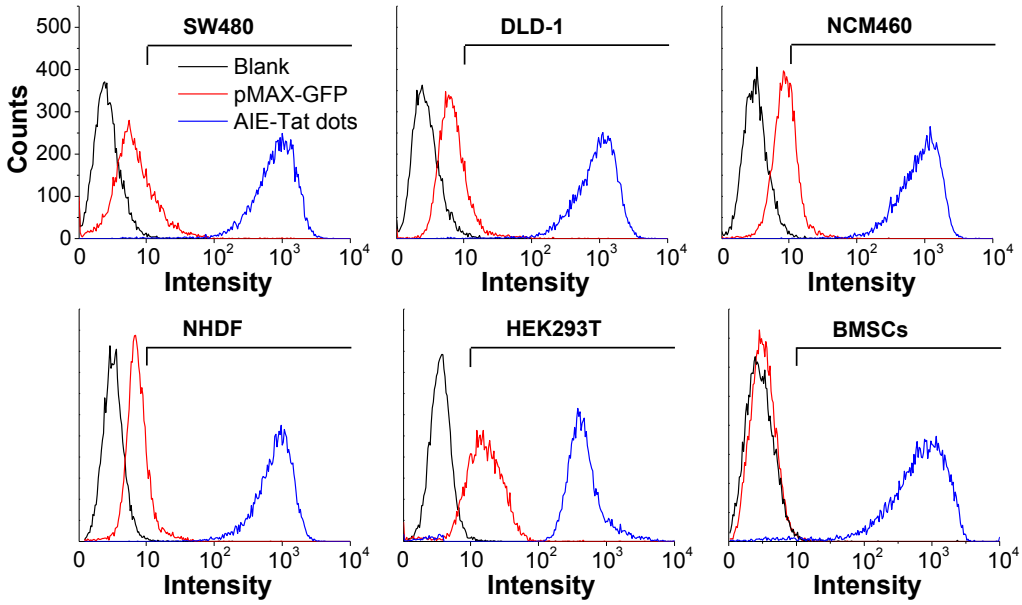

Figure 2.8. (A) Flow cytometry histograms of different cell lines after pMAX-GFP expression (red lines), AIE-Tat dots staining (blue lines) or without any treatment (black lines).

Next, the application of AIE-Tat dots as a generic labelling agent was further examined using a panel of human cells of different tissue origin. HEK 293T cells, human colon adenocarcinoma SW480 cells (SW480), human colon adenocarcinoma DLD-1 cells (DLD-1), normal human colon mucosal epithelial cells (NCM460 cells), normal human primary dermal fibroblast cells (NHDF cells), and human bone marrow derived stem cells (BMSCs) were chosen as *in vitro* model cell lines. Calcium phosphate transfection method was employed as a standard benchmark to transfect these cells to express GFP.[120] pMAX-GFP plasmid (5 μg/ well) that drives the GFP expression from copepod Pontellina p. was incubated with the cells overnight. Similar procedures were also repeated for cells to be labeled by AIE-Tat dots (2 nM). The labeling efficiencies by GFP or AIE-Tat dots are assessed by means of flow cytometry analysis. Figure 2.8 shows the fluorescence profiles of these cell lines. Among the cells tested, only HEK 293T cells display relative high GFP expression, while SW480, DLD-1, NCM460, NHDF and BMSCs through are GFP-positive but with extremely low

mean fluorescence, which falls just above the cell auto-fluorescence profile. These results are similar to literature reports, where non-viral transfection methods present relatively low and cell type dependent transfection[24, 25]. On the contrary, AIE-Tat dots showed nearly 100% labeling efficiencies towards all the tested cell lines, with over 100-fold higher mean fluorescence intensity as compared to GFP labeled cells.

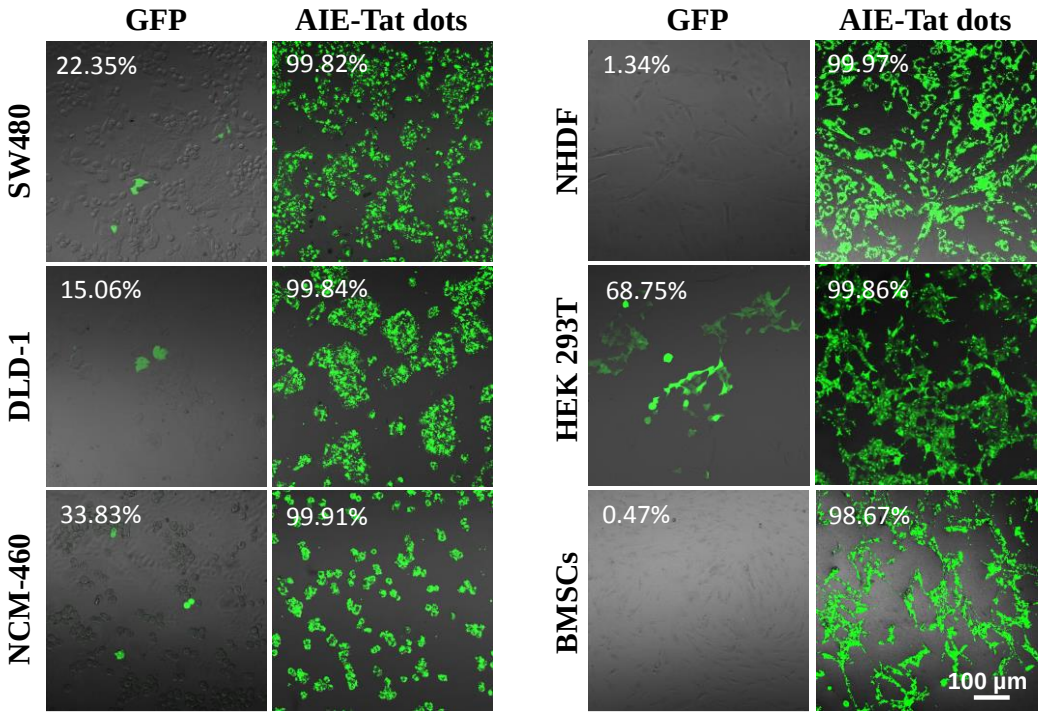

Figure 2.9. Fluorescence/transmission overlay images of pMAX-GFP expressed cells and AIE-Tat dots labelled cells. Insets are labelling rates measured by flow cytometry. All the images share the same scale bar.

This results were further confirmed by CLSM images (Figure 2.9), where only few cells were lighted up by GFP for most of these cell lines, indicating the the limitation of GFP transfection method in practical applications. Among them, HEK 293T showed the highest GFP labelling rate of 70%, which is still not satisfied for long term cell tracing. On the other hand, all the cells treated with AIE-Tat dots showed bright green fluorescence, despite of cell types, indicating that Tat functionalized AIE dots are able to internalized into most type of cells, even primary cells, and stem cells . In addition, it is noteworthy that the cells directly labeled by AIE-Tat dots can be

immediately detected by CLSM and flow cytometry, while a lag period of several to 24 hours between plasmid introduction and GFP expression exists for GFP transfection, further revealing the advantage of AIE dots as imaging contrast over GFP.

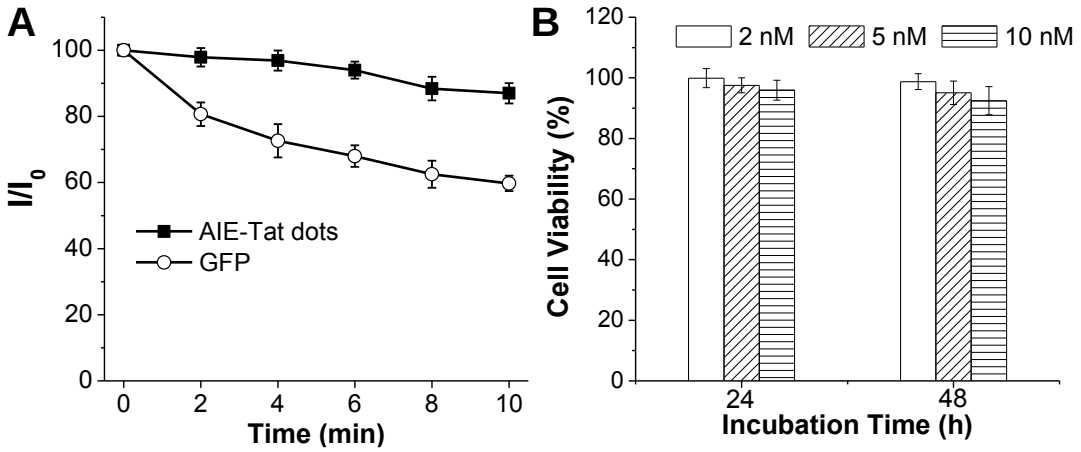

Figure 2.10. A) Photostability of AIE-Tat dots and GFP in HEK293T cells. B) Cell viability of HEK293T cells after incubation with AIE-Tat dots at different concentrations for 24 and 48 h, respectively.

In addition, AIE-Tat dots showed higher photostability inside the cells, where the signal loss of AIE-Tat dots-staining cells is less than 15%, while GFP transfected cells lost 40% of their fluorescence after 10 min of continuous laser scanning (Figure 2.10A). As biocompatibility of fluorescent materials is of high importance, the metabolic viability of HEK293T cells after treatment with AIE-Tat dots was examined by methylthiazolyldiphenyltetrazolium bromide (MTT) assays. The HEK 293T cells show over 95% cell viability even after 48 h incubation with 10 nM AIE-Tat dots (5-fold higher concentration than that used for imaging), indicating their excellent biocompatibility and very low cytotoxicity (Figure 2.10B). Collectively, these results suggest that our AIE-Tat dots outperform the traditional fluorescent protein-based live cell labelling on several fronts, thus making them a promising choice for cell imaging and tracing.

2.3.5 *In Vitro* Long Term Cell Tracing

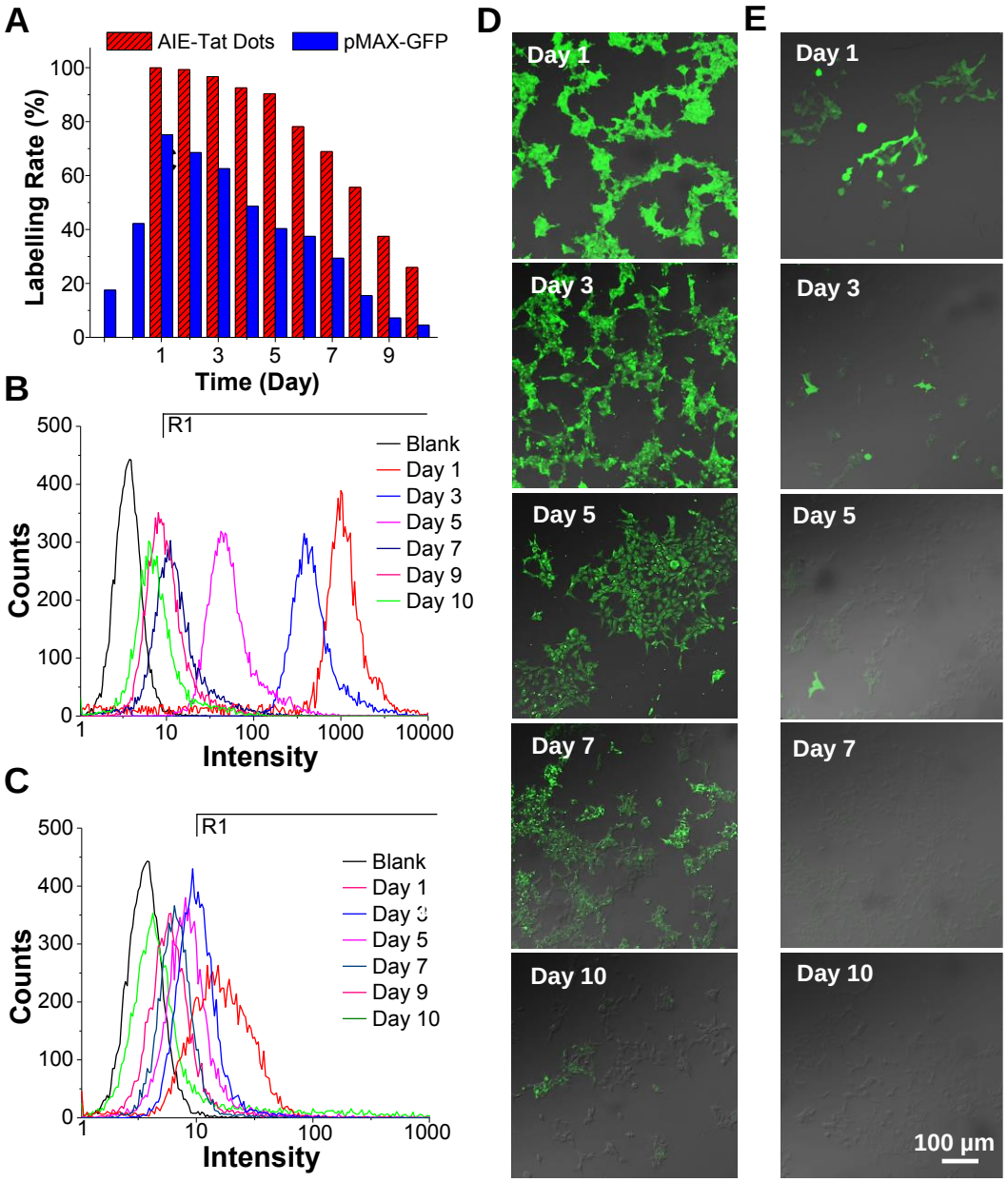

Figure 2.11. (A) Continuous monitoring of cell labelling rates by GFP or AIE-Tat dots for 10 days. (B) and (C) Flow cytometry histograms of HEK 293T cells after incubation with (B) 2 nM AIE-Tat dots or (C) 5 μg/well p-MAX-GFP plasmid overnight and then sub-cultured for designated times. (D) and (E) CLSM images of HEK293T cells labelled by (D) AIE-Tat dots or (E) pMAX-GFP at different days post-incubation. All the images share the same scale bar.

The ability to achieve long term live cell tracking is indispensable for studies of cell migration, chemotaxis, proliferation and differentiation, among other fundamental biological processes. Due to the display of high GFP transfection efficiency, HEK 293T cells were chosen as the model cell line to compare the *in vitro* cell tracing ability

between AIE-Tat dots and pMAX-GFP. After overnight incubation with AIE-Tat dots or GFP plasmid, these cells were subcultured for designated time intervals. The fluorescence profiles and labeling rates by the two methods were accessed by flow cytometry, and the results are shown in Figure 2.11. AIE-Tat dots labeled HEK293T cells show 99.98% labeling efficiency at 1st day after incubation, which remains above 90% on the 5th day of post-incubation (Figure 2.11B). After 10 days of continuous cell culture, the cell labeling rate drops to 20%, while clearly distinguishable fluorescence profile from untreated cells was still observed. On the other hand, due to the existence of signal lag period (Figure 2.11A), the brightest GFP signal was observed on the 3rd day after plasmid introduction, which was defined as the 1st day for cell tracing. The highest GFP labeling rate is 68% on the 1st day, with only 3-fold higher mean fluorescence intensity than blank HEK 293T cells (Figure 2.11C). On the 5th and 10th days of post-incubation, the GFP-positive cells are only around 30% and 4%, respectively. The confocal images were also provided to further confirm their cell tracing performance. Over half cells showed bright GFP fluorescence on the first two days, but only a few cells show GFP fluorescence on the 3rd and 5th day (Figure 2.11E). From 7th day onwards, no GFP-positive cell can be observed. AIE-Tat dots labeled cells still show bright fluorescence for almost all the cells at 7th day of post-incubation, and the signal is traceable in some cells on the 10th day (Figure 2.11D). The high brightness and long cell tracing period indicate that AIE-Tat dots can be efficiently internalized into cell cytoplasm with high cytoplasm retention ability and is able to pass to daughter cells during cell proliferation.

2.4 Conclusion

In summary, we successfully fabricated BTPEBT-loaded organic AIE dots conjugated with surface cell penetration peptides (HIV-1 Tat) (AIE-Tat), and

demonstrated their applications of non-invasive *in vitro* cell imaging and tracing. Benefitting from the AIE nature of BTPEBT, the AIE-Tat dots showed ultra-bright and stable fluorescence under different pH conditions and upon continuous laser scanning. *In vitro* cellular imaging study reveals an extremely low working condition of 200 pM for cell labelling purpose, and an excellent colloidal stability and even distribution of AIE-Tat dots in cell cytoplasm with excellent cell retention. In addition, AIE-Tat dots showed successful internalization into all tested six different human cell lines including stem cells all with ~100% labelling efficiencies, superior over the commonly used calcium phosphate mediated GFP transfection method where only HEK 293T cells showed a high GFP labelling rate of ~70%. The cell tracing experiments further revealed that the internalized AIE-Tat dots could be efficiently transferred to daughter cells during cell proliferation and trace HEK 293T cells up to 10 days (equivalent of 14 generations) with almost 100% cell labelling rate within the first 5 days, outperforming GFP plasmid transfection method. This study clearly demonstrated the promising performance of AIE-Tat dots as directed labelling agents for long term cell tracing, which should open new opportunities for oncology studies and cell based therapy. Moreover, AIE dots are capable of conjugation with different targeting moieties and other imaging modalities such as magnetic resonance and nuclear imaging agents, which further renders AIE dots broader biological applications.

CHAPTER 3

MULITMODAL DETECTION OF VASCULAR INTEGRITY AND LEAKAGE BY GADOLINIUM FUNCTIONALIZED ORGANIC DOTS WITH AGGREGATION-INDUCED EMISSION CHARACTERISTICS

3.1 Introduction

Inflammatory reactions are common pathophysiological processes involved in innumerable diseases, atherosclerotic plaque development as well asbiological implants.[73, 121-123] For example, dengue inflammation is the most important mosquito-borne disease which could lead to fatal dengue shock syndrome, brain inflammation could lead to early brain injury and even life-threaten aneurysmal subarachnoid hemorrhage (SAH),[123] while lung inflammation could result in chronic obstructive pulmonary disease and asthma.[124] A method or agents that could accurately and reliably visualize and determine the acute, localization and severity of infection and inflammation is of great clinical importance for rapid initiation appropriate treatment, delineation. Several imaging techniques such as magnetic resonance imaging (MRI),[125] positron emission tomography[126, 127] or ultrasonography[128] have been developed for inflammation detection and quantification.[129] However, these techniques rely on morphologic or metabolic changes and cannot be able to accurately identify acute and localized inflammation in the early stage.[130]

The blood vessels serve as a physical barrier and function in a highly responsive and dynamic manner, allowing rapid control of the transport rate of solutes, macromolecules and leukocytes between blood and tissue.[130, 131] The regulation of vascular permeability is a highly coordinated process that is fundamental for the maintenance of homeostasis in the body. While this regulation is important for the initiation and resolution of immune responses as well as for tissue repair, the loss of barrier function and increase of vascular leakage are often associated with the pathogenesis of inflammatory diseases. Although early recognition of vascular leakage has been adopted by the WHO as a guideline to identify patients that are at risk of developing severe dengue, there are no effective diagnostic and predictive measures for

this purpose. Thus, there is an urgent need for a standardized approach to examine vascular leakage for risk prediction in dengue infections and other inflammations. It also has been reported that Evans blue could bind to albumin in the blood, which can served as a marker for detection of vascular permeability by measuring its absorbance at 620 nm.[132-134] The discovery of red fluorescence of Evans blue under excitation and the development of two-photon fluorescence imaging (TPFI) technique further make it possible for visualizing the *in vivo* leakage process.[135, 136] TPFI utilizes the low-energy irradiation in the near-infrared (NIR) region (700-1000 nm) as the excitation source, which has high tissue penetration depth and low auto fluorescence interference.[82] However, the inevitable leakage of Evan blue in normal blood vascular makes it difficult to quantitatively determine the leakage severity, and fluorescence of such small molecules are largely affected by surrounding environment, further lowering its detection sensitivity.

The discovery of fluorogens with aggregation-induced emission characteristics (AIEgens) provided the exciting opportunities for fabrication of organic dots (AIE dots) with ultrahigh brightness for biological applications.[39, 42, 53] In previous chapter, we have successfully demonstrated the (1,2-distearoyl-sn-glycero-3-phosphoethanolamine-N- [methyl(polyethylene glycol)-2000]) (DSPE-PEG_{2000}) encapsulated AIE dots showed ultrahigh brightness and excellent stability. In addition, the existence of PEG protective shells prevent the nonspecific interaction with surrounding biomolecules or proteins, which further inspired us to fabricate AIE dots for *in vivo* biological applications. Herein, in this chapter, we reported a multimodality fluorescent toolbox for the assessment of vascular leakage in a preclinical mouse model of inflammation. DSPE-PEG with amine terminal groups was used to encapsulate a new AIEgen with strong red emission in aggregated state, 2,3-bis(4-(phenyl(4-(1,2,2-

triphenylvinyl)phenyl)amino)phenyl)furmaronitrile (TPETPAFN), to form the AIE dots. AIE dots were further surface functionalized with gadolinium (Gd), the resultant AIE-Gd dots showed ultra-bright and stable fluorescence in aqueous buffer solution. These AIE-Gd dots also showed excellent colloidal stability, photostability and high two-photon absorption. The Gd content can be precisely quantified by ICP-MS at ppb level, which should provide the severity of leakage with high sensitivity. We demonstrated that these hybrid dots are able to leak outside from blood vessel upon inflammation. Using these novel tools based on organic-inorganic hybrid AIE dots, we aim to better understand inflammation induced vascular leakage, and to explore the possibility to translate these probes into clinical applications for early diagnosis of vascular leakage.

3.2 Experimental

3.2.1 Materials

1,2-Distearoyl-sn-glycero-3-phosphoethanolamine-N-[amino(polyethylene glycol)-2000] (DSPE-PEG_{2000}-NH_2) was a commercial product of Avanti Polar Lipids, Inc. Gadolinium(III) chloride hexahydrate and *N*,*N*-dimethylformamide (DMF) was purchased from Sigma. 2,2',2''-(10-(2-((2,5-dioxopyrrolidin-1-yl)oxy)-2-oxoethyl)-1,4,7,10-tetraazacyclododecane-1,4,7-triyl)triacetic acid (DOTA-NHS-ester) was purchased from CheMatech. Tetrahydrofuran (THF) was distilled from sodium benzophenone ketyl under dry nitrogen immediately prior to use. All reactions and manipulations were carried out under nitrogen gas with the use of standard inert atmosphere. Milli-Q water was supplied by Milli-Q Plus System (Millipore Corporation, Breford, USA). Ultrapure grade 10×phosphate-buffered saline (PBS) buffer with pH = 7.4 was purchased from 1st BASE Singapore.

3.2.2 Characterization

NMR spectra were measured on a Bruker AV 500 NMR spectrometer (DRX 500, 500 MHz). UV-vis spectra were recorded on a Shimadzu UV-1700 spectrometer. Photoluminescence (PL) spectra were recorded on a Perkin-Elmer LS 55 spectrofluorometer. Average particle size and size distribution of the samples were measured by laser light scattering (LLS) with a particle size analyzer (90 Plus, Brookhaven Instruments Co. USA) at a fixed angle of 90 ° at room temperature. The morphology of the samples was studied by transmission electron microscopy (TEM, JEM-2010F, JEOL, Japan). ICP-MS was used to detect the contents of Gd on dot surface and inside the ear.

3.2.3 Synthesis of AIE-Gd Dots

2,3-bis(4-(phenyl(4-(1,2,2-triphenylvinyl)phenyl)amino)phenyl)furmaronitrile (TPETPAFN) (Figure 1a) was synthesized according to literatures.[22] To fabricate AIE dots with amino group as the surface, a THF solution (1 mL) containing TPETPAFN (1 mg) and DSPE-PEG_{2000}-NH_2 (2 mg) was poured into water (10 mL) under sonication using a microtip probe sonicator at 12 W output (XL2000, Misonix Incorporated, NY). The mixture was further placed in dark in fume hood for THF evaporation at 600 rpm overnight. The AIE dots were further mixed and reacted with excess DOTA-NHS-ester overnight. After reaction, the dot suspension was dialysed against MilliQ water using membrane with cut-off of 6-8 kDa for 2 days to eliminate the unreacted DOTA-NHS-ester. The obtained AIE dot suspension is further chelated with Gadolinium(III) chloride hexahydrate. After overnight reaction, the resultant AIE-Gd dot suspension was dialysed against MilliQ water using membrane with cut-off of 6-8 kDa for 2 days to eliminate the unreacted Gd. AIE-Gd dot suspension was further purified by filtering through a 0.2 μm syringe driven filter and stored at 4 ℃. The obtained AIE dots were

further freeze-dried, and the weight of the final powder is weighted. The powder was dissolved in THF solution, and the absorbance of TPETPAFN is measured. According to the standard calibriation curve of the absorbance and concentration of TPETPAFN, the weight of TPETPAFN in the powder was obtained, and so as the encapsulation efficiency.

3.2.4 Single Particle Fluorescence Imaging

Fluorescence imaging of individual AIE-Gd dot was performed with a custom-built Wide-Field Microscope (WFM) based on a Nikon ECLIPSE Ti-U inverted microscope frame. Light from a CW multi-line Ar ion laser (Melles Griot, CA, USA) was fiber-coupled to a Nikon TIRF attachment and focused on the back aperture of a high NA objective (Nikon TIRF Apo 100×, NA = 1.49, oil immersion). Immersion oil (n_D = 1.4790, Cargille, USA) was added between the high NA objective and the cover slip for index matching. The luminescence was collected by the same objective. After passing through the dichroic mirror and the emission filter, the luminescence was directed onto an iXonEM+897 EMCCD camera (512 × 512 pixels, 150 nm per pixel resolution, Andor Technology, Northern Ireland) connected to the side port of the microscope. A filter set consisting of a z488/10× excitation filter, Z488RDC dichroic mirror, and HQ500LP emission filter was used for imaging. The camera was connected to a computer furbished with camera-dedicated software to control the imaging parameters, and for data acquisition. The samples were prepared by depositing a droplet of NP solutions on a glass cover slide, waiting for 30s for particles adsorption to the substrate, removing excess of liquid and drying under N_2. Fluorescence intensity time-traces were obtained by acquiring 1000 consecutive frames at a rate of 10 frames per second (100 ms exposure time, 100 s time-traces) and extracting the number of counts per particle at each frame. The images were analysed using Andor Solis (ver.

4.14.30001.0, Andor Technology, Northern Ireland) and NIS Elements Ar 4.10.00 (Nikon, Japan) software. The fluorescence intensity time-traces were analyzed by subtracting the background and integrating all the remaining photon counts using a customized analysis software written in LabView (National Instruments).

3.2.5 Two-Photon Absorption Measurement

The two-photon absorption (TPA) spectrum was measured using two-photon induced fluorescence (TPIF) spectroscopy. The Rhodamine 6G and AIE dot solution were degassed before measurements. The samples were excited with laser pulses of 100 fs produced by the mode-locked Ti:Sapphire laser (Spectraphysics Tsunami) with a repetition rate of 82 MHz, and a femtosecond optical parametric amplifier (OPA) was used within the spectral range of 800-960 nm. The emission for the AIE dot aqueous suspensions were collected at a 90^{o} angle by a high numerical aperture lens and directed to a spectrometer's entrance slit. Rhodamine 6G in methanol was used as the reference. TPA cross-sections (δ) were calculated from the following equation:[2]

$$\frac{\delta_2}{\delta_1} = \frac{F_2 \eta_1 c_1 n_1}{F_1 \eta_2 c_2 n_2}$$

where δ_1 and δ_2 are the TPA cross-sections, F_1 and F_2 are the TPFI intensities, η_1 and η_2 are the fluorescence quantum yields, c_1 and c_2 are the concentrations, n_1 and n_2 are the refractive indexes of solvents (1 corresponds to Rhodamine 6G, 2 is AIE dot). The concentration of AIE dot suspension is calculated on the basis of dot as described in the previous chapter.

3.2.6 Blood Vascular Imaging

The right ears of the mice were pre-treated with 40 ul of 1% croton oil (C6719, Sigma) (in acetone) for different durations to induce inflammation with varying

severities. Control contralateral left ears were treated with only 40 ul of vehicle (acetone). Just before imaging, mice were anesthetized with 8 μL/g mouse bodyweight of 150 mg/kg ketamine and 10 mg/kg xylazine. Hair was thoroughly removed using Veet hair removal cream (Reckitt Benckiser), before placing the ear on a custom built heating platform that maintained the temperature of the mouse ear at 35 ℃. Mice were placed on a heating pad to maintain a core body temperature of 37 ℃ throughout each imaging procedure. AIE-Gd dots (4 μL/g mouse bodyweight) at the concentration of 100 nM based on dot concentration were administered intravenously via retro-orbital injection prior to imaging. All procedures were performed under the institution's IACUC (Institutional Animal Care and Use Committee) guidelines. A TriM Scope II single-beam two-photon microscope (LaVision BioTec) with a tuneable 680-1080 nm laser was used to acquire the images.

3.2.7 Evans blue Detection

AIE-Gd dots (4 μL/g mouse bodyweight at 100 nM) and Evans blue (4 μL/g mouse bodyweight of 20 mg/ml) were mixed together and co-injected, immediately before croton oil treatment. After the pre-designated time (1, 3, 5, 7 h), the mice were sacrificed by carbon dioxide asphyxiation, and blood was flushed by perfusing 10 ml of PBS via the right ventricle of the mouse heart, while the vena cava was cut. The mouse ears were collected using a 2 cm by 0.7 cm stencil to ensure consistent sizes of samples retrieved. Evans blue dye was then extracted from the ears by N,N-dimethylformamide (DMF) (D4451, Sigma) and the content of Evans blue in each ear was determined by measuring the absorbance at 620 nm.

3.2.8 Gd Contents Detection

After extraction of Evan blue, the obtained ears from mouse were collected and nitrified by the nitric acid (70%) under heating. After the ears were completely

decomposed, the samples were dissolved in 5% nitric acid for ICP-MS analysis. The contents of Gd remaining in the mouse ears were then quantitatively determined by the standard curve.

3.3 Results and Discussion

3.3.1 Fabrication of AIE-Gd Dots

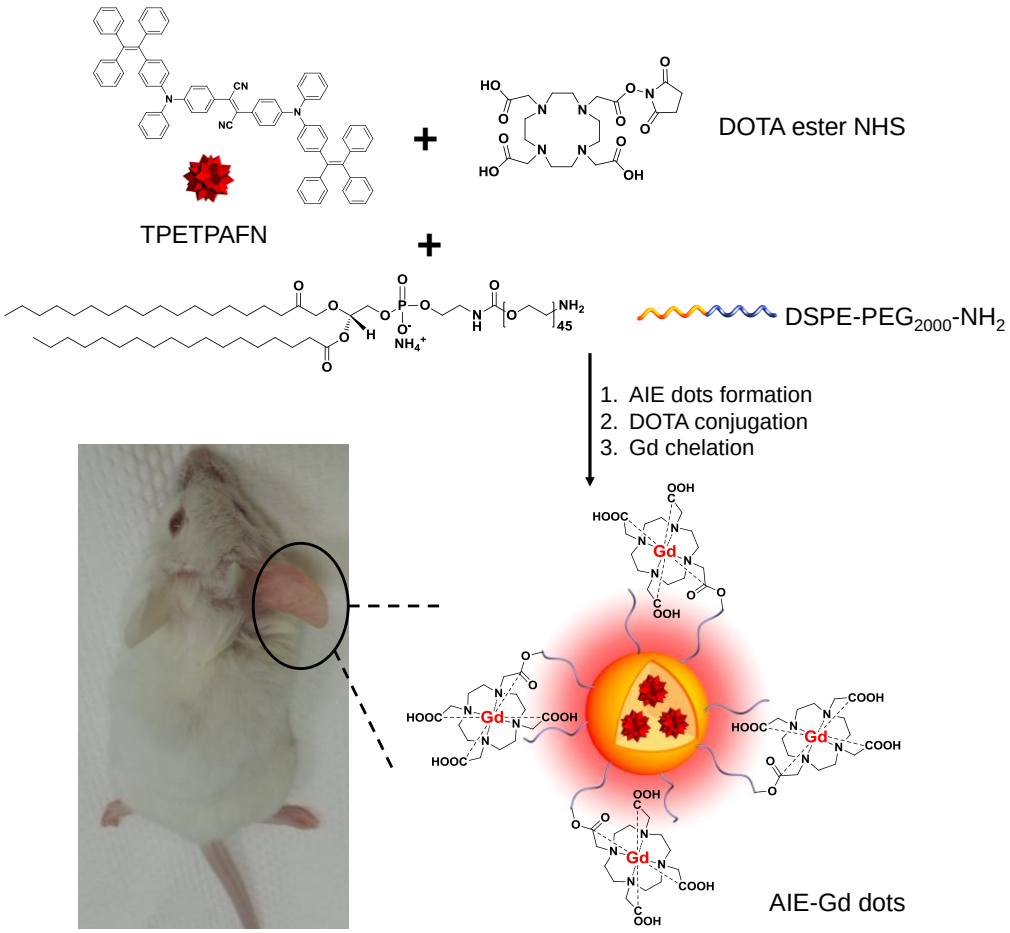

Scheme 3.1. Chemical structures of DSPE-PEG_{2000}-NH_2, TPETPAFN and DOTA, and the schematic illustration of AIE-Gd dots formation.

2,3-Bis(4-(phenyl(4-(1,2,2-triphenylvinyl)phenyl)amino)phenyl)furmaronitrile (TPETPAFN) (Scheme 3.1) was synthesized according to literatures.[115] The AIE dots were fabricated via a modified nano-precipitation methods with the assistance of ultrasound sonication. An amphiphilic block copolymer, 1,2-distearoyl-sn-glycero-3-phosphoethanolamine-N-[amino(polyethylene glycol)-2000] (DSPE-PEG_{2000}-NH_2)

was used as the matrix to load TPETPAFN molecules to form AIE dots. The detailed procedures were described in previous chapter. Upon AIE dots formation, the hydrophobic DSPE segments of the matrix will intertwine with TPETPAFN molecules to form the core, while amine group terminated polyethylene glycol (PEG) chain render outside towards water phase, rendering AIE dots with surface amino group for further functionalization with gadolinium (Gd^{3+}). After obtain the AIE dots, 2,2',2''-(10-(2-((2,5-dioxopyrrolidin-1-yl)oxy)-2-oxoethyl)-1,4,7,10-tetraazacyclododecane-1,4,7-triyl)triacetic acid (DOTA-NHS ester) was conjugated to AIE dot surface. Gd^{3+} was then chelated to AIE dot surface through DOTA moiety to render AIE-Gd dots with dual modal functionality.

3.3.2 Characterization of AIE-Gd Dots

The encapsulated TPEPTAFN is calculated to be ~31.7 wt%, equivalent to ~4400 TPETPAFN molecules per dots. Such a high AIE fluorogen density ensures the high brightness of the AIE dots. Ion coupled plasma-mass spectrometry (ICP-MS) was used to quantify the Gd^{3+} content in the finally obtained AIE-Gd dots. The result revealed the AIE-Gd dots contain 2.3 wt% of Gd^{3+}, which is estimated to be equivalent to 2100 Gd^{3+} ions per AIE-Gd dots. Laser light scattering (LLS) was further applied to access the size distribution of AIE-Gd dots, which revealed that the AIE-Gd dots have an average hydrodynamic size 38.9 ± 2.6 nm with narrow size distribution and a polydispersity of ~0.109 (Figure 3.1A). High-resolution transmission electron microscopy (HR-TEM) shows the morphologies of the AIE-Gd dots, which are in spherical shapes with size around 36 nm (Figure 3.1B).

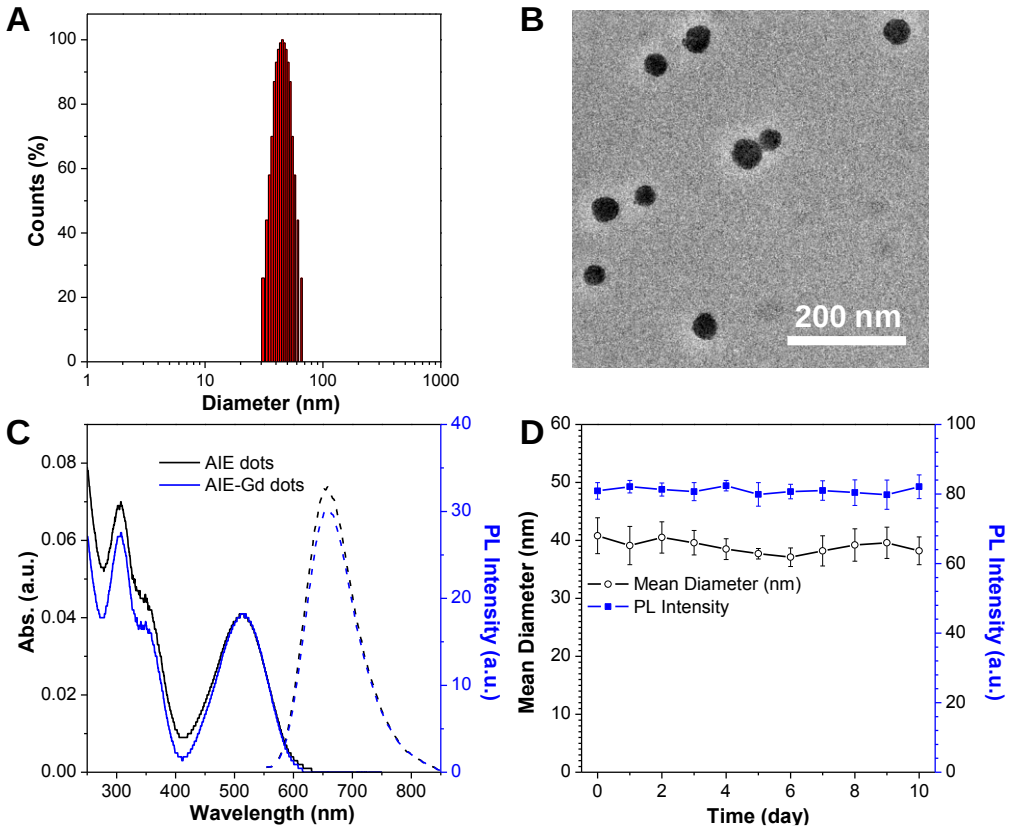

Figure 3.1. A) LLS result, and B) TEM image of AIE-Gd dots. C) Absorption and PL spectra of AIE-Gd dots before and after Gd chelation. D) Hydrodynamic size and fluorescence changes of AIE-Gd dots in 1× PBS buffer.

The AIE-Gd dots in water suspension showed absorption and emission peaks centred at 512 and 670 nm, respectively, with a high quantum yield (η) of 24% measured with 4-(dicyanomethylene)-2-methyl-6-(p-dimethylaminostyryl)-4H-pyran in methanol as the standard (Figure 3.1C). It should be noted that Gd^{3+} chelation showed negligible effects on the optical properties as the absorption and emission spectra of the AIE dots are hardly affected by chelation process, indicating high stability of the dots towards surface functionalization. Moreover, the size and fluorescence of the AIE-Gd dots remain almost unchanged after 7 days incubation in 1× phosphate-buffered saline (PBS) buffer (Figure 3.1D), further indicating the high colloidal stability of AIE-Gd dots in biological buffer. Such a high colloidal stability should be contributed by the existence of PEG chains, which suppress the nonspecific interaction between these

AIE-Gd dots as well as the interaction between AIE-Gd dots and surrounding biomolecules, making them promising for the *in vivo* vascular imaging.

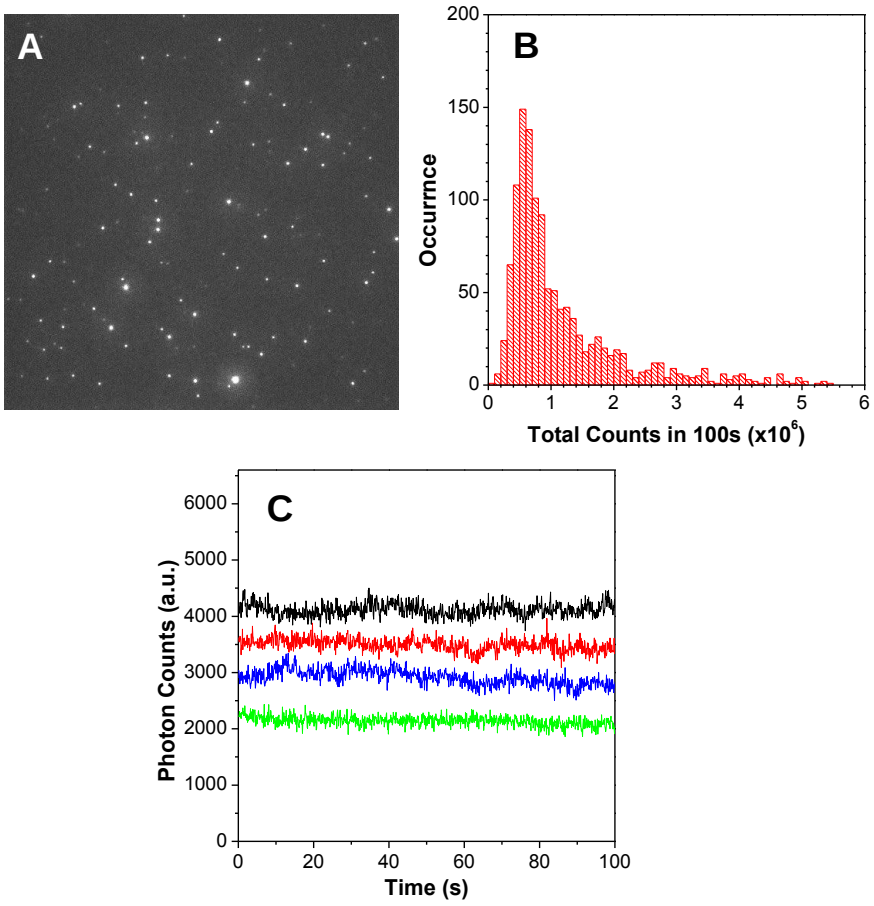

Figure 3.2. A) Luminescence image, B) luminescence intensity histogram, C) representative luminescence intensity time-traces of TPETPAFN loaded AIE dots.

The brightness and photostability of AIE dots were further studied by the single particle fluorescence imaging experiment using wide-field fluorescence microscope. The wide-filed fluorescence image of these individual AIE dots was shown in Figure 3.2A, which showed very bright and uniformly distributed fluorescence. The corresponding histograms of total number of photons emitted by these 1216 representative AIE dots within 100s show an average emitted photon number of 1.18 $\times 10^6$ counts (Figure 3.2B), which is much higher than selected benchmark (QD655, 2.8×10^5 counts), indicating the high brightness of the AIE dots. Continuous laser irradiation was used to study the photostability of AIE dots. The real-time fluorescence

intensity of four individual AIE dots were collected by the integration of the emission of these dots over 100 ms for 1000 consecutive frame. The results are shown in Figure 3.2C, where negligible effects to the fluorescence intensity of 4 representative AIE dots was observed under the continuous laser scanning, indicating high resistance of AIE dots towards photobleaching. In addition, no blinking or intermittency was observed for all AIE dots (Figure 3.2C), such a stable fluorescence further make them a promising candidate for real-time single dot tracing, as well as red blood cells (RBCs) flow measurement and other applications.

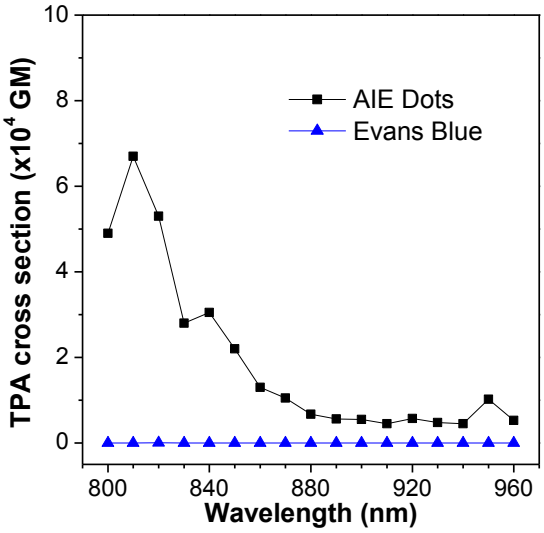

Figure 3.3. Two-photon absorption spectrum of AIE dots in water.

Materials with high TPA cross section are able to emit strong visible fluorescence from low-energy irradiation in the NIR region, which minimizes the absorbance of biosubstrate, and is beneficial for clear intravital imaging at high resolution levels. The TPA spectrum of AIE-Gd dots in aqueous solution was measured using a TPFI microscope with a tunable Ti:sapphire laser, using Rhodamine 6G in methanol as the standard. As a comparison, Evans blue, a commonly used blood vascular imaging contrast and inflammation detection probe, is also selected for the TPA measurement. The emission signals of AIE-Gd dots and Evans blue were collected

upon excitation from 800 to 920 nm, and their corresponding TPA spectra were shown in Figure 3.3. As shown, the maximum TPA cross section (δ) value of AIE-Gd dots is measured to be 6.7×10^4 GM (based on dots concentration) upon excitation at 810 nm, which is much higher than that of Evans blue. Such a high TPA cross section of AIE-Gd dots in aqueous media is highly desirable for high resolution intravital imaging.

3.3.3 Inflammation Imaging

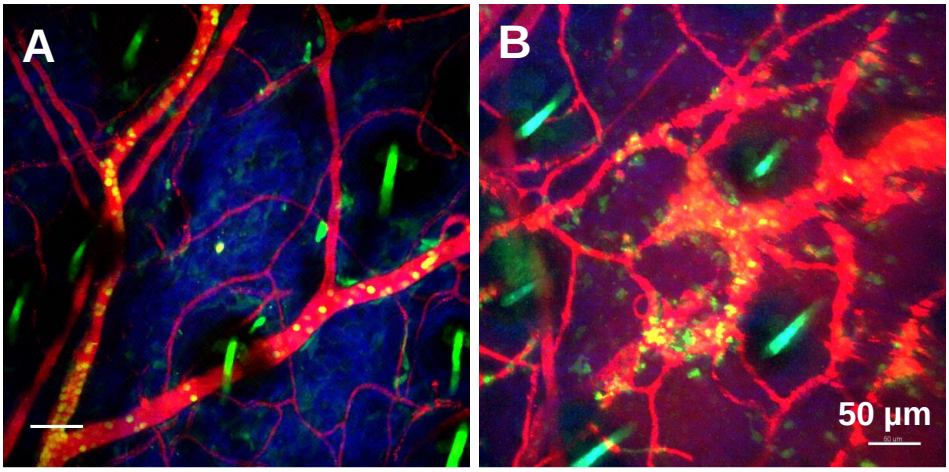

Figure 3.4. Intravital TPFI of mouse ears A) without or B) with inflammation. The inflammatory ear was first treated with 1% croton oil (40 μL) for 3 h, followed by AIE-Tat dots injection, and immediate imaging.

Real-time two-photon inflammation detection and imaging in transgenic live mice with AIE-Gd dots is investigated using an intravital two-photon microscope. The neutrophils of the mice are green fluorescent protein (GFP) gene modified to provide green fluorescence. Croton oil that can cause irritation and swelling was used to induce mouse ear inflammation. After treatment the left ear with 40 μL of croton oil for 3 h, AIE-Gd dots (100 nM, 40 μL/gram of mouse weight) were administered intravenously prior to two-photon fluorescence imaging. Figure 3.4 shows the images of ear blood vessels of healthy ear, and inflammation ear, respectively. As shown, the major blood vessels as well as the smaller capillaries in the pia meter could be clearly visualized by red fluorescence originated from AIE-Gd dots. Owing to the PEG segment of the dot

surfaces, nonspecific binding is blocked, the AIE dots showed excellent colloidal stability in blood vessels, and therefore, smooth flow and negligible large AIE dots aggregates in health blood vascular were observed. Moreover, neither obvious leakage of AIE-Gd dots from blood vessels nor increase of background signal could be observed within tested period (over 30 min), revealing the excellent vascular retention ability of AIE-Gd dots, which outperforms Evans blue, which showed significant leakage even in moral healthy blood vessels. On the contrary, two-photon fluorescence image of croton oil treated inflammatory ear is quite different. As observed in Figure 3.4B, lots of red fluorescence outside vascular was observed. These AIE-Gd dots not only tend to leak out from the blood vessel and diffuse into surround tissue, but also are able to bind the outer layer of the blood vessels in the inflammatory ear. The accumulation of green fluorescence neutrophils in the inflammation ear was also observed, which further indicates that our AIE-Gd dots have the capability to detect and image the vascular leakage induced by inflammation.

In a parallel experiment, we performed the croton oil treatment and the intravenously injection of AIE-Gd dots (40 μL/gram of mouse weight) at the same time. And the two-photon fluorescence imaging was conducted at 3 h post-injection. The results are shown in Figure 3.5. As shown, almost no red fluorescence from blood vascular can be observed for healthy ear under the same imaging condition. The result clearly indicates the excellent clearance of our AIE dots, as very weak red fluorescence in observed in blood vascular at 3-h post-injection. The absence of red fluorescence in the healthy ear also revealed that our AIE dots will not leak outside from the blood vascular, providing extremely low background signal. On the other hand, as for the inflammatory ear, bright red fluorescence was observed from the inside and outside of blood vascular, providing a clear visualization of inflammations. The excellent

inflammation imaging and quick clearance make our AIE dots an ideal candidate for inflammation imaging in practical applications.

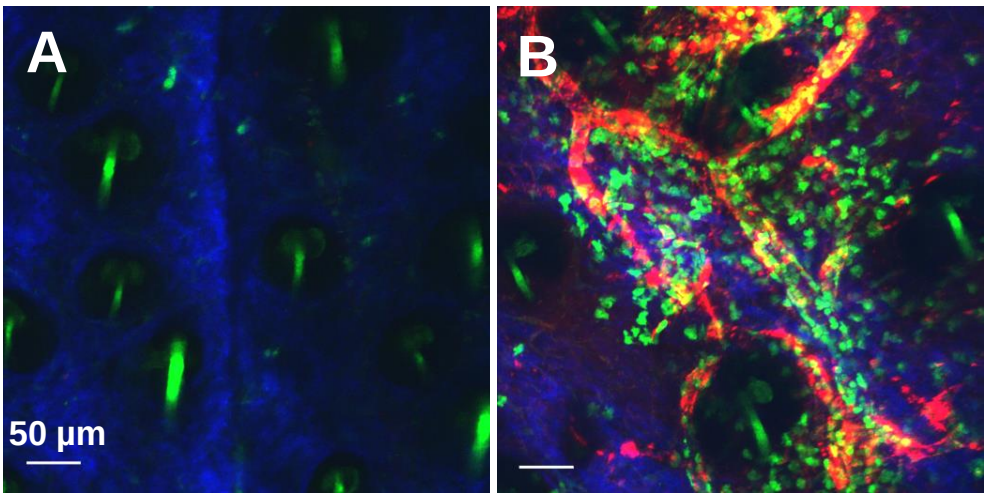

Figure 3.5. Intravital TPFI of mouse ears A) without or B) with inflammation. The croton oil treatment and AIE dots injection were conducted as the same time. At 3 h post-injection, croton oil is removed, and the images were obtained.

3.3.4 Quantification of Vascular Leakage

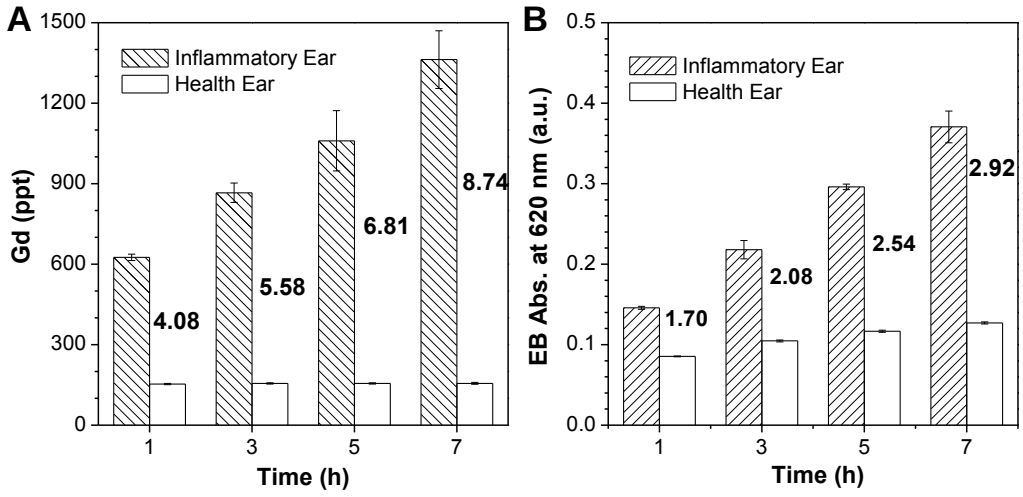

Figure 3.6. A) Amount of Gd and B) absorption of Evans blue in inflammation and healthy ears after designated croton oil treatment. The AIE-Gd dots and Evans blue was injected at the starting time of croton oil treatment.

We subsequently utilized the contents of Gd^{3+} remaining in the ear to quantitatively determine the severity of inflammation, using Evans blue as the benchmark. The croton oil treatment, and the injection of AIE-Gd dots and Evans blue

were conducted simultaneously. The mice were sacrificed at 1, 3, 5 and 7 h post-injection. The blood was flashed and the ears were cut for analysis. *N,N*-dimethylformamide (DMF) was used to extract Evans blue from the ear, and the amount of remaining Evans blue in the ear was evaluated by measuring its absorption at 620 nm. The ears were further nitrified, the amount of residue Gd^{3+} was accessed by ICP-MS. As shown in Figure 3.6A, Gd^{3+} content in the 1 h croton oil treated inflammatory ear is ~4.8-fold of that in the healthy ear of the same mouse, while Evans blue only showed less than 2-fold increase (Figure 3.6B). Moreover, upon increase the inflammation severity to 7 h croton oil treatment, the Gd^{3+} content difference between inflammation ear and healthy ear increases to over 8 fold, while the Evans blue difference is less than 3-fold. These results clearly indicate that our AIE-Gd dots have higher sensitivity than traditional measurement of Evans blue absorption method for inflammation detection. In addition, upon increasing the croton oil treatment, the Gd^{3+} content in the healthy ear remains almost the same, while Evans blue showed gradually increased absorbance, indicating that our dots have better vascular retention than Evans blue, which helps to provide a higher sensitivity and lower background signal, and a clear and direct visualization of inflammation.

3.3.5 Real-Time Monitoring of Vascular Leakage

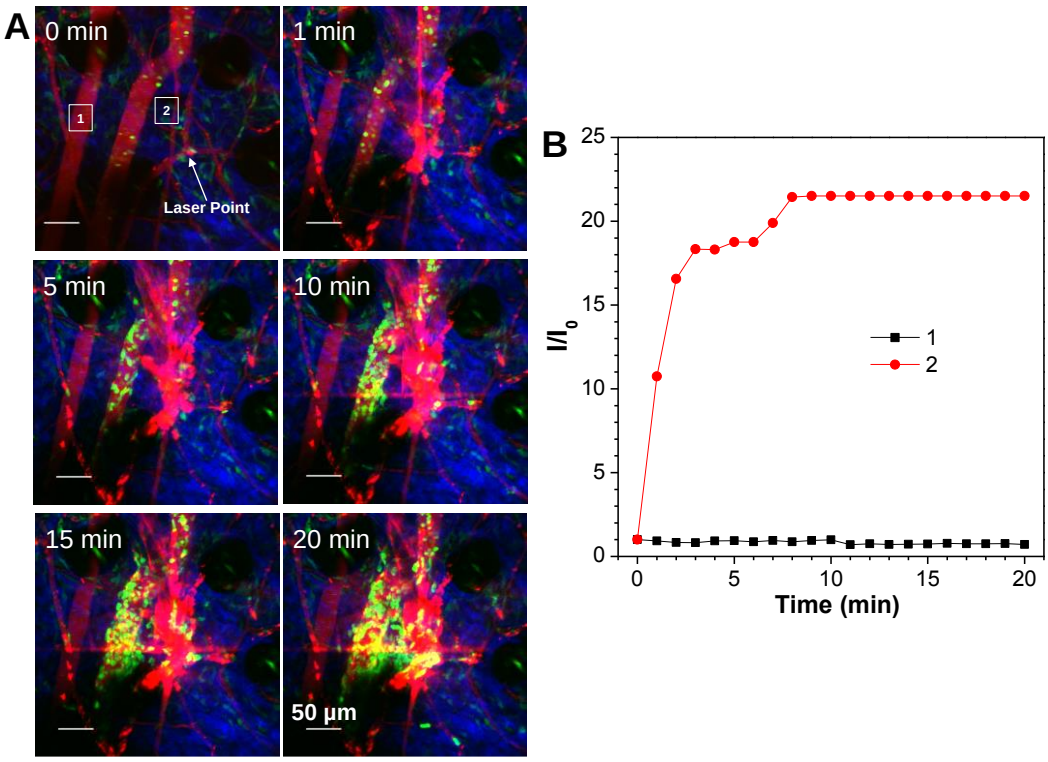

Figure 3.7. A) Time-lapse images of AIE-Gd dots treated mouse ear before and after laser burn. B) Fluorescence intensity changes of selected two areas before and after laser burn. The neutrophils are GFP genetically modified.

To real time monitoring the leakage of AIE-Gd dots upon inflammation or injury, the mouse was intravenously injected with our dots, followed by blood vascular imaging. In the duration of imaging, the selected area is burned by an intense laser beads, and the leakage of AIE-Gd dots was monitoring by the TPFI microscope. As shown in the Figure 3.7A, upon laser burning, a quick accumulation of red fluorescence in the burnt area is observed, which is even faster than the accumulation of neutrophils. We also monitored the fluorescence changes during the injury imaging. As shown, the fluorescence in the burnt areas quick increased over 20-fold within 10 min, while the blood vessel away from it showed unchanged fluorescence intensity. The results further reinforced that our AIE-Gd dots could be utilized for facile real time inflammation or injury detection and imaging.

3.4 Conclusion

In conclusion, this chapter presented a general approach to introduce more functional materials or modalities to AIE dots, and demonstrated their *in vivo* applications for detection and imaging of blood vascular integrity and leakage. Benefiting from the high brightness of AIEgens in aggregates, organic AIE dots with strong red emission and photostability under two-photon excitation were successfully fabricated. Gadolinium was further chelated onto the AIE dots surface to yield AIE-Gd dots with dual modalities. The Gd chelation did not affect the optical properties of AIE dots, and they exhibit excellent stability in biological environment. Upon intravenously injection into mouse, the blood vascular will be light up, clearly and distinguishable red fluorescence with weak background signal from outside blood vessel can be observed under two-photon excitation. Under inflammation, the vascular permeability will increase, and our AIE dots will leak outside from the blood vascular, serving as an *in vivo* fluorescence marker for blood vascular integrity and leakage. Moreover, the Gd contents chelated onto the AIE dots can also provide the quantitatively analysis of the leakage, providing a guidance of the inflammation severity.

CHAPTER 4

ORGANIC DOTS WITH AGGREGATION-INDUCED EMISSION CHARACTERISTICS FOR TARGETED AND IMAGE-GUIDED PHOTODYANMIC THERAPY

4.1 Introduction

Image-guided therapy that combines the diagnostic and therapeutic effects into one delivery system has shown its own advantage and attracted great attentions in biological researches and practical applications.[137, 138] Among these developed image-guided therapy systems, photodynamic therapy (PDT) that utilizes a beam of light, oxygen, and photosensitizers (PSs) to produce reactive oxygen species (ROS) that are toxic to tumor has been served as an elegant approach for cancer therapy.[139] The therapeutic effects of PDT can be readily and precisely controlled by the location of the light beam with high spatiotemporal precision and noninvasive properties.[140, 141] In addition, these PSs are also able to emit fluorescence under light illumination, providing the chance for visualization of the tumor location and the therapeutic effects.[142] However, as conventional fluorogens, most PSs, such as the widely used porphyrin derivatives are readily to aggregate due to their large hydrophobicity and the rigid planar chemical structures. This π–π stacking in aggregate states always resulted in quenched fluorescence and reduced ROS generation.[143, 144] When being encapsulated or loaded into nanoparticles (NPs), this quenching and reduction phenomena are even more severe, largely compromising their PDT performance.[86] Many effects have been put on to fight against this,[145-147] but this natural process of aggregation for fluorogens and PSs is inevitable, and hence it holds great potentials to design new class of PSs showing efficient ROS generation in aggregate states.

We have demonstrated that the fluorogens with aggregation-induced emission characteristics (AIEgens) are able to emit strong fluorescence in aggregates or be encapsulated into nanoparticles.[74, 148, 149] Such unique and exciting properties of AIEgens make it possible for design of AIE light-up probes and AIE dots for biological sensing and imaging.[150-155] In addition, several AIEgens have been applied in PDT, but

they only served as energy donor to enhance the ROS generation of porphyrin derivatives.[55, 156, 157] And there has been no report on AIEgens that inherently possess the ROS generation capability.

In this chapter, for the first time, we demonstrated that AIEgens can not only show bright fluorescence but also be able to efficiently generate ROS in aggregates. Such properties make them the ideal candidates for image-guided PDT. Using 2-(2,6-bis((*E*)-4-(phenyl(4′-(1,2,2-triphenylvinyl)-[1,1′-biphenyl]-4-yl)amino)styryl)-4*H*-pyran-4-ylidene)malononitrile (TPETPADCM) as an example, we fabricated the organic AIE dots using 1,2-distearoyl-*sn*-glycero-3-phosphoethanolamine-*N*-[maleimide(polyethylene glycol)] (DSPE-PEG_{2000}-Mal) as encapsulation matrix. The resultant AIE dots is further conjugated with cyclic arginine-glycine-aspartic acid (cRGD) peptide, which can selectively target the cancer cells with integrin overexpress for targeted and image-guided PDT. The TPETPADCM-cRGD dots can generate ROS very efficiently under appropriate light irradiation, which showed selective cellular uptake and toxicity to targeted MDA-MB-231 cells upon light irradiation while keeping control cells intact.

4.2 Experimental

4.2.1 Materials

1,2-Distearoyl-sn-glycero-3-phosphoethanolamine-N-[maleimide(polyethylene glycol)-2000] (DSPE-PEG_{2000}-Mal) was purchased from Avanti Polar Lipids, Inc. 3-(4,5-Dimethylthiazol-2-yl)-2,5-diphenyltetrazolium bromide (MTT) and other unmentioned chemicals were all purchased from Sigma-Aldrich and used as received without further purification. Thiolated cyclic (Arg-Gly-Asp-D-Phe-Lys(mpa)) peptide (c(RGDfK)) was customized from GL Biochem Ltd

(Shanghai). Dulbecco's Modified Essential Medium (DMEM) is a commercial product of National University Medical Institutes (Singapore). Milli-Q water was supplied by Milli-Q Plus System (Millipore Corporation, Breford, USA). 10× phosphate-buffer saline (PBS) buffer with pH = 7.4 (ultrapure grade) is a commercial product of 1st BASE (Singapore). Milli-Q water (18.2 MΩ) was used to prepare the buffer solutions from the 10× PBS stock buffer. 1× PBS contains NaCl (137 mM), KCl (2.7 mM), Na_2HPO_4 (10 mM), and KH_2PO_4 (1.8 mM). Fetal bovine serum (FBS) and trypsin-EDTA solution were purchased from Gibco (Life Technologies, AG, Switzerland). Annexin V-FITC apoptosis detection kit was also purchased from Life Technologies.

4.2.2 Characterization

Particle size and size distribution were determined by laser light scattering (LLS) with a particle size analyzer (90 Plus, Brookhaven Instruments Co., USA) at a fixed angle of 90 °at room temperature. TEM images were obtained from a JEOL JEM-2010 transmission electron microscope with an accelerating voltage of 200 kV. UV-vis absorption spectra were taken on a Milton Ray Spectronic 3000 array spectrophotometer. Photoluminescence (PL) spectra were measured on a Perkin-Elmer LS 55 spectrofluorometer. All UV and PL spectra were collected with quarz cuvette at 24 ±1 ℃.

4.2.3 Preparation of AIE Aggregates

2-(2,6-Bis((*E*)-4-(phenyl(4′-(1,2,2-triphenylvinyl)-[1,1′-biphenyl]-4-yl)amino)styryl)-4*H*-pyran-4-ylidene)malononitrile (TPETPADCM) was synthesized according to previous reports. AIEgens were firstly dissolved in THF to make the stock solution at a concentration of 0.1 mM. To form the AIE aggregates, 1 mL of THF stock solution were added into 10 mL MilliQ water under string at 600 rpm. After THF evaporation, the aggregates were obtained at concentration of 0.01 mM.

4.2.4 ROS Measurement in Solution

Dichlorofluorescin (DCFH) was used as the indicator for ROS generation measurement in solution. To prepare DCFH, 0.5 mL of 1 mM 2'-7' dichlorofluorescin diacetate (DCFH-DA, signal) in ethanol solution is added into 2 mL of 0.01 NaOH solution. And the mixture is placed at room temperature for 30 min. The hydrolysate is further neutralized with 10 mL of 25 mM PBS buffer. The DCFH is stored on ice in dark before use. To measure ROS generation, DCFH is added into the solution of AIE aggregates to obtain a working concentration of 40 μM. the mixture is exposed to light irradiation for different time, and the emission spectra of the mixture is obtain upon excitation at 460 nm. The enhancement fold of the DCFH fluorescence intensity at 530 nm is used to quantify the ROS generation efficiency. 1,3-diphenylisobenzofuran (DPBF) that quickly reacts with ROS with reduced absorbance was also used for measuring the ROS generation of AIE dots.

4.2.5 Preparation of TPETPADCM Loaded AIE Dots

DSPE-PEG_{2000}-Mal (2 mg) and TPETPADCM (1mg) were fully dissolved in 1 mL THF solution, which was then poured into water (10 mL). This was followed by sonicating the mixture for 2 minutes at 12 W output using a microtip probe sonicator (XL2000, Misonix Incorporated, NY). The mixture was then stirred at room temperature overnight to evaporate the organic solvent. The NP suspension was further filtered with a 0.2 μm syringe filter to obtain TPETPADCM AIE dots.

4.2.6 Conjugation of cRGD to TPETPADCM Dots

Thiolated cRGD was conjugated to the surface of TPETPADCM dots (denoted as TPETPADCM-cRGD dots) as the following procedure. The TPETPADCM dots were suspended in HEPES buffer (0.2 mg mL^{-1}) and incubated with excess thiolated cRGD at room temperature for 6 h. Then the cRGD functionalized nanoparticles were

washed with Milli-Q water (3 mL ×3 times) by ultrafiltration (20,000 MWCO, Amicon, Millipore Corporation, Bedford, USA), suspended in Milli-Q water and stored at 4 ℃ for further use.

4.2.7 Cell Culture

The breast cancer cell line MDA-MB-231, MCF-7 and normal cell line NIH 3T3 were provided by American Type Culture Collection (ATCC). The cells were cultured in DMEM (Invitrogen, Carlsbad, CA) containing 10% heat-inactivated FBS (Invitrogen), 100 U mL^{-1} penicillin, and 100 μg mL^{-1} streptomycin (Thermo Scientific) and maintained in a humidified incubator at 37 ℃ with 5% CO_2. Before experiment, the cells were precultured until confluence was reached.

4.2.8 Intracellular ROS Detection

ROS generation inside cells under light irradiation was detected using dichlorofluorescein diacetate (DCF-DA) cellular reactive oxygen species assay kit (Abcam). MDA-MB-231, MCF-7 and NIH 3T3 cells were cultured in the chambers (LAB-TEK, Chambered Coverglass System) at 37 ℃. After 80% confluence, the culture medium was removed and washed twice with PBS buffer. Following incubation with TPETPADCM-cRGD dots (10 μg mL^{-1}) for 1 h in the dark, DCF-DA was loaded into the cells. After 10 min incubation, cells were washed twice with PBS and then exposed to light irradiation for 10 s at the power density of 0.25 W cm^{-2}. After irradiation, the medium was replaced with PBS and fluorescence images of treated cells were acquired using a laser confocal microscope.

4.2.9 Confocal Imaging

MDA-MB-231, MCF-7 and NIH 3T3 cells were cultured in the chambers at 37 ℃. After 80% confluence, the culture medium was removed and washed twice with

PBS buffer. Following incubation with TPETPADCM-cRGD dots (10 μg mL^{-1}) for 1 h, the cell nucleus were living stained with Hoechst 33342 (Life Technologies), following the standard protocol of the manufacturer. The cellular apoptosis imaging measurement was carried out based on standard detection kit (Annexin V-FITC Apoptosis Detection Kit) according to manufacturer's protocol. The cells were then imaged immediately by confocal laser scanning microscope (CLSM, Zeiss LSM 410, Jena, Germany). The images were analysed by Image J 1.43 × program (developed by NIH, http://rsbweb.nih.gov/ij/).

4.2.10 Cytotoxicity Studies

3-(4,5-Dimethythiazol-2-yl)-2,5-diphenyltetrazolium bromide (MTT) assays were used to assess the metabolic activity of MDA-MB-231, MCF-7 and NIH 3T3 cells. The cells were seeded in 96-well plates (Costar, IL, USA) at an intensity of 4×10^4 cells mL^{-1}. After 24 h incubation, the medium was replaced with the TPETPADCM-cRGD dots at different concentrations and incubated at 37 ℃. Following incubation with TPETPADCM-cRGD dots for 1 h, cells were washed twice with PBS and then exposed to light irradiation for 2 min at the power density of 0.25 W cm^{-2}. The cells were further incubated for 24 h and then washed twice with 1× PBS buffer, and 100 μL of freshly prepared MTT (0.5 mg mL^{-1}) solution in culture medium was added into each well. The MTT medium solution was carefully removed after 3 h incubation in the incubator at 37 °C. DMSO (100 μL) was then added into each well and the plate was gently shaken to dissolve all the precipitates formed. The absorbance of MTT at 570 nm was monitored by the microplate reader (Genios Tecan). Cell viability was expressed by the ratio of absorbance of the cells incubated with TPETPADCM-cRGD dots to that of the cells incubated with culture medium only. The relative cell survival percentages compared to the dots-free control were plotted against the drug

concentration in logarithmic scale. The data reported represent an average of three measurements from different batches. The dose-effect profiles were obtained by sigmoidal logistic fitting by use of Origin 8.0 (OriginLab, Northampton, MA) and the half-maximal inhibitory concentration (IC_{50}) values were determined on the basis of the fitted data.

4.3 Results and Discussion

4.3.1 Synthesis and Characterization of TPETPADCM

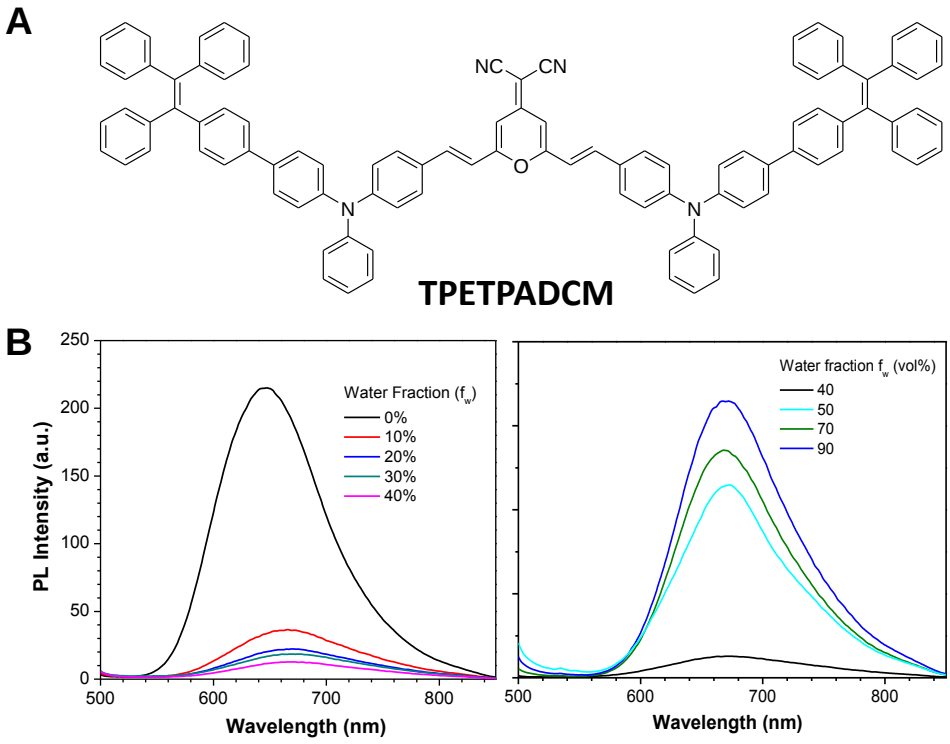

Figure 4.1. A) Chemical structure of TPETPADCM. B) PL spectra of TPETPADCM (λ_{ex} = 502 nm) in THF/water mixtures with different water fractions (f_w).

We synthesized TPETPADCM according to our previous report, and the structure is shown in Figure 4.1A.[74] The AIE characteristics of TPETPADCM was firstly study by measuring its photoluminescence (PL) spectra in THF and water mixtures with different water fractions (f_w) (Figure 4.1B). In pure THF solution, TPETPADCM shows moderate fluorescence. Upon gradual increase f_w (from 0 to 40%),

the emission of TPETPADCM is dramatically weakened and the emission color is bathochromically shifted, due to the increase in the solvent polarity and the transformation to the twisted intramolecular charge transfer (TICT) state. Upon further increasing f_w over 40 vol %, the light emission of TPETPADCM is invigorated and is intensified with a further increase in f_w, indicating that TPETPADCM is an AIE active luminogen.[74, 149]

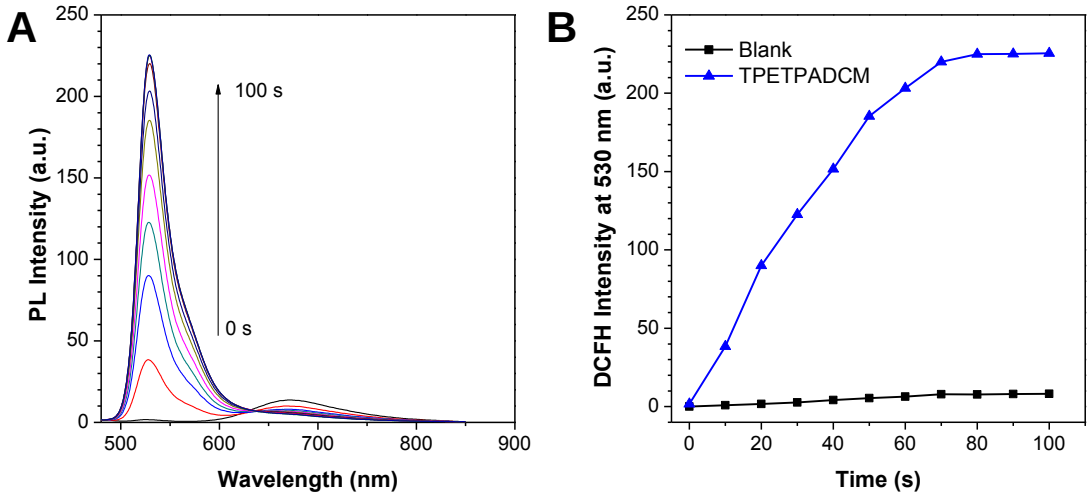

Figure 4.2. A) PL spectra of the mixture of TPETPADCM aggregates and DCFH. B) DCFH PL peak intensity changes under continuous light irradiation.

To demonstrate the ROS generation capability of TPETPADCM in aggregates, we used dichlorofluorescin (DCFH) as the indicator. DCFH can readily react with ROS to result in increased emission at 530 nm. As shown in Figure 4.2A, exposure the mixture of TPEPTADCM aggreagtes and DCFH to whit light irradiation, the emission of DCFH at 530 nm will quickly increase. The fluorescence intensity enhancement of DCFH is over 200-fold (Figure 4.2B). In addition, only exposure DCFH itself to light irradiation, almost on change of its fluorescence intensity is observed, excluding the possibility of DCFH as the PSs. These results clearly demonstrated that TPETPADCM can efficiently generate ROS in the aggregated state.

4.3.2 Synthesis and Characterization of TPETPADCM-cRGD Dots

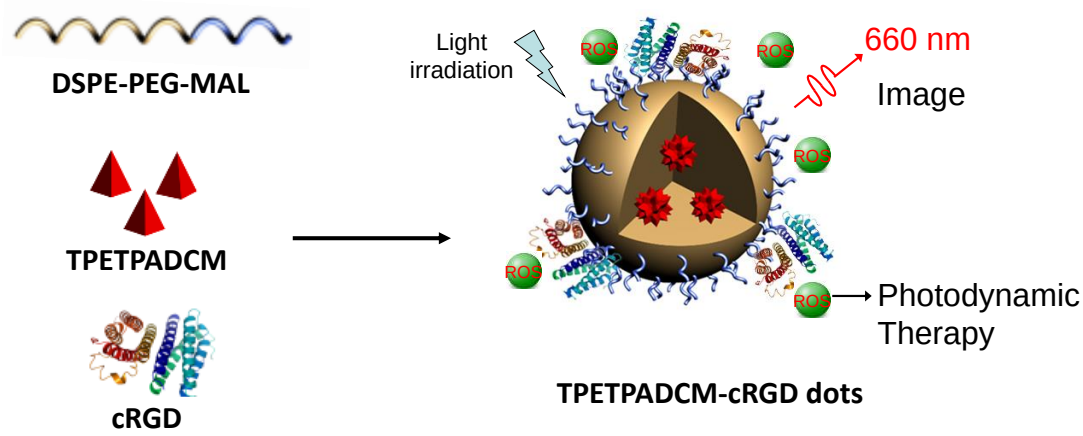

Scheme 4.1. Schematic illustration of TPETPADCM-cRGD dots for image-guided photodynamic therapy.

The TPETPADCM dots were prepared using DSPE-PEG_{2000}-Mal as the encapsulation matrix following the nano-precipitation method as described in the previous chapters. Upon transferring them from THF to water phase, the hydrophobic DSPE segment will intertwine TPETPADCM to form the core, while hydrophilic PEG chains will render outside towards water phase and provide the surface maleimide group for further conjugation. The targeting moiety towards cancer cells with overexpressed $\alpha_v\beta_3$ integrin, cRGD-SH, was then conjugated to the TPETPADCM dot surface through click chemistry between the surface maleimide and -SH to yield the TPETPADCM-cRGD dots (Scheme 4.1).

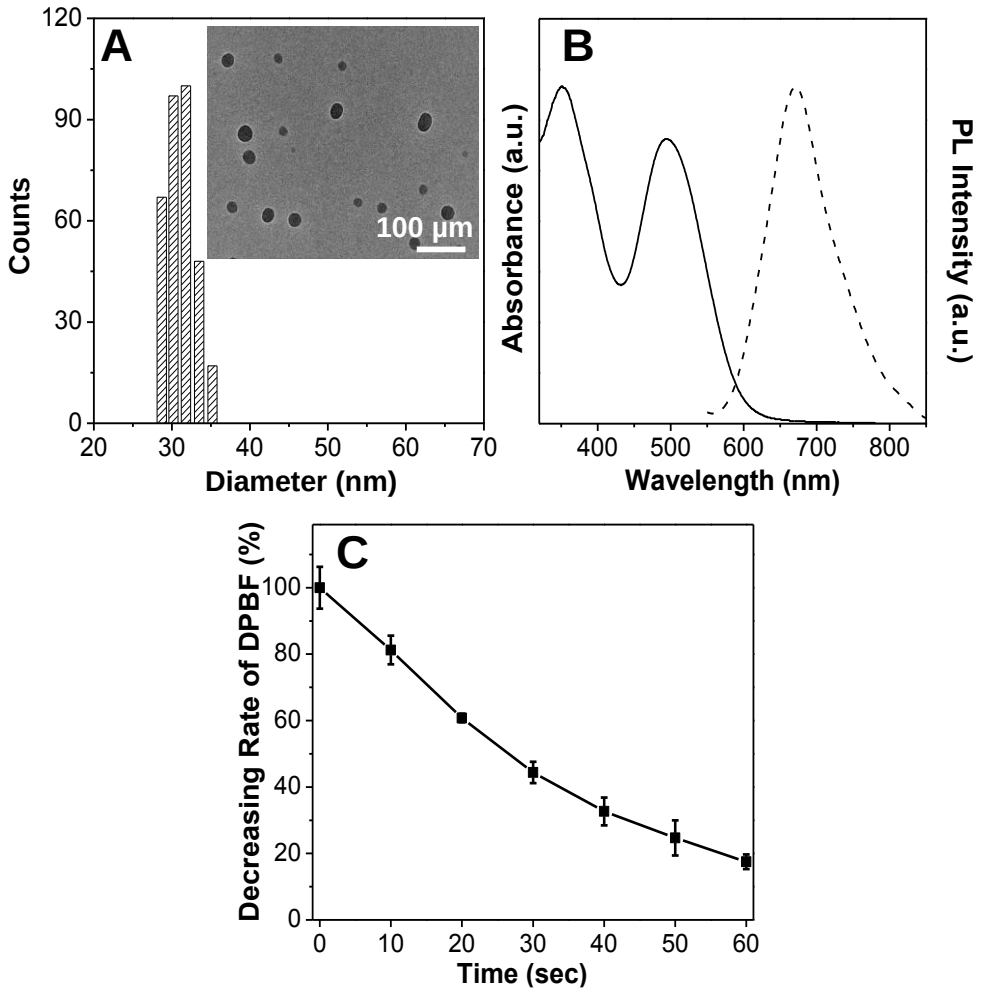

Figure 4.3. A) Size distribution and TEM image (inset), B) absorption and emission spectra, and C) ROS generation of TPETPADCM-cRGD dots.

Laser light scattering (LLS) results revealed the hydrodynamic size distribution of TPETPADCM-cRGD dots, which has an average size of ~32 nm with a low polydispersity of ~0.12 (Figure 4.3A). Transmission electron microscopy (TEM) image showed that TPETPADCM-cRGD dots are spherical nanoparticels with a mean size of ~30 nm. The UV-Vis and photoluminescence (PL) spectra of T-TTD NPs are shown in Figure 4.3B. They have two absorption peaks centred at 353 and 502 nm, respectively, with an emission maximum peaked at 669 nm. The fluorescence quantum yield was 10±1%, measured using Rhodamine 6G in methanol as the standard. The corresponding ROS generation capability of TPETPADCM-cRGD dots was then evaluated using 1,3-

diphenylisobenzofuran (DPBF) as the indicator, which could quickly react with ROS with reduced absorbance. As shown in Figure 4.3C, upon exposure to light irradiation, the solution shows quickly decreased absorbance at 418 nm (16.3% of its original after 1 min irradiation), which is indicative of efficient ROS generation by TPETPADCM-cRGD dots. Possessing the high brightness and ROS generation under illumination, the TPETPADCM-cRGD dots should be able to selectively recognize $\alpha_v\beta_3$ integrin overexpressed cancer cells and kill them.

4.3.3 Targeted Cellular Imaging

To test the targeting effect of TPETPADCM-cRGD dots, MDA-MB-231 cancer cells with overexpressed $\alpha_v\beta_3$ integrin on cellular membrane were chosen as integrin-positive cancer cells, while MCF-7 cancer cells and NIH 3T3 normal cells with low $\alpha_v\beta_3$ integrin expression were used as the negative controls. We incubated the TPETPADCM-cRGD dots with MDA-MB-231, MCF-7 and NIH 3T3 cells for 1 h. The confocal images are shown in Figures 4.4, where strong red fluorescence of TPETPADCM-cRGD dots in the cytoplasm and blue fluorescence of Hoechst from cell nucleus are simultaneously observed in MDA-MB-231 cells (Figure 4.4A). It is obvious that the red fluorescent signals in MCF-7 (Figure 4.4B) and NIH 3T3 (Figure 4.4C) cells are much weaker than that in MDA-MB-231 cells, indicating the TPETPADCM-cRGD dots are able to recognize and selectively image of MDA-MB-231 cells with $\alpha_v\beta_3$ integrin overexpression. Receptor blocking experiments were also carried out to investigate the uptake mechanism of TPETPADCM-cRGD dots. In these experiments, free cRGD was first incubated with MDA-MB-231 cells before TPETPADCM-cRGD dot were added. As shown in Figure 4.4D, the red fluorescent signal of T-TTD NPs is dramatically reduced when the integrin is initially blocked with

the excess cRGD. These results demonstrated that the TPETPADCM-cRGD dots were uptaken through $\alpha_v\beta_3$ integrin receptor-mediated endocytosis.

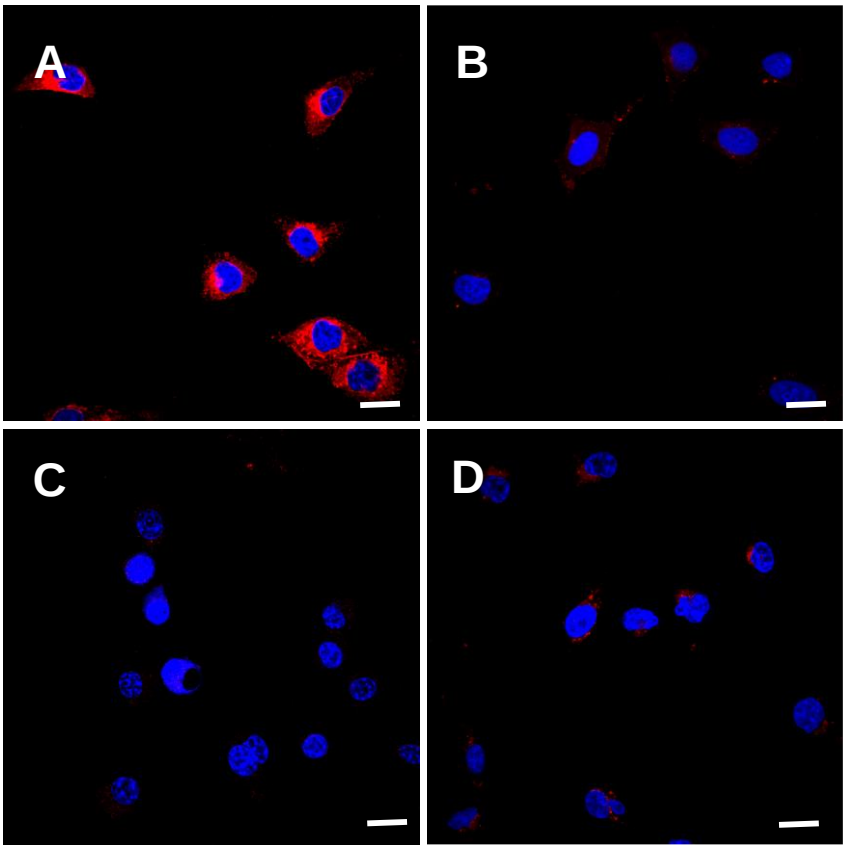

Figure 4.4. Confocal images of A) MDA-MB-231, B) MCF-7, C) NIH 3T3 cells, and D) free cRGD (50 μM) pre-treated MDA-MB-231 cells upon incubation with TPETPADCM-cRGD dots (1 μg/mL) for 1 h. The blue fluorescence from the nuclei of cells is dyed by Hoechst 33342, the red fluorescence is from TPETPADCM-cRGD dots. All the images share the same bar of 20 μm.

To evaluate whether the TPATPADCM-cRGD dots are able to generate ROS inside the cells, we used a cell permeable fluorescence dye dichlorofluorescein diacetate (DCF-DA). DCF-DA is able to be rapidly oxidized to highly fluorescent dichlorofluorescein (DCF) in the presence of ROS. As shown in Figure 4.5, strong green fluorescence of DCF was observed inside the targeted MBA-MD-231 cells, demonstrating efficient ROS generation from the TPETPADCM-cRGD dots. In contrast, negligible green fluorescence is observed when TPETPADCM-cRGD dots are

incubated with MCF-7 (Figure 2E) or NIH 3T3 (Figures 4.5B and C) cells, due to the poor cellular uptake of TPETPADCM-cRGD dots.

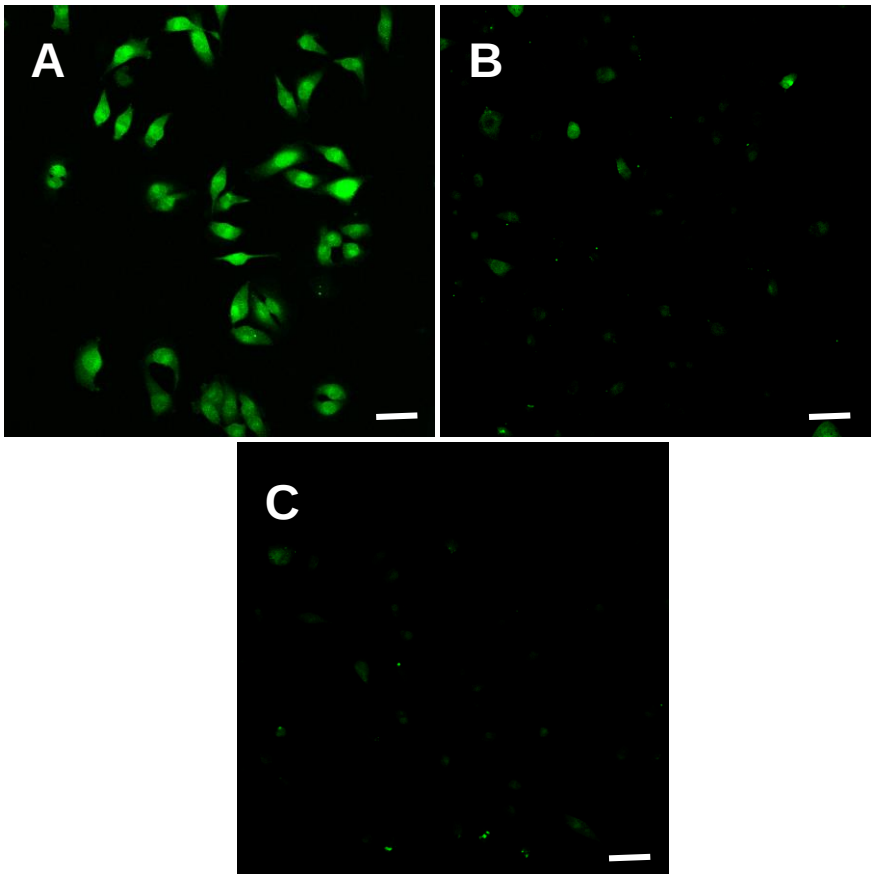

Figure 4.5. Detection of intracellular ROS production by dichlorofluorescein diacetate (DCF-DA) in A) MDA-MB-231, A) MCF-7 and C) NIH 3T3 cells after incubation with TPETPADCM-cRGD dots (10 μg/mL) followed by light irradiation. All the images share the same scale bar of 50 μm.

4.3.4 Photodynamic Therapy

The photodynamic therapy performance of TPETPADCM-cRGD was evaluated by standard methylthiazolyldiphenyltetrazolium bromide (MTT) assay. The viability of MDA-MB-231, MCF-7, NIH 3T3 cells after incubation with TPEPTADCM-cRGD dots at different concentrations was studied. As shown in Figure 4.6A, without the light irradiation, all the cells exhibit very high viability nearly 100%, indicative of non-toxicity and good biocompatibility of TPETPADCM-cRGD dots in dark. While, exposure these TPETPADCM-cRGD dots treated cells to light irradiation,

the TPETPADCM-cRGD dots only showed obvious cytotoxicity to MDA-MB-231 cells. The toxicity increased with the TPETPADCM-cRGD dot concentration, with a half-maximal inhibitory concentration (IC_{50}) of 11 μg mL^{-1} under our experimental conditions.

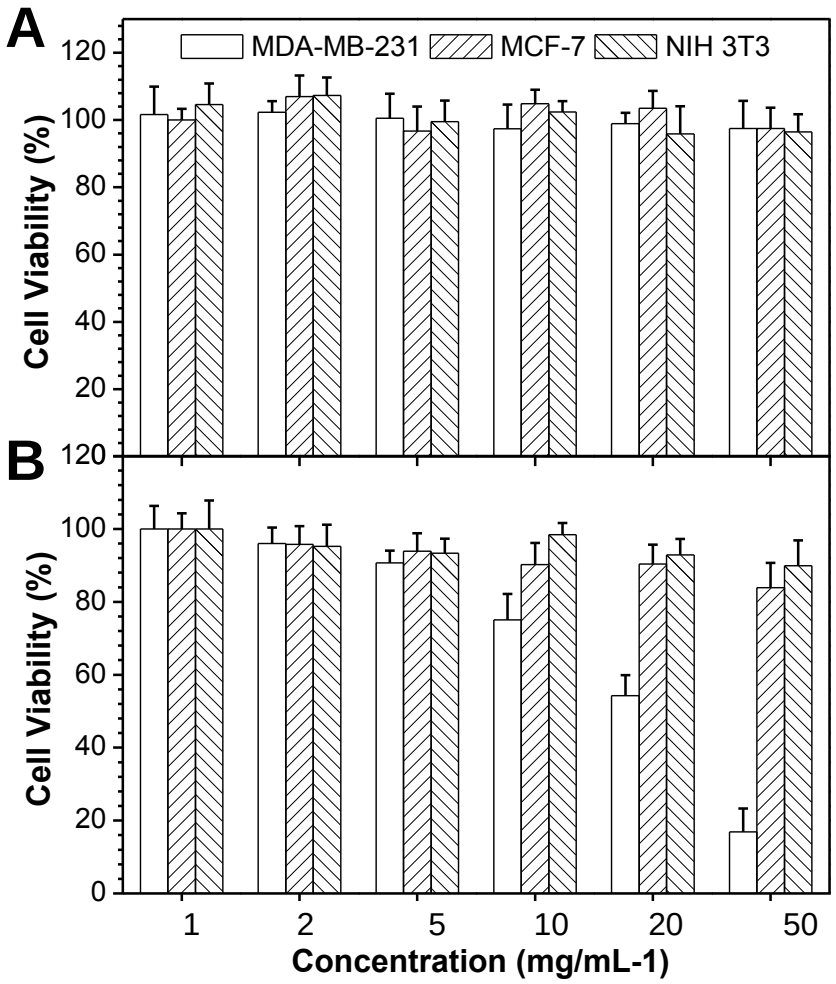

Figure 4.6. Inhibition of MDA-MB-231, MCF-7 and NIH 3T3 cells growth in the presence of different concentrations of TPETPADCM-cRGD dots A) without or B) with light irradiation (0.25 W cm^{-1}, 2 min) followed by further incubation of the cells for 24 h. Data represent mean values ± standard deviation, n = 3.

Apoptosis is the process of programmed cell death, and photodynamic treated can induce this cell apoptosis process. We used fluorescein isothiocyanate (FITC)-tagged Annexin V, one of the most commonly used fluorescent probes to distinguish viable cells from apoptotic ones, to visualize the apoptosis cells in our experiment. Annexin V can bind to the membrane of apoptotic cells which express

phosphatidylserine. As shown in Figure 4.7A, after incubation of TPETPADCM-cRGD dots with light irradiation in MDA-MB-231 cells, green fluorescence attributed to FITC is clearly observed from the cell membrane, indicating that the cells possibly underwent apoptosis process. No FITC signal is detectable in MCF-7 (Figure 4.7B) and NIH 3T3 (Figure 4.7C) cells, which agrees with the results shown in Figures 4.4-6. The overall results indicate that the cRGD moiety is able to guide the TPETPADCM-cRGD dots to $\alpha_v\beta_3$ integrin overexpressed tumor cells, resulting in selective cancer cell killing due to the ROS generation.

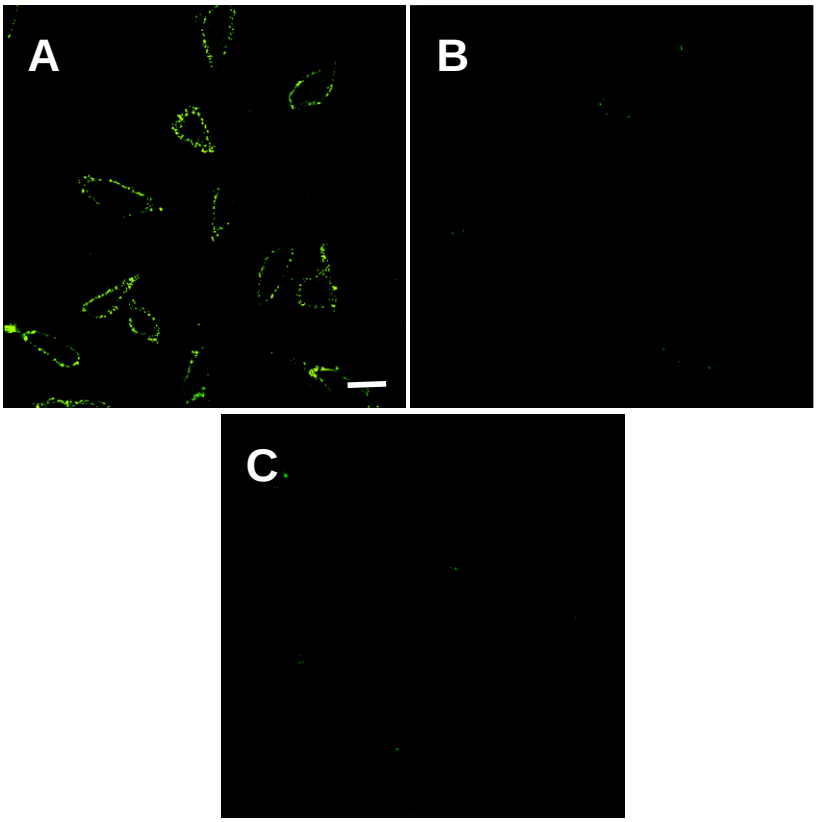

Figure 4.7. Cell apoptosis imaging using FITC-tagged Annexin V in MDA-MB-231 (A), MCF-7 (B) and NIH 3T3 (C) cells incubated with TPETPADCM-cRGD dots after light irradiation. All images share the same scale bar of 20 μm.

4.4 Conclusion

In summary, in chapter, we demonstrated that AIEgen can also act as PSs, moreover, they are able to show efficient ROS generation in aggregated state. We fabricated AIE dots based on a red-emissive fluorogen with AIE characteristics as the PS for imaging-guided PDT. To selectively target a specific type of cancer cells, cRGD peptide was conjugated to the NP surface. Due to the suppressed nonspecific cellular uptake, the fabricated TPETPADCM-CRGD dots showed targeted cellular imaging towards $\alpha_v\beta_3$ integrin overexpressed cancer cells with high sensitivity and selectivity. Cell viability studies showed that TPETPADCM-cRGD dots could selectively and efficiently kill the targeted cancer cells under a beam of light irradiation. This PDT platform based on AIEgens is simple to design and synthesis, which offers new opportunities for imaging-guided PDT.

CHAPTER 5

CELLULAR AND MITOCHONDRIA DUAL TARGETED ORGANIC DOTS WITH AGGREGATION-INDUCED EMISSION CHARACTERISTICS FOR IMAGE-GUIDED PHOTODYNAMIC THERAPY

5.1 Introduction

Mitochondria are the vital sub-cellular organelles to eukaryotic cells and powerhouse of cell activity.[158, 159] Mitochondria medicine has emerged as a new field of biomedical and pharmacological research.[160] To achieve the mitochondria targeting with enhanced therapy effects, the therapeutic reagents need to internalize into targeted cells and accumulate at mitochondria sites.[161-163] This is much more crucial when it comes to photodynamic therapy (PDT) as mitochondria are the main targeted of singlet oxygen,[164-166] and the singlet oxygen is short in lifetime (< 0.04 μs) as well as radius of action (< 0.02 μm).[167-170] Direct modification of drugs or photosensitizers (PSs) with mitochondria targeting ligands has been prevalent in last decades to direct drug cargoes to mitochondria.[167, 171-176] However, these approaches required tedious synthetic processes with limitations that the post-modified drugs or molecules may not be able to maintain their therapeutic effects.[177]

Recently, nanotechnology or nanocarrier systems have been considered as a simple and non-chemical approach to deliver drug molecules to specific targeted cells or subcellular organelles of interest with enhanced stability and pharmacokinetics.[177-182] Up to now, various nanocarriers including liposome micelles or solid nanoparticles (NPs) have been reported to be able to deliver the loaded drugs to mitochondria.[183-190] but none of them possesses the selectivity towards different cell lines. Moreover, the aggregation-caused quenching (ACQ) effect of traditional PSs often leads to quenched fluorescence as well as reduced ROS generation when they naturally aggregated or accumulated in limited area,[191-193] which largely compromised the efficiencies of PDT. Moreover, the existence of ACQ effect also makes it difficult to develop NPs with bright fluorescence and efficient ROS production for image-guided PDT based on traditional PSs. We and other have reported the novel fluorogens with aggregation-

induced emission (AIEgen) characteristics,[39, 42, 110-114] which has attracted great research interests in biological and biomedical applications. Very recently, we and others also found that several AIEgens show efficient ROS production in aggregate state.[52, 53, 88, 194] These unique properties are ideal for mitochondria targeted PDT since encapsulation of AIEgens by mitochondria targeted nanocarriers will not compromise their fluorescence and ROS generation.

In this chapter, we developed a facile strategy of fabrication of AIE dots with bright red fluorescence and high ROS generation for cellular and mitochondrial dual-targeted PDT, which served as the extension of previous chapter. We synthesized a new AIEgen, **DPBA-TPE**, which showed strong red fluorescence and efficient ROS generation in aggregates under light illumination. The corresponding AIE dots were then fabricated by a modified nano-precipitation method using DSPE-PEG as encapsulation matrix. Bearing folic acid and triphenylphosphine (TPP) targeting ligands at the surface, the yielded **FA-AIE-TPP** dots are able to selectively internalize into folate-receptor (FR) positive cancer cells over other cells and subsequently accumulate in mitochondria. The dual targeted **FA-AIE-TPP** dots showed enhanced PDT effects as compared to sole cellular targeted or mitochondria targeted AIE dots. Our NP formulation thus represents a simple and general strategy for cellular and subcellular dual targeted delivery.

5.2 Experimental

5.2.1 Materials

1,4-Bis(bromomethyl)-2,5-dimethoxybenzene (**2**), 2,5-bimethoxybenzene-1,4-dicarboxaldehyde (**3**), and *N*-(4-(1,2,2-triphenylvinyl)phenyl)benzenamine (**10**), were prepared according to the literature. 1,2-distearoyl-sn-glycero-3-phosphoethanolamine-N-[amino(polyethylene glycol)-2000]) (DPSE-PEG-NH_2) and (1,2-distearoyl-sn-

glycero-3-phosphoethanolamine-N-[folate(polyethylene glycol)-2000]) (DSPE-PEG-FA) were purchased from Avanti Polar Lipids, Inc. All the other chemicals and reagents were purchased from Sigma-Aldrich and used as received without further purification.

5.2.2 Characterization

^{1}H spectrum was measured on a Bruker AV 300 or 400 spectrometer in CD_2Cl_2 using tetramethylsilane (TMS; $\delta = 0$) as internal reference. High resolution mass spectra (HRMS) were recorded on a GCT premier CAB048 mass spectrometer operating in MALDI-TOF mode. The UV-vis and PL spectra were measured on UV-1700 (Shimadzu, Japan) and LS-55 (Perkin Elmer, USA) spectrometer, respectively. Laser light scattering with a particle size analyzer (90 Plus, Brookhaven Instruments Co. USA) was used to determine the hydrodynamic diameters of AIE dots. Zeta-potential of AIE dots was determined by Zetasizer (Malvern, UK). High-resolution transmission electron microscope (HR-TEM, JEM-2010F, JEOL, Japan) was used to study the morphology and size of AIE dots.

5.2.3 Preparation of DPBA-TPE

The **DPBA-TPE** molecular was synthesized by Qin Wei (HKUST). A dry ethanol solution (30mL) of sodium hydroxide (40 mg) was added to a mixture of 4-bromophenylacetonitrile (873 mg, 4.5 mmol) and 2,5-bimethoxybenzene-1,4-dicarboxaldehyde (388 mg, 2 mmol) under a nitrogen atmosphere. The reaction mixture was stirred for 12 h at room temperature, and the precipitate was filtered out and washed with water and DCM. An orange powder (**5**) was obtained in 81.9% yield (904 mg). Compound **5** (200 mg, 0.364 mmol) was reacted with **10** (381 mg, 0.9 mmol) in the presence of $Pd(OAc)_2$ (11.2 mg, 0.05 mmol), Cs_2CO_3 (487 mg, 1.5 mmol), P(*t*-Bu)$_3$ (30.3 mg, 0.15 mmol) and toluene (40 mL) at 110 ℃ for 24 h under a nitrogen

atmosphere. Water (30 mL) and chloroform (300 mL) were then added after cooling to room temperature. The obtained organic layer was washed with brine, dried by anhydrous $MgSO_4$ and further dried under reduced pressure. Column chromatography on silica gel using hexane/DCM as eluent was they applied to purify the crude product. The afforded **DPBA-TPE** as a red solid in 68% yield (305 mg). ^{1}H NMR (400 MHz, CD_2Cl_2), δ (TMS, ppm): 7.90 (s, 2H), 7.88 (s, 2H), 7.55 (d, *J* = 8.8 Hz, 4H), 7.30 (t, *J* = 8.0 Hz, 4H), 7.18-7.02 (m, 40H), 6.94 (d, *J* = 8.4 Hz, 4H), 6.85 (d, *J* = 8.4 Hz, 4H), 3.94 (s, 6H). ^{13}C NMR (75 MHz, $CDCl_3$), δ (TMS, ppm): 152.32, 149.09, 147.25, 145.65, 144.32, 144.14, 143.92, 141.36, 140.98, 139.70, 133.78, 132.66, 131.67, 131.64, 131.61, 129.79, 128.19, 128.05, 128.02, 127.25, 126.86, 126.83, 126.76, 125.94, 125.47, 124.34, 124.22, 122.76, 118.79, 111.89, 110.58, 56.74. HRMS (MALDI-TOF, m/z): [M^+] calcd for $C_{90}H_{66}N_4O_2$, 1234. 5186; found, 1234.5192. Anal. calcd for $C_{90}H_{66}N_4O_2$: C, 87.49; H, 5.38; N, 4.53; O, 2.59. found: C, 87.61; H, 5.33; N, 4.52.

5.2.4 Preparation of DPBA-TPE Nanoaggregates

DPBA-TPE was fully dissolved in THF to prepare the stock (100 μM). Appropriate amounts of the THF stock solution were then mixed with different volumes of MilliQ water under vigorous stirring to reach the final concentration of 10 μM with different water fraction (0–90 vol%). The PL spectra of these mixtures were then measured by LS-55 spectrometer.

5.2.5 ROS Generation Measurement

The ROS generation of **DPBA-TPE** aggregates or AIE dots under light irradiation was measured using dichlorofluorescin (DCFH) as the indicator. The PL spectra of the mixture of **DPBA-TPE** (10 μM) and DCFH (2 μM) were measured

before and after exposure to white light irradiation (250 $mWcm^{-2}$) upon excitation at 460 nm. The increase of fluorescence intensity at 530 nm is the indication of ROS generation in solution. The same experimental procedures were applied to AIE dots.

5.2.6 Preparation of AIE Dots

To synthesize **AIE-FA** dots, a THF solution (1 mL) containing **DPBA-TPE** (0.5 mg) and DSPE-PEG-FA (0.5 mg) and DSPE-PEG (0.5 mg) was poured into water (10 mL) under sonication using a microtip probe sonicator at 12 W output (XL2000, Misonix Incorporated, NY). The mixture was further placed in dark in fume hood for THF evaporation at 600 rpm overnight, and concentrated by centrifuge. To synthesize **AIE-TPP** dots, DSPE-PEG-NH_2 (0.5mg) was used to replace DSPE-PEG-FA (0.5 mg) during the nanoparticle formation. The resultant AIE dots suspension with amino group at surface was reacted with excess triphenylphosphine (TPP). **AIE-TPP** dots were then dialysis against water with 6-8 kDa membrane to remove excess TPP. To synthesize **FA-AIE-TPP** dots, DSPE-PEG-FA (0.5 mg) and DSPE-PEG-NH_2 (0.5 mg) were used as the matrix during dots formation. The AIE dots suspension was then reacted with TPP. **FA-AIE-TPP** dots were then dialysis against water using 6-8 kDa membrane to remove excess TPP.

5.2.7 Confocal Imaging

NIH-3T3 normal cells and MCF-7 cancer cells were cultured in 8-well chamber (LAB-TEK, Chambered Coverglass System) at 37 ℃. After 80% confluence, the cells were incubated for 4 h with these AIE dots (20 μg/mL based on **DPBA-TPE** mass concentration) suspended in cell culture medium, and then washed twice with PBS. To label mitochondria, the cells were further incubated with MitoTracker Green (Invitrogen, 200 nM) for 20 min. After washing, the cells were immediately imaged by confocal laser scanning microscope (CLSM). The red fluorescence from AIE-dots was

acquired above 650 nm upon excitation at 534 nm. The green fluorescence from MitoTracker Green was obtained between 505 to 560 nm upon excitation at 488 nm.

5.2.8 Measurement of Mitochondrial Membrane Potential

JC-1 dye (Invitrogen) was used to measure mitochondrial membrane potential (MMP) changes during PDT treatment. After 4h incubation of MCF-7 cells with these AIE dots (20 μg/mL based on **DPBA-TPE** mass concentration) suspended in cell culture medium. The cells were washed and exposed to light irradiation (100 $mWcm^{-2}$) for 0, 5, and 10 min. MCF-7 cells were incubated with JC-1 dyes (2 μg/mL) for 20 min. After washing, the cells were immediately imaged by CLSM. Upon excitation at 488 nm, the green signal was collected between 505 and 525 nm, and the red signal was collected above 590 nm.

5.2.9 Flow Cytometry

NIH-3T3 normal cells and MCF-7 cancer cells were cultured in 6-well plate at 37 ℃. After 80% confluence, the cells were incubated with these AIE dots (20 μg/mL based on **DPBA-TPE** mass concentration) suspended in cell culture medium for 4 h. The cells were then harvested by trypsin, and resuspended in 1×PBS. Cyan-LX (DakoCytomation) was then used to access the fluorescence intensities of cells, where 10,000 events were counted for the histogram analysis.

5.2.10 Cell Migration Assay

NIH-3T3 and MCF-7 cells were cultured into 6-well plates and grown for 24 h. Cell scratch spatula were applied to make a scratch in the cell monolayer. After rinsing the cells with PBS, the photographs of the scratches were taken using a microscope with a 10× objection (Nikon-Ti-U). The cells were then treated with AIE dots (20 μg/mL based on **DPBA-TPE** mass concentration) for 4 h and followed by light

irradiation (100 $mWcm^{-2}$, 10 min), the cells were further cultured for 72 h, after which the pictures were taken again. The migration ratio is determined by the number of cells migrated to wound area after PDT treatment to that of control cells without any treatment and light irradiation after 72 h.

5.2.11 Cytotoxicity Studies

The viability of NIH-3T3 and MCF-7 cells was evaluated using methylthiazolyldiphenyltetrazolium bromide (MTT) assays. Both cells were seeded in 96-well plates (Costar, IL, USA) at an intensity of 4×10^4 cells/mL, respectively. After 24 h incubation, AIE dots in DMEM suspensions at various concentrations were then added into each well. After 4 h incubation, the AIE dot suspensions were replaced by fresh cell culture medium. The selected wells were exposed to light irradiation (100 $mWcm^{-2}$, 10 min), and further cultured for 24 h. In the parallel experiment, both cell lines were treated with AIE dots for 24 h in dark. The cells were then incubated with MTT solution (0.5 mg/mL, 100 μL/well) for 3 h. After remove of MTT, filtered DMSO was then added (100 μL/well) and the plate was gently shaken for 10 min at room temperature to dissolve all the precipitates formed. Microplate reader (Genios Tecan) was then used to access the absorbance of MTT at 570 nm. Cell viability was determined by the ratio of the absorbance of the cells incubated with AIE dots to that of the cells incubated with culture medium only. The same experiment procedures were repeated by fixing the AIE dot concentration with varied light power or exposure time.

5.3 Results and Discussion

5.3.1 Synthesis and Characterization of DPBA-TPE

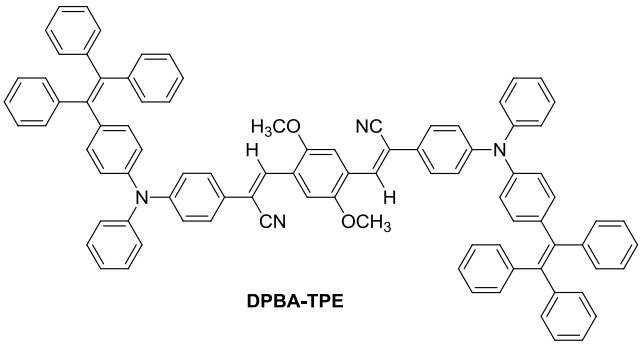

DPBA-TPE

Scheme 5.1. Chemical structure of **DPBA-TPE**.

To demonstrate the potential of AIE dots for cellular and mitochondria dual targeted image-guided PDT, a new AIEgen, **DPBA-TPE** (Scheme 5.1) with ROS production ability was and designed and synthesized by our collaborator in Hong Kong University of Science and Technology (HKUST). The structure of **DPBA-TPE** (Scheme 5.1) is comprised of the dimethoxybenzene and arylamines as the electron donor (**D**), cyano groups as the acceptor (**A**), as well as TPE groups as the iconic AIE unit. The introduction of **D-A** system to TPE groups is expected to generate a new AIEgen with increased electronic conjugation, and hence longer absorption and emission wavelengths. **DPBA-TPE** in THF showed an absorption spectrum peaked at 480 nm. The AIE properties of **DPBA-TPE** were studied by measuring its photoluminescence (PL) spectrum changes in water/THF mixtures with different water fractions (f_w) (Figure 5.1A). **DPBA-TPE** in THF shows weak orange-red fluorescence where the emission peaks at 619 nm. With the increase of f_w ($\leq$ 40%), the emission of **DPBA-TPE** is decreased and bathochromically shifted to 624 nm, due to solvent polarity increase and the transformation to the twisted intramolecular charge transfer (TICT) state. Upon further increasing f_w, the emission of **DPBA-TPE** is invigorated from f_w of ~50% and is further intensified. Collectively, these data indicate that **DPBA-**

TPE possesses both AIE and TICT characteristics, while AIE plays a dominant role in determining their optical properties in aggregated states.

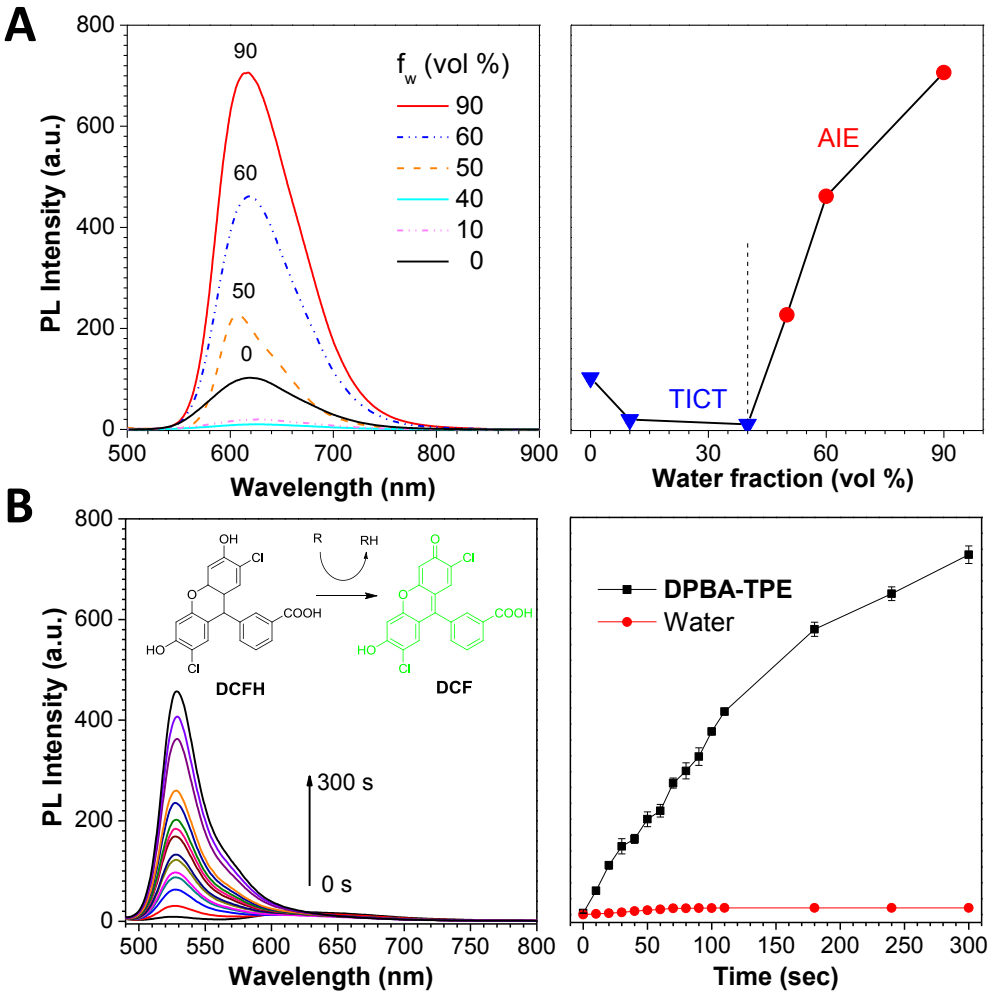

Figure 5.1. A) PL spectra of **DPBA-TPE** (10 μM) in THF/water mixtures with different water fractions. B) PL spectra of **DPBA-TPE** (10 μM) and DCFH (2 μM) mixture in water with different white light irradiation time (250 mW cm^{-2}).

To study whether **DPBA-TPE** is able to generate ROS in aggregated state, dichlorofluorescin (DCFH) was used as the ROS indicator, which initially shows no fluorescence in aqueous solution but emits bright green fluorescence upon reaction with singlet oxygen. As shown in Figure 5.1B, the mixed aqueous solution of **DPBA-TPE** (10 μM) and DCFH (2 μM) showed quickly increased fluorescence centered at 530 nm upon exposure to white light irradiation (250 mW cm^{-2}) within minutes, while DCFH itself under light irradiation remain weakly fluorescent, indicating that the **DPBA-TPE**

aggregates are able to efficiently generate singlet oxygen species. Together with the bright red fluorescence in the aggregated state, it is highly predictable that the encapsulation of **DPBA-TPE** into organic dots will not compromise its imaging quality and PDT effect.

5.3.2 Fabrication and Characterization of AIE dots

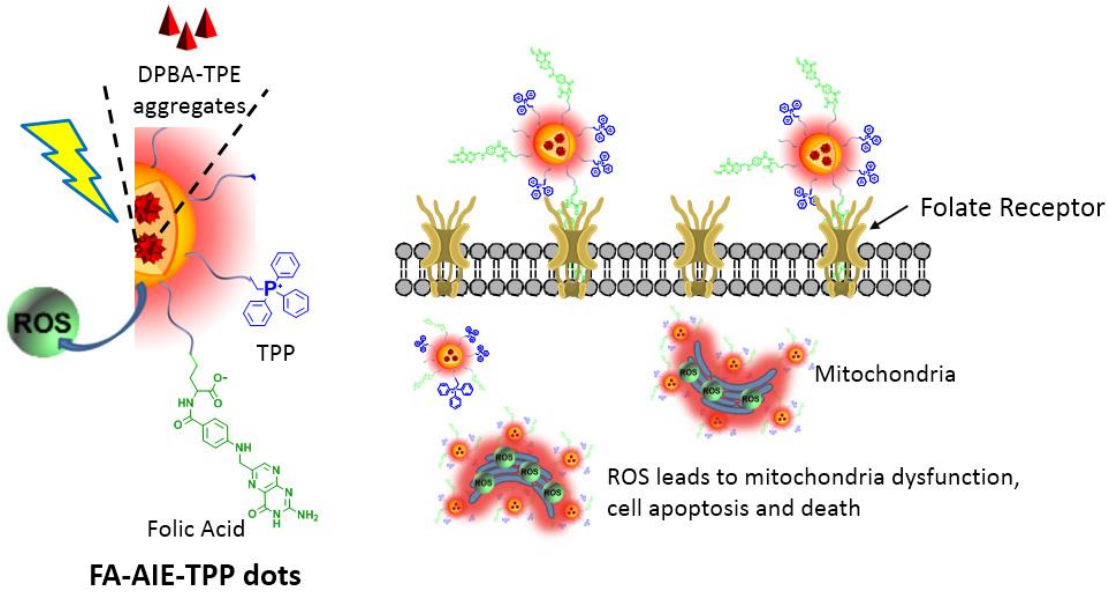

Scheme 5.2. Schematic illustration of **FA-AIE-TPP** dots for specific targeting of FR-positive MCF-7 breast cancer cell mitochondria for image-guided PDT.

To fabricate the dual targeting AIE dots, a modified nano-precipitation method as described in previous chapters was used (Scheme 5.2). Biocompatible block copolymers of lipid-PEG with different terminal groups, (1,2-distearoyl-sn-glycero-3-phosphoethanolamine-N-[amino(polyethylene glycol)-2000]) (DPSE-PEG-NH_2) and (1,2-distearoyl-sn-glycero-3-phosphoethanolamine-N-[folate(polyethylene glycol)-2000]) (DSPE-PEG-FA) were chosen as the encapsulation matrix. To bring the resultant AIE dots to mitochondria, cationic TPP, which is able to accumulate in mitochondria in response to high mitochondrial membrane potential (MMP),[195, 196] was then reacted with AIE dot suspension to yield **FA-AIE-TPP** dots. After the reaction, dialysis of the **FA-AIE-TPP** dots suspension against water using 6 to 8 kDa cutoff

membrane was applied to remove excess TPP. Similar procedures were applied to fabricate folic acid mono-functionalized AIE dots (**AIE-FA)** and TPP mono-functionalized AIE dots (**AIE-TPP)**. The formed **FA-AIE-TPP** dots are expected to specifically internalize into folate receptor (FR) positive cancer cells, and subsequently accumulate in mitochondria for mitochondria imaging and enhanced PDT effects (Scheme 5.2).

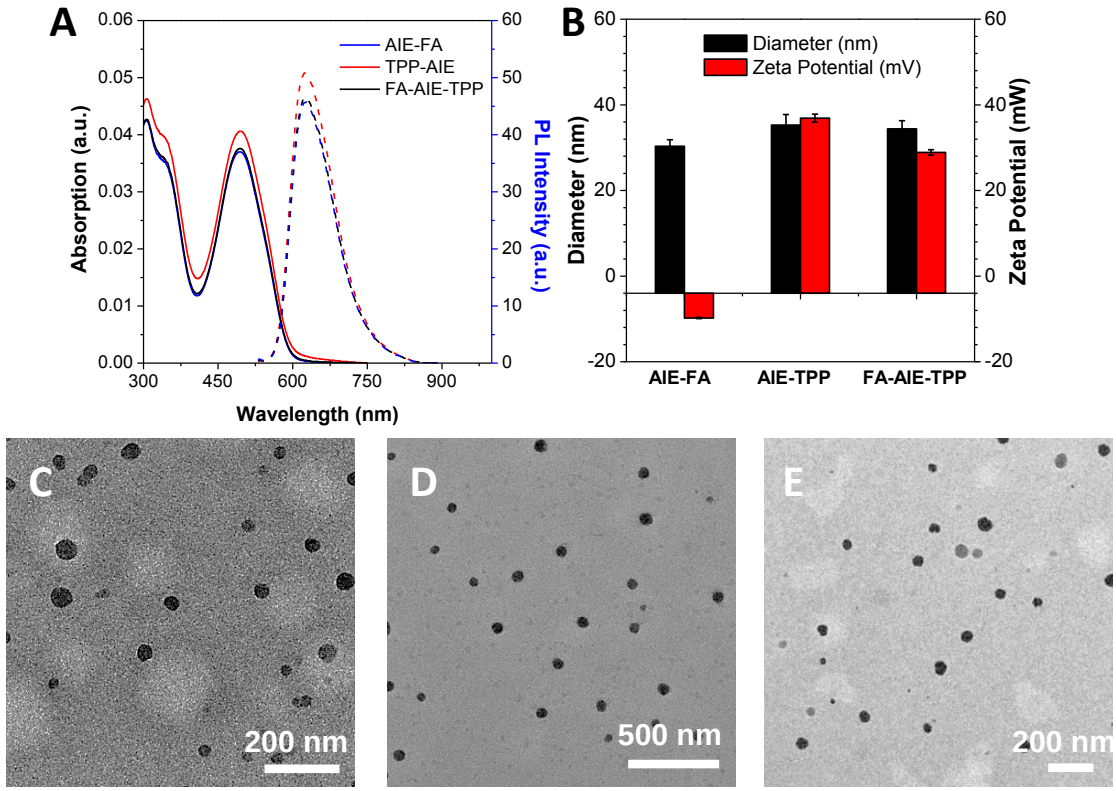

Figure 5.2. A) Absorption and PL spectra, and B) hydrodynamic diameters and surface zeta potentials of three AIE dots in water. TEM image of C) **AIE-FA**, D) **AIE-TPP**, and E) **FA-AIE-TPP** dots.

The absorption and PL spectra of **FA-AIE-TPP** dots in aqueous suspension are shown in Figure 5.2. The **FA-AIE-TPP** dot suspension showed two absorption peaks centered at 305 and 497 nm, respectively. The PL spectrum is centered at 624 nm with a fluorescence quantum yield of 14% using 4-(dicyanomethylene)-2-methyl-6-(p-dimethylaminostyryl)-4H-pyran (DCM) in methanol as reference (43%). It should be noted that surface modification does not affect the optical properties of the AIE dots as

both **AIE-FA** and **AIE-TPP** dots showed similar absorption and PL spectra (Figure 5.2A), which should be benefited from the excellent encapsulation ability of DSPE-PEG. The hydrodynamic diameters of the three AIE dots were evaluated using laser light scattering (LLS). **AIE-FA, AIE-TPP,** and **FA-AIE-TPP** dots exhibit similar sizes of around ~30±1.2, ~35±1.7, ~34±1.5 nm with narrow size distribution, respectively (Figure 5.2B). The surface zeta potentials of the three dots are −9.8, 36.9, 28.9 mV for **AIE-FA**, **AIE-TPP** and **FA-AIE-TPP** dots, respectively. The increase of surface charge of **AIE-TPP** and **FA-AIE-TPP** dots should be due to the conjugation of TPP at dots surface, which also slightly increases the AIE dot sizes. High resolution transmission electron microscope (HR-TEM) was further applied to study the morphology and size distribution of these AIE dots. The **FA-AIE-TPP** dots are spherical in shape with a mean diameter of 31 nm, and **AIE-FA** and **AIE-TPP** dots exhibit similar spherical shapes with sizes around 28 nm and 32 nm (Figures 5.2C-E). In addition, no precipitation was observed after the AIE dots have been stored for several months, indicating the excellent colloidal stability.

The PDT effect of the AIE dots is further studied by measuring the reactive oxygen species (ROS) generation efficiency under light irradiation using DCFH as an indicator. As shown in Figure 5.3, the **FA-AIE-TPP** dot suspension is able to generate ROS very quickly and efficiently under white light irradiation, which is evidenced by the rapid increase of DCFH fluorescence intensity at 530 nm. Moreover, increasing the exposure time, AIE dot concentration, or light power will also increase the ROS generation (Figure 5.3), indicating that ROS production of AIE dots is time-, concentration- and power-dependent. Such an efficient ROS generation capability makes the AIE dots a good candidate for image-guided PDT.

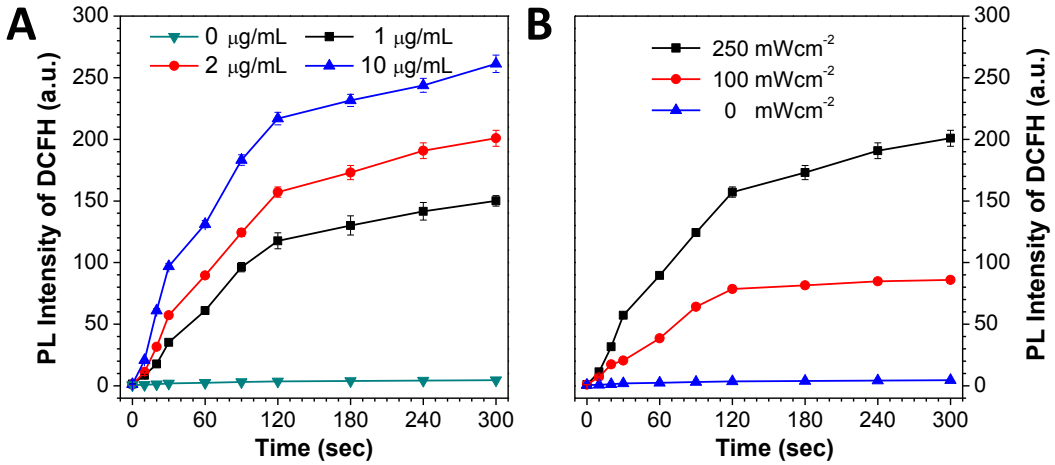

Figure 5.3. ROS generation of **FA-AIE-TPP** dots in aqueous solution at A) varied dot concentrations with a fixed light power of 250 $mWcm^{-2}$, and B) varied light powers with fixed dot concentration of 2 μg/mL upon irradiation for 300 s, using DCFH (2 μM) as ROS indicator.

5.3.3 Cellular and Mitochondria Dual Targeted Imaging

The cellular targeting of the three AIE dots were investigated by flow cytometry and fluorescence imaging. FR-positive MCF-7 breast cancer cells were chosen as the target, with FR-negative NIH-3T3 fibroblast cells as the control. After incubating both cell lines for 4 h with the three AIE dots at 20 μg/mL based on **DPBA-TPE** mass concentration, flow cytometry was further applied to study the cellular uptake of AIE dots in MCF-7 and NIH-3T3 cells. All the three AIE dots treated NIH-3T3 cells only show very small increase in average fluorescence intensity, indicating the low cellular uptake of all the AIE dots into NIH-3T3 cells due to lack of cellular targeting ligands and the suppressed non-specific internalization by PEG (Figure 5.4A). On the other hand, **FA-AIE-TPP** and **AIE-FA** dots treated MCF-7 cells show similar average fluorescence intensities, which are much higher than those of blank or **AIE-TPP** dots treated MCF-7 cells (Figure 5.4B).

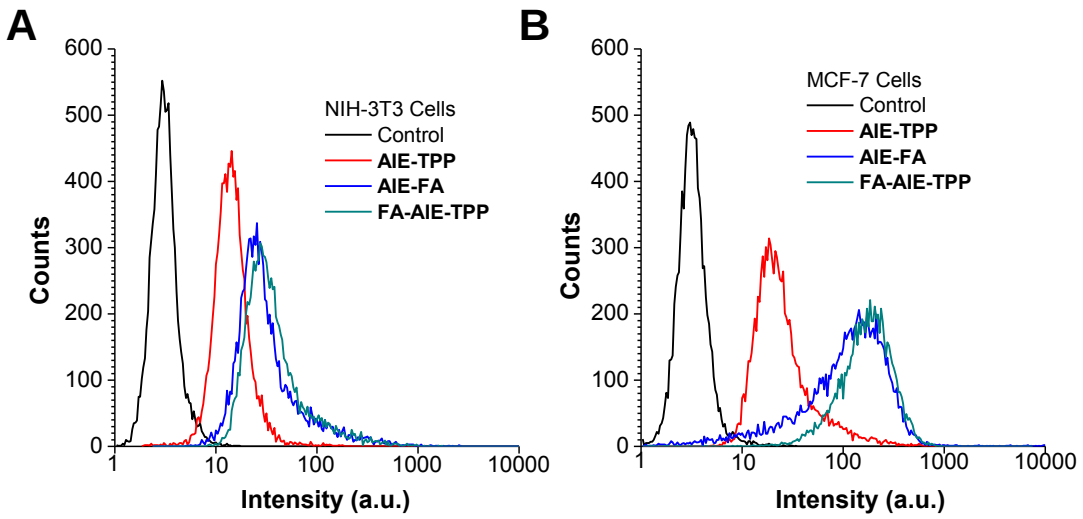

Figure 5.4. Flow cytometry histograms of A) NIH-3T3 cells and B) MCF-7 cells after incubation with AIE dots (20 μg/mL) for 4 h.

The confocal images were then used to study the cellular targeting performance. Figure 5.5 shows the corresponding fluorescence images of these AIE dots treated either MCF-7 or NIH-3T3 cells. For **FA-AIE-TPP** or **AIE-FA** dots incubated cells, much stronger red fluorescence can be observed for MCF-7 cells than NIH-3T3 cells, revealing the targeting capability of folate decorated AIE dots towards FR-positive cells. While, **AIE-TPP** dots show very weak fluorescence inside both cell lines. The confocal images are in consistent with flow cytometry results, indicating that folic acid decoration promotes the cellular uptake of AIE dots to FR-positive cells. As TPP is able to drive **FA-AIE-TPP** dots to mitochondria, the similar cellular uptake between **AIE-FA** dots and **FA-AIE-TPP** dots should provide insights into the important roles of the PS localization inside cells for different PDT performance.

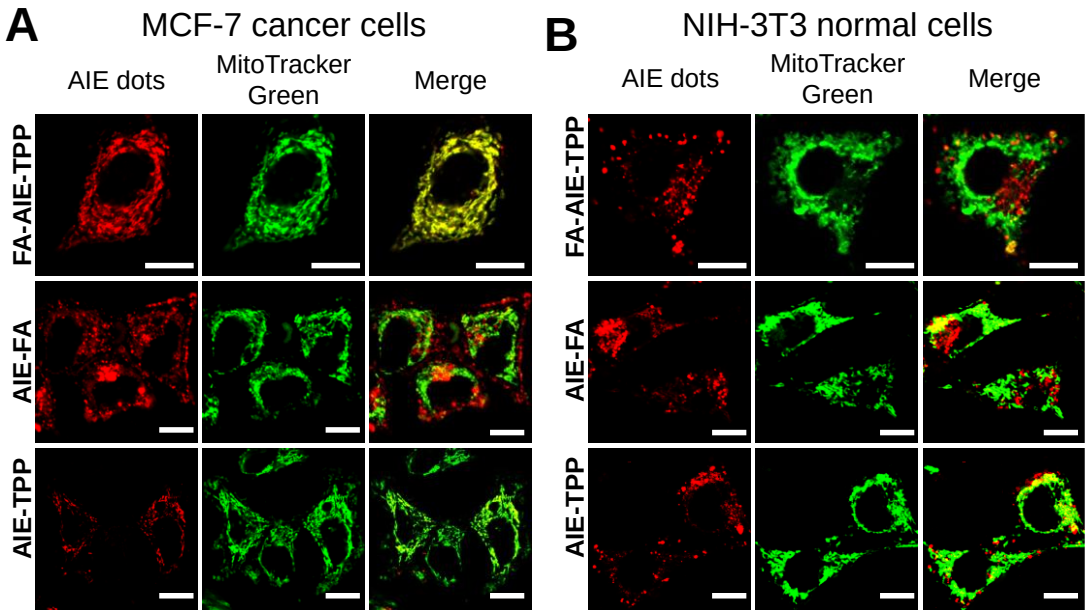

Figure 5.5. CLSM images of A) MCF-7 cancer cells and B) NIH-3T3 normal cells after incubation with AIE dots (20 μg/mL) and MitoTracker Green (200 nM). AIE dots: E_x: 543 nm, E_m: > 650 nm; MitoTracker Green: E_x = 488, E_m = 505 – 525 nm. The scale bar size is 10 μm for all images.

To test whether these AIE dots are able to accumulate at mitochondrial sites, commercially available mitochondrial tracker MitoTracker Green (Invitrogen) was used as the co-stain. The red fluorescence from **FA-AIE-TPP** dots clearly shows a characteristic mitochondrial network inside MCF-7 cells (Figure 5.5A), which is in consistent with green fluorescence emitted from MitoTracker Green. Without TPP decoration, **AIE-FA** dots are randomly distributed inside MCF-7 cancer cells, indicating that the existence of TPP drives the accumulation of AIE dots to mitochondria. Due to the poor cellular uptake of **AIE-TPP** dots as previously described, poor visualization of mitochondrial pattern in MCF-7 cells is observed. On the other hand, besides very weak red fluorescence, its poor overlap with the green fluorescence from MitoTracker green is observed for NIH-3T3 cells, indicating the poor cellular uptake and mitochondria localization of all three AIE dots in FR-negative cells (Figure 5.5B). The Pearson's correlation coefficients are also used to quantify the co-localization between AIE dots and MitoTracker Green, which are 0.97, 0.49, 0.63 for

MCF-7 cells, and 0.29, 0.40, 0.31 for NIH-3T3 cells, for **FA-AIE-TPP**, **AIE-FA**, and **AIE-TPP** dots, respectively. The higher Pearson's coefficient of **AIE-TPP** dots in MCF-7 than NIH-3T3 cells should be ascribed to the higher MMP of cancer cells over normal cells, which promoted mitochondria accumulation of **AIE-TPP** dots in MCF-7 cells. The highest Pearson's coefficient for **FA-AIE-TPP** dots towards MCF-7 cell mitochondria clearly demonstrates that modifying the mitochondria targeted nanocarriers with secondary cellular targeting ligands is able to enhance their cellular uptake towards targeted cells with subsequent mitochondria accumulation.

5.3.4 Photodynamic Therapy of AIE Dots

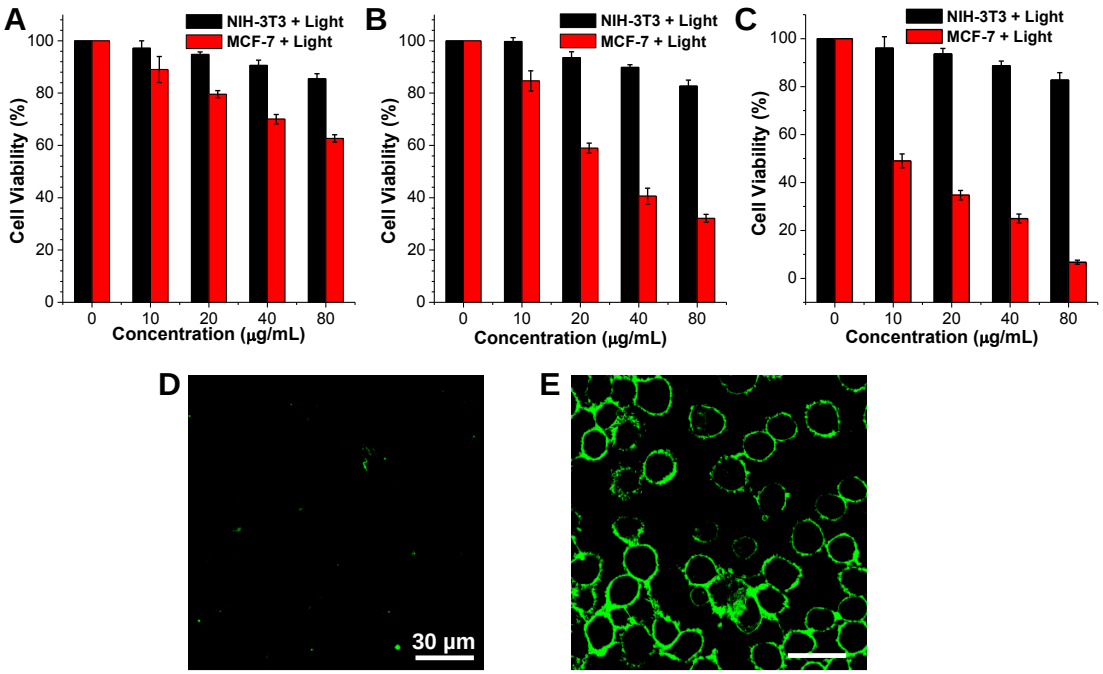

Figure 5.6. Viabilities of MCF-7 cancer cells and NIH-3T3 normal cells after incubation with A) **AIE-TPP**, B) **AIE-FA**, C) **FA-AIE-TPP** dots at varied concentrations, followed by white light irradiation (250 $mWcm^{-2}$). D) and E) Annexin V labeled MCF-7 cells after incubation with **FA-AIE-TPP** dots (20 μg/mL) without (D) or with (E) light irradiations (250 $mWcm^{-2}$). D) and E) share the same scale bar.

The PDT effects of the three **AIE** dots on viabilities of NIH-3T3 and MCF-7 cells were then investigated by MTT assays. Upon incubation with the three AIE dots in dark for 24 h, both NIH-3T3 and MCF-7 cells exhibit high cell viabilities of over 90%

even at a high **DPBA-TPE** concentration of 80 μg/mL, indicating the low cytotoxicity of AIE dots without light irradiation. In the parallel experiments, incubating both cell lines with AIE dots for 4 h and followed by light irradiation (100 $mWcm^{-2}$) for 10 min leads to large differences in cell viabilities (Figures 5.6 A-C). All three AIE dots exhibit very low photo-toxicity towards NIH-3T3 cells, which should be due to the poor cellular uptake. As for MCF-7 cells, **FA-AIE-TPP** dots show the most efficient killing efficiency under light irradiation with a cell viability of less than 10% at the **DPBA-TPE** concentration of 80 μg/mL. While under the same condition, **AIE-TPP** and **AIE-FA** dots treated MCF-7 cells show cell viabilities of ~60% and ~32%, respectively. The half maximal inhibitory concentration (IC_{50}) was further applied to quantify the anticancer efficiency of the three dots under light irradiation. The IC_{50} values are >80, ~32, and ~10 μg/mL for **AIE-TPP**, **AIE-FA**, and **FA-AIE-TPP** dots, respectively. As almost the same amount of **AIE-FA** and **FA-AIE-TPP** dots are internalized into MCF-7 cells as revealed by CLSM and flow cytometry (Figures 5.4 and 5.5), the lower IC_{50} of **FA-AIE-TPP** dots clearly indicates that localizing PS loaded nanocarriers in mitochondria helps enhance anticancer effects of PDT. The comparison between **AIE-TPP** and **FA-AIE-TPP** dots also reveals that the increased cellular uptake of the latter helps increase the amount of NPs accumulated at mitochondria to yield enhanced PDT. Moreover, the killing efficiency of **FA-AIE-TPP** dots towards MCF-7 cells also increases with the exposure time and light power.

PDT triggered cell death normally destroys the mitochondria membrane and triggers the release of cytochrome, leading to apoptosis process. We used fluorescein isothiocyanate (FITC)-tagged Annexin V to differentiate apoptotic cells from viable ones. As shown in Figures 5.6 D and E, incubating MCF-7 cells with **FA-AIE-TPP** dots in dark, almost no green fluorescence from Annexin V is observed. While upon

light irradiation, bright green fluorescence originated from Annexin V can be observed from cell membrane, indicating that MCF-7 cells undergo apoptosis process in the presence of **FA-AIE-TPP** dots and light irradiation.

5.3.5 Mitochondria Membrane Potential Study

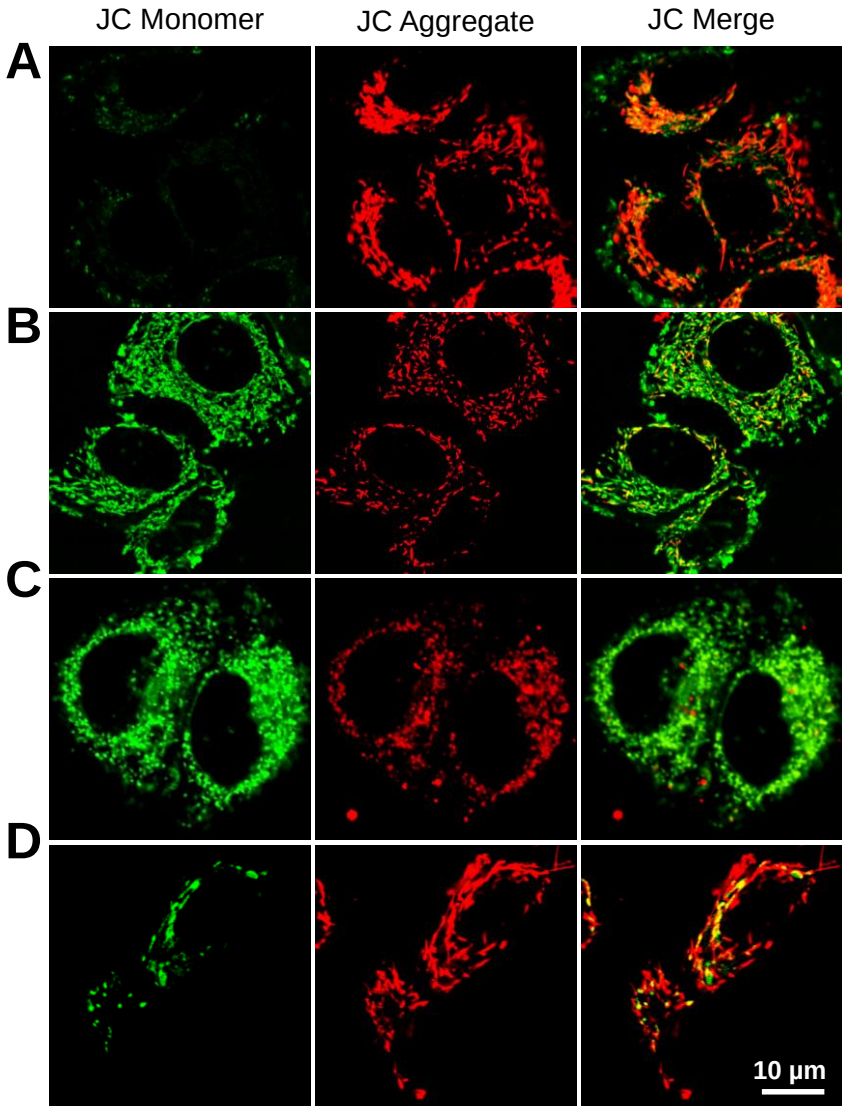

Figure 5.7. A-C) MMP changes of **FA-AIE-TPP** dots (20 μg/mL) treated MCF-7 cancer cells measured by JC-1 (2 μg/mL) after light irradiation (100 mW cm^{-2}) for A) 0, B) 5, and C) 10 min. D) MMP changes of MCF-7 without FA-AIE-TPP dots treatment under light irradiation. All the images share the same scale bar.

It has been reported that PDT treatment on mitochondria can cause mitochondria damage, leading to cell apoptosis and death. One of the characteristics of mitochondria damage or dysfunction is the loss of mitochondria membrane potential

(MMP), which will trigger the release of cytochrome at early stage of apoptosis.[164-166] We used a membrane-permeable JC-1 dye to monitor MMP changes during PDT treatment. JC-1 dye undergoes reversible fluorescence changes between its aggregate and monomer states. At high MMP level, JC-1 forms red emissive fluorescent aggregates on normal mitochondria, while it is shifted to green emissive monomer on depolarized mitochondria with low MMP. Figure 5.7 shows the representative confocal images of JC-1 assays, and the green/red (G/R) ratio helps quantify the MMP loss of MCF-7 cells during PDT. The accumulation of **FA-AIE-TPP** dots in mitochondria in dark does not de-polarize the mitochondria membrane as evidenced by the dim green fluorescence and bright red fluorescence from JC-1 dye. Upon exposure to white light, the JC-1 staining changes, where green fluorescence increases at the expense of red fluorescence (G/R ratio changes from 0.46 to 3.59 and 4.37), indicating the loss of MMPs and damage of mitochondria upon light irradiation. In addition, irradiation of blank MCF-7 cancer cells does not cause obvious MMP changes (Figure 5.7D), further indicating that mitochondria damage is due to the ROS generated by AIE dots under light illumination. It should be noted that the red fluorescence emitted from **FA-AIE-TPP** dots is still observable during PDT treatment, which provides the opportunity to visualize the morphology changes of mitochondria from characteristic tubular-like structure to dot-like structures after light irradiation.

5.3.6 Cell Migration Study

As the powerhouse of cells, mitochondrion provides the major energy for cancer cell activities, including proliferation, migration and metastasis. It is postulated that the dysfunction of mitochondria highly affects the ATP production and hence the migration of cancer cells. A cell-scratch spatula method is used to study the effects of AIE dots on cell migration before and after light irradiation. A scratch was applied to the cell

monolayer prior to 4h incubation with these three AIE dots (20 μg/mL based on **DPBA-TPE** mass concentration) and light irradiation (100 $mWcm^{-2}$, 10 min). The migration ratio is determined by the number of cells migrated to the wound area after PDT treatment to that of control cells without AIE dots treatment and light irradiation after 72 h post-culture (Figure 5.8). The AIE dots and light irradiation did not affect the migration ability of NIH-3T3 cells, as they migrated into the wound area with a very high migration ratio of ~100%. On the other hand, AIE dots in dark do not affect the migration ability of MCF-7 cells, but further light irradiation is able to inhibit the wound closure of AIE dots treated MCF-7 cells, with migration ratios of 74.2%, 54.1%, and 6.8% for **AIE-TPP**, **AIE-FA** and **FA-AIE-TPP** dots, respectively (Figures 5.8B). As cancer cells are highly metastatic, the inhibition of migration should also contribute to the anticancer therapy.

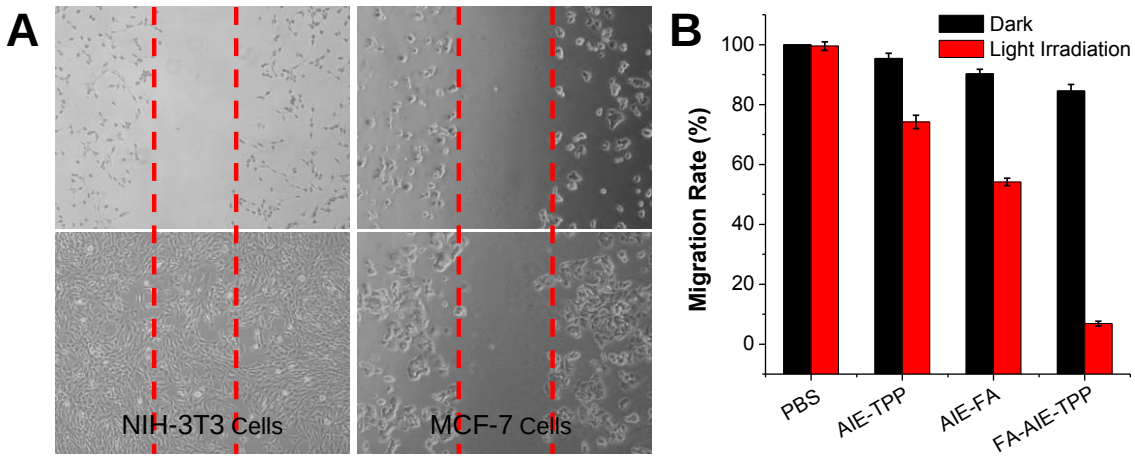

Figure 5.8. A) White field image of **FA-AIE-TPP** dots treated NIH-3T3 and MCF-7 cells before (up) and after 72 h culture (bottom). Both cells were incubated with **FA-AIE-TPP** dots (20 μg/mL based on **DPBA-TPE** mass concentration) for 4 h, followed by light exposure (100 mW/cm^2) for 10 min. B) The effects of AIE dots treatment on migration of MCF-7 cells with and without light irradiation.

5.4 Conclusion

In summary, we fabricated dual-targeted AIE dots with efficient ROS generation for FR-positive cancer cell and mitochondrial dual targeted image-guided PDT. The new AIE dots showed bright red fluorescence and efficient ROS generation under light irradiation. To specially target the mitochondria of a selective type of cancer cells, the AIE dot surfaces were decorated with folate acid and TPP. Folate acid promotes the cellular uptake to FR-positive cancer cells, and TPP drives AIE dots to accumulate in mitochondria. The generation of ROS at mitochondria is able to quickly depolarize and destroy the mitochondrial membrane, and largely affects cancer cell migration ability. Cell viability studies revealed that dual functionalized **FA-AIE-TPP** dots showed more efficient anticancer PDT effects than single ligand functionalized **AIE-TPP** or **AIE-FA** dots. Different from traditional approaches which require tedious processes to modify PSs for targeted PDT, this AIE dots strategy provides a new platform for cellular- and organelle-targeted image-guided PDT. Moreover, when the developed strategy is further applied to other imaging or therapeutic reagents, it opens new opportunities in drug delivery and cancer therapy.

CHAPTER 6

CONCLUSIONS AND RECOMMENDATIONS

6.1 Conclusions

Fluorogens with aggregation-induced emission (AIEgens) have recently received remarkably increasing attentions in biological applications due to their largely enhanced fluorescence in aggregated state, tuneable optical properties, and good photostability. As compared to conventional fluorescence probes including organic dyes, QDs, fluorescence proteins, the exploration of AIEgens and AIEgens based nanoparticles (NPs) in bioimaging and theranostic applications is promising with great potentials, but still in its very early stage. The main objective of this thesis is to develop AIEgens based organic dots (AIE dots) for targeted cancer cell or subcellular organelle detection, tracing, and therapy with high selectivity, good sensitivity and excellent therapeutic effects. The *in vivo* blood vascular integrity and leakage was also explored. These applications are of high importance in the early stage of cancer diagnosis, inflammation and infection detection, and the treatment of tumours. The detailed and significant findings obtained during the thesis study are summarized as following.

Firstly, we developed a facile and general encapsulation approach using DSPE-PEG as the matrix to fabricate AIE dots with ultrahigh brightness, good colloidal stability, and excellent photostability. Due to the existence of the PEG chains as the protective shells, the nonspecific interactions are largely suppressed, which increases the imaging sensitivity and contrast. Benefiting the excellent encapsulation ability of chosen DSPE-PEG, the obtained AIE dots showed high fluorescence quantum yield over 60%. Using the method we designed, the surface functional groups of the resultant AIE dots are easily amendable by simply changing the terminal groups of DSPE-PEG. In this chapter, the AIE dots are further conjugated with cell penetration peptide to enhance their cellular uptake towards targeted cells. The AIE dots showed excellent labelling performance towards all tested cells including primary cells and stem cells,

which outperforms the selected benchmark of non-viral green fluorescence protein (GFP) transfection method. These AIE dots showed excellent cellular retention where no leakage is observed during cell proliferation, and they can trace the activities of cells up to 10 days.

We further synthesized a hybrid AIE dots with surface gadolinium chelation and bright red fluorescence under two-photon excitation for *in vivo* imaging and detection of blood vascular integrity and leakage under inflammation. The PEG shells prevent the nonspecific interaction of AIE dots with biomolecules in blood vascular, which provides the clear, distinguishable and continuous red emissive flow inside blood vascular. Different from small organic dyes whose fluorescence are largely susceptible to surrounding environment, our AIE dots showed stable brightness in blood vessels. Under inflammation or infection, the vascular permeability will increase, and our AIE dots will leak outside from the blood vascular, serving as an *in vivo* fluorescence marker for blood vascular integrity and leakage. Moreover, the gadolinium contents chelated onto the AIE dots can also provide the quantitatively analysis of the leakage, providing a guidance of the inflammation severity. In this chapter we provide a new strategy to introduce magnetic modality to fluorescence NPs without affecting the optical properties. With the combination of two modalities, we provide more accurate and sensitive detection of inflammation.

Thirdly, we discovered that some AIEgens can act as photosensitizers (PSs). Taking TPETPADCM as an example, TPETPADCM is able to efficient generate reactive oxygen species (ROS) even in aggregated states. Utilizing the similar methods established in previous chapters, TPETPADCM was encapsulated into DSPE-PEG NPs, which is further conjugated with cRGD that can target towards $\alpha_v\beta_3$ integrin

overexpressed cancer cells. We demonstrated that the resultant TPETPADCM-cRGD dots are able to emit bright red fluorescence and efficiently generate ROS under proper light irradiation. They were further applied to visualize the targeted cancer cells and selectively kill them through the photodynamic effects. For the first time, we demonstrated AIEgens themselves can efficient generate ROS even in aggregated states. This PDT platform based on AIEgens is simple to design and synthesis, which offers new opportunities for image-guided PDT.

Due to short lifetime and action of radius of ROS, the performance of PDT is greatly limited to its subcellular distribution, as mitochondrion is the main targeted of ROS, the address of PSs to mitochondria will largely enhanced the PDT efficiency. As such, in addition to the image-guided PDT towards targeted cells as described in previous chapter, subcellular mitochondria targeting and labelling in living targeted cells was also carried out using cellular and mitochondria dual targeted AIE dots for enhanced photodynamic performance. A new AIEgen, **DPBA-TPE** with bright red emission and efficient ROS production was synthesized and encapsulated to DSPE-PEG matrix to form the AIE dots. The surfaces of AIE dots were further functionalized with folic acid and TPP to address the AIE dots to the mitochondria of folate receptor positive cancer cells. The generation of ROS at mitochondria is able to quickly depolarize and destroy the mitochondrial membrane, which showed more efficient anticancer PDT effects than sole cellular targeted or mitochondria targeted AIE dots. Moreover, this facile strategy is of high importance in subcellular targeting imaging and therapy, as it does not require tedious processes to modify drugs or dyes.

In this thesis, we have successfully demonstrated the design of AIE dots for different biological applications varying from *in vitro* to *in vivo*, for cells to organelles, from diagnosis to therapy. Instead of fight against the ACQ effects associated with

aggregation, the developments of AIEgens are able to take the advantages of nature and inevitable phenomenon of aggregation, making it possible to fabricate NPs with high brightness for detection and imaging in biological environment. Instead of chemical modification of AIEgens to synthesize light-up probes or AIE nanoparticles, this thesis clearly demonstrated a facile and general approach to fabricate AIE dots with ultra-high brightness and other optical properties to fulfil different requirements in these biological applications. The ultrahigh brightness, tuneable emission colour, good photostability and colloidal stability make them promising contrast reagents over fluorescent proteins, organic dyes and quantum dots. In addition, the efficient ROS production in aggregate state further expanded their applications in photodynamic therapy. In the view of material science and applications, the AIE dots with desired optical or therapeutic properties can be fine-tuned by choosing the suitable AIEgens, matrices or strategies. Due to the ACQ effects of conventional fluorogens, the fabrication of nanoparticles with bright fluorescence or efficient ROS production is greatly limited, this thesis thus provides a new solution to fabricate fluorescent AIE nanoparticles with high brightness or efficient ROS generation for imaging, theranostic and other biological applications.

6.2 Recommendations

We have successfully demonstrated the synthesis of AIE dots in different biological applications, which possess promising potentials that are worth of further exploration. With the rapid development of AIE field, and in the parallel to the study of this thesis, many new approaches and applications of AIE dots have been demonstrated. Based on these results obtained in this thesis and others demonstrations, we propose some recommendations for further optimization and investigation of AIE dots in more broadened biological applications.

AIE dots with ultrahigh brightness have been successfully synthesized in this thesis. The current method for AIE dots fabrications demonstrated in this thesis is based on DSPE-PEG as the matrix. This is due to the excellent encapsulation performance of DSPE-PEG, and the high colloidal stability of the resultant AIE dots. The method demonstrated in this thesis is capable to deliver AIE dots with size around ~30 nm. Although they have shown promising performance in biological applications, the AIE dots with different sizes are still highly desirable in biological applications. For example, the nucleus imaging by AIE dots in living cells is still limited, due to the relative larger particle size than the nucleus membrane pore. As a consequence, it would hold great potentials to design and develop AIE dots with different particle sizes. It should be noted that, although the estimation of AIE nanoparticles based on gravimetric measurement via diving the sample by unit weight of nanoparticles is simple and straightforward, its error ranges are largely dependent on many factors. For example, an average diameter is used for concentration estimation due to the intrinsic polydispersity of polymeric nanoparticles. For accurate estimation, the size distribution of AIE particles should be as small as possible, which required the optimization of current AIE dot fabrication to reduce the polydispersity. On the other hand, the particle density estimation also need to improve, as small inorganic particles in nm range can be well dispersed in water even if their density is much larger than water. And the use of the bulk matrix and AIEgens density also introduce experimental error. New and advanced analytical technique and theoretical calculation approach should be developed for reduction the error of nanoparticle concentration determination.

Another important aspect need further investigation is the packing and distribution of AIEgens inside these organic dots. As implied by its name, AIEgens showed intensified emission that is aroused by the formation of aggregates. Benefiting

from this feature, we are able to fabricate the AIE dots with high emission for biological applications. However, currently rare reports how these AIEgens are aggregated and packed inside these NPs, and how they will affect the brightness of the resultant dots. It is also observed that the brightness of AIE dots is not always as the same as these AIEgen aggregates in water at the same concentration. It indicates that we still have not made the full use of the aggregation of these AIEgens, which still awaits for the further exploration. Moreover, the mechanism of these AIEgens with efficient ROS production in aggregate state also need further investigation.

Multifunctional AIE dots integrated with different imaging modalities also need further exploring. Currently, the applications of AIE dots is still limited to *in vitro* or *in vivo* subcutaneous level due to the limited penetration depth and the interference from biological tissues. This can be overcome by integrated the fluorescence imaging with other modalities as such magnetic resonance imaging (MRI) to provide multiple signals. MRI can provide images with high penetration depth but low resolution. This combination of fluorescence AIE dots with MRI reagents could take the advantage of both imaging modalities. We have conducted some works by chelating gadolinium onto AIE dots surface for dual modality detection of blood vascular leakage (Chapter 3), but more exploration still required.

REFERENCES

(1) Willmann, J.K., van Bruggen, N., Dinkelborg, L.M., and Gambhir, S.S. *Nat. Rev. Drug Discov.* **2008**, *7*, 591.

(2) Gusnard, D.A. and Raichle, M.E. *Nat. Rev. Neurosci.* **2001**, *2*, 685.

(3) Nilsson, K.P.R., Herland, A., Hammarstrom, P., and Inganas, O. Biochemistry, **2005**, *44*, 3718.

(4) Åslund, A., Sigurdson, C.J., Klingstedt, T.s., Grathwohl, S., Bolmont, T., Dickstein, D.L., Glimsdal, E., Prokop, S., Lindgren, M., Konradsson, P., Holtzman, D.M., Hof, P.R., Heppner, F.L., Gandy, S., Jucker, M., Aguzzi, A., Hammarstrom, P., and Nilsson, K.P.R. *ACS Chem. Biol.* **2009**, *4*, 673.

(5) Kondepati, V.R., Heise, H.M., and Backhaus, J. *Anal. Bioanal. Chem.* **2007**, *390*, 125.

(6) Weissleder, R.; Pittet, M. J. *Nature* **2008**, *452*, 580.

(7) Phelps, M. E. *Proc. Natl. Acad. Sci. U. S. A.* **2000**, *97*, 9226.

(8) Cheon, J.; Lee, J.-H. *Acc. Chem. Res.* **2008**, *41*, 1630.

(9) Edelman, R. R.; Warach, S. *N. Engl. J. Med.* **1993**, *328*, 708.

(10) Gupta, A. K.; Gupta, M. *Biomaterials* **2005**, *26*, 3995.

(11) Laurent, S.; Forge, D.; Port, M.; Roch, A.; Robic, C.; Vander Elst, L.; Muller, R. N. *Chem. Rev.* **2008**, *108*, 2064.

(12) Fujimoto, J. G. *Nat. Biotechnol.* **2003**, *21*, 1361.

(13) Wang, L. V. *Nat Photon* **2009**, *3*, 503.

(14) Zhang, H. F.; Maslov, K.; Stoica, G.; Wang, L. V. *Nat. Biotechnol.* **2006**, *24*, 848.

(15) Stephens, D. J.; Allan, V. J. *Science* **2003**, *300*, 82.

(16) Swedlow, J. R.; Goldberg, I.; Brauner, E.; Sorger, P. K. *Science* **2003**, *300*, 100.

(17) Larson, D. R.; Zipfel, W. R.; Williams, R. M.; Clark, S. W.; Bruchez, M. P.; Wise, F. W.; Webb, W. W. *Science* **2003**, *300*, 1434.

(18) Giepmans, B. N. G.; Adams, S. R.; Ellisman, M. H.; Tsien, R. Y. *Science* **2006**, *312*, 217.

(19) Heim, R.; Cubitt, A. B.; Tsien, R. Y. *Nature* **1995**, *373*, 663.

(20) Tsien, R. Y. *Angew. Chem. Int. Ed.* **2009**, *48*, 5612.

(21) Zacharias, D. A.; Violin, J. D.; Newton, A. C.; Tsien, R. Y. *Science* **2002**, *296*, 913.

(22) Kircher, M. F.; Gambhir, S. S.; Grimm, J. *Nat. Rev. Clin. Oncol.* **2011**, *8*, 677.

(23) Robbins, P. D.; Ghivizzani S. C. *Pharmacol. Ther.* **1998**, *80*, 35.

(24) Hamm, A.; Krott, N.; Breibach, I.; Blindt, R.; Bosserhoff, A. K. *Tissue Eng.* **2002**, *8*, 235.

(25) L. Santos, J.; Pandita, D.; Rodrigues, J.; P. Pego, A.; L. Granja, P.; Tomas, H. *Curr. Gene Ther.* **2011**, *11*, 46.

(26) Morris, K. V.; Chan, S. W.-L.; Jacobsen, S. E.; Looney, D. J. *Science* **2004**, *305*, 1289.

(27) Swenson, E. S.; Price, J. G.; Brazelton, T.; Krause, D. S. *STEM CELLS* **2007**, *25*, 2593.

(28) Wiedenmann, J.; Oswald, F.; Nienhaus, G. U. *IUBMB Life* **2009**, *61*, 1029.

(29) Birks, J. B. *Photophysics of Aromatic Molecules*; Wiley: London, 1970.

(30) Wang, D.; Qian, J.; He, S.; Park, J. S.; Lee, K.-S.; Han, S.; Mu, Y. *Biomaterials* **2011**, *32*, 5880.

(31) Dubertret, B.; Skourides, P.; Norris, D. J.; Noireaux, V.; Brivanlou, A. H.; Libchaber, A. *Science* **2002**, *298*, 1759.

(32) Michalet, X.; Pinaud, F. F.; Bentolila, L. A.; Tsay, J. M.; Doose, S.; Li, J. J.; Sundaresan, G.; Wu, A. M.; Gambhir, S. S.; Weiss, S. *Science* **2005**, *307*, 538.

(33) Smith, A. M.; Duan, H.; Mohs, A. M.; Nie, S. *Adv. Drug Delivery Rev.* **2008**, *60*, 1226.

(34) Hardman, R. *Environ. Health Perspect.* **2006**, *114*, 165.

(35) Zhelev, Z.; Ohba, H.; Bakalova, R. *J. Am. Chem. Soc.* **2006**, *128*, 6324.

(36) Valeur, B. *Molecular Fluorescence: Principle and Applications*; Wiley-VCH: Weinheim, 2002.

(37) Borisov, S. M.; Wolfbeis, O. S. *Chem. Rev.* **2008**, *108*, 423.

(38) Jares-Erijman, E. A.; Jovin, T. M. *Nat. Biotechnol.* **2003**, *21*, 1387.

(39) Ding, D.; Li, K.; Liu, B.; Tang, B. Z. *Acc. Chem. Res.* **2013**, *46*, 2441.

(40) He, F.; Tang, Y.; Wang, S.; Li, Y.; Zhu, D. *J. Am. Chem. Soc.* **2005**, *127*, 12343.

(41) Hecht, S.; Fréchet, J. M. J. *Angew. Chem. Int. Ed.* **2001**, *40*, 74.

(42) Hong, Y.; Lam, J. W. Y.; Tang, B. Z. *Chem. Commun.* **2009**, 4332.

(43) Luo, J.; Xie, Z.; Lam, J. W. Y.; Cheng, L.; Chen, H.; Qiu, C.; Kwok, H. S.; Zhan, X.; Liu, Y.; Zhu, D.; Tang, B. Z. *Chem. Commun.* **2001**, 1740.

(44) Tang, B. Z.; Zhan, X.; Yu, G.; Sze Lee, P. P.; Liu, Y.; Zhu, D. *J. Mater. Chem.* **2001**, *11*, 2974.

(45) Zhao, Q.; Li, K.; Chen, S.; Qin, A.; Ding, D.; Zhang, S.; Liu, Y.; Liu, B.; Sun, J. Z.; Tang, B. Z. *J. Mater. Chem.* **2012**, *22*, 15128.

(46) Mei, J.; Hong, Y.; Lam, J. W. Y.; Qin, A.; Tang, Y.; Tang, B. Z. *Adv. Mater.* **2014**, *26*, 5429.

(47) Hu, R.; Leung, N. L. C.; Tang, B. Z. *Chem. Soc. Rev.* **2014**, *43*, 4494.

(48) Chen, J.; Law, C. C. W.; Lam, J. W. Y.; Dong, Y.; Lo, S. M. F.; Williams, I. D.; Zhu, D.; Tang, B. Z. *Chem. Mater.* **2003**, *15*, 1535.

(49) Luo, J.; Song, K.; Gu, F. l.; Miao, Q. *Chem. Sci.* **2011**, *2*, 2029.

(50) Li, Z.; Qin, A. *Natl. Sci. Rev.* **2014**, *1*, 22.

(51) Toupin, M.; Brousse, T.; Bélanger, D. *Chem. Mater.* **2004**, *16*, 3184.

(52) Yuan, Y.; Zhang, C.-J.; Gao, M.; Zhang, R.; Tang, B. Z.; Liu, B. *Angew. Chem. Int. Ed.* **2015**, *54*, 1780.

(53) Zhang, X.; Zhang, X.; Tao, L.; Chi, Z.; Xu, J.; Wei, Y. *J. Mater. Chem. B* **2014**, *2*, 4398.

(54) Kim, S.; Pudavar, H. E.; Bonoiu, A.; Prasad, P. N. *Adv. Mater.* **2007**, *19*, 3791.

(55) Kim, S.; Ohulchanskyy, T. Y.; Pudavar, H. E.; Pandey, R. K.; Prasad, P. N. *J. Am. Chem. Soc.* **2007**, *129*, 2669.

(56) Faisal, M.; Hong, Y.; Liu, J.; Yu, Y.; Lam, J. W. Y.; Qin, A.; Lu, P.; Tang, B. Z. *Chem. Eur. J.* **2010**, *16*, 4266.

(57) Li, M.; Lam, J. W. Y.; Mahtab, F.; Chen, S.; Zhang, W.; Hong, Y.; Xiong, J.; Zheng, Q.; Tang, B. Z. *J. Mater. Chem. B* **2013**, *1*, 676.

(58) Mahtab, F.; Lam, J. W. Y.; Yu, Y.; Liu, J.; Yuan, W.; Lu, P.; Tang, B. Z. *Small* **2011**, *7*, 1448.

(59) Mahtab, F.; Yu, Y.; Lam, J. W. Y.; Liu, J.; Zhang, B.; Lu, P.; Zhang, X.; Tang, B. Z. *Adv. Funct. Mater.* **2011**, *21*, 1733.

(60) Zhang, X.; Zhang, X.; Wang, S.; Liu, M.; Zhang, Y.; Tao, L.; Wei, Y. *ACS Appl. Mater. Interfaces* **2013**, *5*, 1943.

(61) Li, K.; Liu, B. *Chem. Soc. Rev.* **2014**, *43*, 6570.

(62) Li, M.; Hong, Y.; Wang, Z.; Chen, S.; Gao, M.; Kwok, R. T. K.; Qin, W.; Lam, J. W. Y.; Zheng, Q.; Tang, B. Z. *Macromol. Rapid Commun.* **2013**, *34*, 767.

(63) Wang, Z.; Chen, S.; Lam, J. W. Y.; Qin, W.; Kwok, R. T. K.; Xie, N.; Hu, Q.; Tang, B. Z. *J. Am. Chem. Soc.* **2013**, *135*, 8238.

(64) Ma, C.; Ling, Q.; Xu, S.; Zhu, H.; Zhang, G.; Zhou, X.; Chi, Z.; Liu, S.; Zhang, Y.; Xu, J. *Macromol. Biosci.* **2014**, *14*, 235.

(65) Zhang, X.; Liu, M.; Yang, B.; Zhang, X.; Chi, Z.; Liu, S.; Xu, J.; Wei, Y. *Polym. Chem.* **2013**, *4*, 5060.

(66) Huang, Z.; Zhang, X.; Zhang, X.; Yang, B.; Zhang, Y.; Wang, K.; Yuan, J.; Tao, L.; Wei, Y. *Polym. Chem.* **2015**, *6*, 2133.

(67) Zhang, X.; Zhang, X.; Yang, B.; Liu, M.; Liu, W.; Chen, Y.; Wei, Y. *Polym. Chem.* **2014**, *5*, 356.

(68) Ding, D.; Kwok, R. T. K.; Yuan, Y.; Feng, G.; Tang, B. Z.; Liu, B. *Mater. Horiz.* **2015**, *2*, 100.

(69) Yuan, Y.; Kwok, R. T. K.; Zhang, R.; Tang, B. Z.; Liu, B. *Chem. Commun.* **2014**, *50*, 11465.

(70) Zhang, X.; Zhang, X.; Yang, B.; Liu, M.; Liu, W.; Chen, Y.; Wei, Y. *Polym. Chem.* **2014**, *5*, 399.

(71) Wu, W.-C.; Chen, C.-Y.; Tian, Y.; Jang, S.-H.; Hong, Y.; Liu, Y.; Hu, R.; Tang, B. Z.; Lee, Y.-T.; Chen, C.-T.; Chen, W.-C.; Jen, A. K. Y. *Adv. Funct. Mater.* **2010**, *20*, 1413.

(72) Li, K.; Jiang, Y.; Ding, D.; Zhang, X.; Liu, Y.; Hua, J.; Feng, S.-S.; Liu, B. *Chem. Commun.* **2011**, *47*, 7323.

(73) Geng, J.; Li, K.; Qin, W.; Ma, L.; Gurzadyan, G. G.; Tang, B. Z.; Liu, B. *Small* **2013**, *9*, 2012.

(74) Qin, W.; Ding, D.; Liu, J.; Yuan, W. Z.; Hu, Y.; Liu, B.; Tang, B. Z. *Adv. Funct. Mater.* **2012**, *22*, 771.

(75) Qin, W.; Li, K.; Feng, G.; Li, M.; Yang, Z.; Liu, B.; Tang, B. Z. *Adv. Funct. Mater.* **2014**, *24*, 635.

(76) Li, K.; Qin, W.; Ding, D.; Tomczak, N.; Geng, J.; Liu, R.; Liu, J.; Zhang, X.; Liu, H.; Liu, B.; Tang, B. Z. *Sci. Rep.* **2013**, *3*, 1150.

(77) Li, K.; Zhu, Z.; Cai, P.; Liu, R.; Tomczak, N.; Ding, D.; Liu, J.; Qin, W.; Zhao, Z.; Hu, Y.; Chen, X.; Tang, B. Z.; Liu, B. *Chem. Mater.* **2013**, *25*, 4181.

(78) Geng, J.; Li, K.; Ding, D.; Zhang, X.; Qin, W.; Liu, J.; Tang, B. Z.; Liu, B. *Small* **2012**, *8*, 3655.

(79) Yu, Y.; Feng, C.; Hong, Y.; Liu, J.; Chen, S.; Ng, K. M.; Luo, K. Q.; Tang, B. Z. *Adv. Mater.* **2011**, *23*, 3298.

(80) Ding, D.; Li, K.; Qin, W.; Zhan, R.; Hu, Y.; Liu, J.; Tang, B. Z.; Liu, B. *Adv. Healthcare Mater.* **2013**, *2*, 500.

(81) Ding, D.; Mao, D.; Li, K.; Wang, X.; Qin, W.; Liu, R.; Chiam, D. S.; Tomczak, N.; Yang, Z.; Tang, B. Z.; Kong, D.; Liu, B. *ACS Nano* **2014**, *8*, 12620.

(82) Ding, D.; Goh, C. C.; Feng, G.; Zhao, Z.; Liu, J.; Liu, R.; Tomczak, N.; Geng, J.; Tang, B. Z.; Ng, L. G.; Liu, B. *Adv. Mater.* **2013**, *25*, 6083.

(83) Dolmans, D. E.; Fukumura, D.; Jain, R. K. *Nat. Rev. Cancer* **2003**, 3, 380.

(84) Castano, A. P.; Demidova, T. N.; Hamblin, M. R. *Photodiagn. Photodyn. Ther.* **2004**, *1*, 279.

(85) Sekkat, N.; van den Bergh, H.; Nyokong, T.; Lange, N. *Molecules* **2012**, *17*, 98.

(86) Andersson, D. I.; Hughes, D. *Nat. Rev. Micro.* **2010**, *8*, 260.

(87) Zhang, C.; Jin, S.; Li, S.; Xue, X.; Liu, J.; Huang, Y.; Jiang, Y.; Chen, W.-Q.; Zou, G.; Liang, X.-J. *ACS Appl. Mater. Interfaces* **2014**, *6*, 5212.

(88) Hu, F.; Huang, Y.; Zhang, G.; Zhao, R.; Yang, H.; Zhang, D. *Anal. Chem.* **2014**, *86*, 7987.

(89) Wu, X.; Liu, H.; Liu, J.; Haley, K. N.; Treadway, J. A.; Larson, J. P.; Ge, N.; Peale, F.; Bruchez, M. P. *Nat. Biotechnol.* **2003**, *21*, 41.

(90) Zrazhevskiy, P.; Gao, X. *Nat. Commun.* **2013**, *4*, 1619.

(91) Denning, D. P.; Hatch, V.; Horvitz, H. R. *Nature* **2012**, *488*, 226.

(92) Nakano, S.; Stillman, B.; Horvitz, H. R. *Cell* **2011**, *147*, 1525.

(93) Hong, H.; Yang, Y.; Zhang, Y.; Cai, W. *Curr. Top. Med. Chem.* **2010**, *10*, 1237.

(94) Ly, H. Q.; Frangioni, J. V.; Hajjar, R. J. *Nat. Clin. Pract. Cardiovasc Med.* **2008**, *5*, 96.

(95) Yan, L.; Han, Y.; He, Y.; Xie, H.; Liu, J.; Zhao, L.; Wang, J.; Gao, L.; Fan, D. *Stem Cell Rev.* **2007**, *3*, 265.

(96) Guo, Y.; Su, L.; Wu, J.; Zhang, D.; Zhang, X.; Zhang, G.; Li, T.; Wang, J.; Liu, C. *Cytotechnology* **2012**, *64*, 391.

(97) Wang, S.; Hazelrigg, T. *Nature* **1994**, *369*, 400.

(98) Tsien, R. Y. *Angew. Chem. Int. Ed.* **2009**, *48*, 5612.

(99) Butko, M. T.; Yang, J.; Geng, Y.; Kim, H. J.; Jeon, N. L.; Shu, X.; Mackey, M. R.; Ellisman, M. H.; Tsien, R. Y.; Lin, M. Z. *Nat. Neurosci.* **2012**, *15*, 1742.

(100) Li, S.-D.; Huang, L. *J. Controlled Release* **2007**, *123*, 181.

(101) Ang, D.; Tay, C. Y.; Tan, L. P.; Preiser, P. R.; Ramanujan, R. V. *Mater. Sci. Eng.: C* **2011**, *31*, 1445.

(102) Jaiswal, J. K.; Mattoussi, H.; Mauro, J. M.; Simon, S. M. *Nat. Biotechnol.* **2003**, *21*, 47.

(103) Gao, Y.; Cui, Y.; Chan, J. K.; Xu, C. *Am. J. Nucl. Med. Mol. Imaging* **2013**, *3*, 232.

(104) Idris, N. M.; Li, Z.; Ye, L.; Wei Sim, E. K.; Mahendran, R.; Ho, P. C.-L.; Zhang, Y. *Biomaterials* **2009**, *30*, 5104.

(105) Sutton, E.; Henning, T.; Pichler, B.; Bremer, C.; Daldrup-Link, H. *Eur. J. Radiol.* **2008**, *18*, 2021.

(106) Christophe Youta, D.; Maya, K.; Rima, Z.; Regis, M.; Didier, B. *Nanotechnology* **2010**, *21*, 355102.

(107) Marks, K. M.; Nolan, G. P. *Nat. Methods* **2006**, *3*, 591.

(108) Chithrani, B. D.; Chan, W. C. W. *Nano Lett.* **2007**, *7*, 1542.

(109) Birks, J. B. *Photophysics of Aromatic Molecules*; Wiley: London, 1970.

(110) Hong, Y.; Lam, J. W. Y.; Tang, B. Z. *Chem. Soc. Rev.* **2011**, *40*, 5361.

(111) Zhao, Z.; W. Y. Lam, J.; Zhong Tang, B. *Curr. Org. Chem.* **2010**, *14*, 2109.

(112) Liu, J.; Lam, J. Y.; Tang, B. *J. Inorg. Org. Polym. Mater.* **2009**, *19*, 249.

(113) Yuan, W. Z.; Lu, P.; Chen, S.; Lam, J. W. Y.; Wang, Z.; Liu, Y.; Kwok, H. S.; Ma, Y.; Tang, B. Z. *Adv. Mater.* **2010**, *22*, 2159.

(114) Chi, Z.; Zhang, X.; Xu, B.; Zhou, X.; Ma, C.; Zhang, Y.; Liu, S.; Xu, J. *Chem. Soc. Rev.* **2012**, *41*, 3878.

(115) Li, K.; Qin, W.; Ding, D.; Tomczak, N.; Geng, J.; Liu, R.; Liu, J.; Zhang, X.; Liu, H.; Liu, B.; Tang, B. Z. *Sci. Rep.* **2013**, *3*, 1150.

(116) Zhao, Z.; Deng, C.; Chen, S.; Lam, J. W. Y.; Qin, W.; Lu, P.; Wang, Z.; K wok, H. S.; Ma, Y.; Qiu, H.; Tang, B. Z. *Chem. Commun.* **2011**, *47*, 8847

(117) Hu, R.; Lager, E.; Aguilar-Aguilar, A. l.; Liu, J.; Lam, J. W. Y.; Sung, H. H. Y.; Williams, I. D.; Zhong, Y.; Wong, K. S.; Peña-Cabrera, E.; Tang, B. Z. *J. Phys. Chem. C* **2009**, *113*, 15845.

(118) Piantavigna, S.; McCubbin, G. A.; Boehnke, S.; Graham, B.; Spiccia, L.; Martin, L. L. *Biochem. Biophys. Acta, Biomembr.* **2011**, *1808*, 1811.

(119) Kaplan, I. M.; Wadia, J. S.; Dowdy, S. F. *J. Controlled Release* **2005**, *102*, 247.

(120) *Calcium phosphate-mediated transfection of eukaryotic cells. Nat. Methods* **2005**, *4*, 319.

(121) Tsai, Y.-T.; Zhou, J.; Weng, H.; Shen, J.; Tang, L.; Hu, W.-J. *Adv. Healthcare Mater.* **2014**, *3*, 221.

(122) do Nascimento, G. C.; Leite-Panissi, C. R. A. *Physiol. Behav.* **2014**, *125*, 1.

(123) Altay, O.; Suzuki, H.; Hasegawa, Y.; Ostrowski, R. P.; Tang, J.; Zhang, J. H. *Neurobiol. Dis.* **2014**, *62*, 365.

(124) Jones, H. A. *Proc. Am. Thorac. Soc.* **2005**, *2*, 545.

(125) Sigovan, M.; Boussel, L.; Sulaiman, A.; Sappey-Marinier, D.; Alsaid, H.; Desbleds-Mansard, C.; Ibarrola, D.; Gamondès, D.; Corot, C.; Lancelot, E.; Raynaud, J.-S.; Vives, V.; Laclédère, C.; Violas, X.; Douek, P. C.; Canet-Soulas, E. *Radiology* **2009**, *252*, 401.

(126) Zhuang, H.; Alavi, A. *Semin. Nucl. Med.* **2002**, *32*, 47.

(127) Schuster, D. P.; Kozlowski, J.; Hogue, L.; Ferkol, T. W. *Exp. Lung Res.* **2003**, *29*, 45.

(128) Lindner, J. R.; Song, J.; Xu, F.; Klibanov, A. L.; Singbartl, K.; Ley, K.; Kaul, S. *Circulation* **2000**, *102*, 2745.

(129) Rudd, J. H. F.; Hyafil, F.; Fayad, Z. A. *Arterioscler., Thromb., Vasc. Biol.* **2009**, *29*, 1009.

(130) Boerman, O. C.; Rennen, H.; Oyen, W. J. G.; Corstens, F. H. M. *Semin. Nucl. Med.* **2001**, *31*, 286.

(131) Vandenbroucke, E.; Mehta, D.; Minshall, R.; Malik, A. B. *Ann. N. Y. Acad. Sci.* **2008**, *1123*, 134.

(132) Saria, A.; Lundberg, J. M. *J. Neurosci. Methods* **1983**, *8*, 41.

(133) Xu, Q.; Qaum, T.; Adamis, A. P. *Invest. Ophthalmol. Visual Sci.* **2001**, *42*, 789.

(134) Marmarou, A., Bullock, R., Avezaat, C., Baethmann, A., Becker, D., Brock, M., Hoff, J., Nagai, H., Reulen, H.-J., Teasdale, G. *Intracranial Pressure and Neuromonitoring in Brain Injury*; Springer: Vienna, 1998.

(135) Hamer, P. W.; McGeachie, J. M.; Davies, M. J.; Grounds, M. D. *J. Anat.* **2002**, *200*, 69.

(136) Hawkins, B. T.; Egleton, R. D. *J. Neurosci. Methods* **2006**, *151*, 262.

(137) Chen, X.; Gambhir, S. S.; Cheon, J. *Acc. Chem. Res.* **2011**, *44*, 841.

(138) Yang, K.; Feng, L.; Shi, X.; Liu, Z. *Chem. Soc. Rev.* **2013**, *42*, 530.

(139) Dolmans, D. E.; Fukumura, D.; Jain, R. K. *Nat. Rev. Cancer* **2003**, *3*, 380.

(140) Gohy, J. F.; Zhao, Y. *Chem. Soc. Rev.* **2013**, *42*, 7117.

(141) Rai, P.; Mallidi, S.; Zheng, X.; Rahmanzadeh, R.; Mir, Y.; Elrington, S.; Khurshid, A.; Hasan, T. *Adv. Drug. Delivery Rev.* **2010**, *62*, 1094.

(142) Celli, J. P.; Spring, B. Q.; Rizvi, I.; Evans, C. L.; Samkoe, K. S.; Verma, S.; Pogue, B. W.; Hasan, T. *Chem. Rev.* **2010**, *110*, 2795.

(143) Castano, A. P.; Demidova, T. N.; Hamblin, M. R. *Photodiagn. Photodyn. Ther.* **2004**, *1*, 279.

(144) Sekkat, N.; van den Bergh, H.; Nyokong, T.; Lange, N. *Molecules* **2012**, *17*, 98.

(145) Park, S. Y.; Baik, H. J.; Oh, Y. T.; Oh, K. T.; Youn, Y. S.; Lee, E. S. *Angew. Chem. Int. Ed* **2011**, *50*, 1644.

(146) Cho, Y.; Choi, Y. *Chem. Commun.* **2012**, *48*, 9912.

(147) Zheng, G.; Chen, J.; Stefflova, K.; Jarvi, M.; Li, H.; Wilson, B. C. *Proc. Natl. Acad. Sci. U.S.A.* **2007**, *104*, 8989.

(148) Ding, D.; Li, K.; Liu, B.; Tang, B. Z. *Acc. Chem. Res.* **2013**, *46*, 2441.

(149) Hong, Y. N.; Lam, J. W. Y.; Tang, B. Z. *Chem. Soc. Rev.* **2011**, *40*, 5361.

(150) Qin, W.; Ding, D.; Liu, J.; Yuan, W. Z.; Hu, Y.; Liu, B.; Tang, B. Z. *Adv. Funct. Mater.* **2012**, *22*, 771.

(151) Xue, X.; Zhao, Y.; Dai, L.; Zhang, X.; Hao, X.; Zhang, C.; Huo, S.; Liu, J.; Liu, C.; Kumar, A.; Chen, W.-Q.; Zou, G.; Liang, X.-J. *Adv. Mater.* **2014**, *26*, 712.

(152) Yuan, Y.; Kwok, R. T.; Tang, B. Z.; Liu, B. *J. Am. Chem. Soc.* **2014**, *136*, 2546.

(153) Li, Y.; Wu, Y.; Chang, J.; Chen, M.; Liu, R.; Li, F. *Chem. Commun.* **2013**, *49*, 11335.

(154) Yuan, Y.; Kwok, R. T.; Feng, G.; Liang, J.; Geng, J.; Tang, B. Z.; Liu, B. *Chem. Commun.* **2014**, *50*, 295.

(155) Huang, X.; Gu, X.; Zhang, G.; Zhang, D. *Chem. Commun.* **2012**, *48*, 12195.

(156) Shi, H.; Kwok, R. T. K.; Liu, J.; Xing, B.; Tang, B. Z.; Liu, B. *J. Am. Chem. Soc.* **2012**, *134*, 17972.

(157) Chang, C.-C.; Hsieh, M.-C.; Lin, J.-C.; Chang, T.-C. *Biomaterials* **2012**, *33*, 897.

(158) Wang, X.; Peralta, S.; Moraes, C. T. *Adv. Cancer Res.* **2013**, 119, 127.

(159) Rajendran, L.; Knolker, H.-J.; Simons, K. *Nat. Rev. Drug Discov.* **2010**, *9*, 29.

(160) Weigl, S.; Paradiso, A.; Tommasi, S. *Curr. Genomics* **2013**, *14*, 195.

(161) Wong, K. K. Y.; Liu, X. L. *Pediatr. Surg. Int.* **2012**, *28*, 943.

(162) Lim, C. S. *Adv. Drug Delivery Rev.* **2007**, *59*, 697.

(163) Torchilin, V. P. *Annu. Rev. Biomed. Eng.* **2006**, *8*, 343.

(164) Lam, M.; Oleinick, N. L.; Nieminen, A.-L. *J. Biol. Chem.* **2001**, *276*, 47379.

(165) Hilf, R. *J. Bioenerg. Biomembr.* **2007**, *39*, 85.

(166) Ngen, E. J.; Rajaputra, P.; You, Y. *Bioorg. Med. Chem.* **2009**, *17*, 6631.

(167) Rajaputra, P.; Nkepang, G.; Watley, R.; You, Y. *Bioorg. Med. Chem.* **2013**, *21*, 379.

(168) Moan, J.; Berg, K. *Photochem. Photobiol.* **1991**, *53*, 549.

(169) Skovsen, E.; Snyder, J. W.; Lambert, J. D. C.; Ogilby, P. R. *J. Phys. Chem. B* **2005**, *109*, 8570.

(170) Kim, S.; Tachikawa, T.; Fujitsuka, M.; Majima, T. *J. Am. Chem. Soc.* **2014**, *136*, 11707.

(171) Dickinson, B. C.; Chang, C. J. *J. Am. Chem. Soc.* **2008**, *130*, 9638.

(172) Sakhrani, N. M.; Padh, H. *Drug Des., Dev. Ther.* **2013**, *7*, 585.

(173) Li, S. P. Y.; Lau, C. T. S.; Louie, M. W.; Lam, Y. W.; Cheng, S. H.; Lo, K. K. W. *Biomaterials* **2013**, *34*, 7519.

(174) Prasad, P.; Khan, I.; Kondaiah, P.; Chakravarty, A. R. *Chem.-Eur. J.* **2013**, *19*, 17445.

(175) Xu, J.; Zeng, F.; Wu, H.; Hu, C.; Wu, S. *Biomacromolecules* **2014**, *15*, 4249.

(176) Hu, Q.; Gao, M.; Feng, G.; Liu, B. *Angew. Chem. Int. Ed.* **2014**, *53*, 14225.

(177) Boddapati, S. V.; D'Souza, G. G. M.; Erdogan, S.; Torchilin, V. P.; Weissig, V. *Nano Lett.* **2008**, *8*, 2559.

(178) Sharma, A.; Soliman, G. M.; Al-Hajaj, N.; Sharma, R.; Maysinger, D.; Kakkar, A. *Biomacromolecules* **2011**, *13*, 239.

(179) Breunig, M.; Bauer, S.; Goepferich, A. *Eur. J. Pharm, Biopharm.* **2008**, *68*, 112.

(180) Ganta, S.; Devalapally, H.; Shahiwala, A.; Amiji, M. *J. Controlled Release* **2008**, *126*, 187.

(181) Jabr-Milane, L.; van Vlerken, L.; Devalapally, H.; Shenoy, D.; Komareddy, S.; Bhavsar, M.; Amiji, M. *J. Controlled Release* **2008**, *130*, 121.

(182) Peer, D.; Karp, J. M.; Hong, S.; Farokhzad, O. C.; Margalit, R.; Langer, R. *Nat. Nanotechnol.* **2007**, *2*, 751.

(183) Savić, R.; Luo, L.; Eisenberg, A.; Maysinger, D. *Science* **2003**, *300*, 615.

(184) D'Souza, G. G. M.; Wagle, M. A.; Saxena, V.; Shah, A. *Biochim. Biophys.Acta, Bioenerg.* **2011**, *1807*, 689.

(185) Sharma, A.; Soliman, G. M.; Al-Hajaj, N.; Sharma, R.; Maysinger, D.; Kakkar, A. *Biomacromolecules* **2012**, *13*, 239.

(186) Marrache, S.; Dhar, S. *Proc. Natl. Acad. Sci. U.S.A.* **2012**, *109*, 16288.

(187) Paunesku, T.; Vogt, S.; Lai, B.; Maser, J.; Stojićević, N.; Thurn, K. T.; Osipo, C.; Liu, H.; Legnini, D.; Wang, Z.; Lee, C.; Woloschak, G. E. *Nano Lett.* **2007**, *7*, 596.

(188) Wang, L.; Liu, Y.; Li, W.; Jiang, X.; Ji, Y.; Wu, X.; Xu, L.; Qiu, Y.; Zhao, K.; Wei, T.; Li, Y.; Zhao, Y.; Chen, C. *Nano Lett.* **2010**, *11*, 772.

(189) Esumi, K.; Houdatsu, H.; Yoshimura, T. *Langmuir* **2004**, *20*, 2536.

(190) Esumi, K.; Takei, N.; Yoshimura, T. *Colloids Surf., B* **2003**, *32*, 117.

(191) Bennett, L. E.; Ghiggino, K. P.; Henderson, R. W. *J. Photochem. Photobiol., B* **1989**, *3*, 81.

(192) Park, S. Y.; Baik, H. J.; Oh, Y. T.; Oh, K. T.; Youn, Y. S.; Lee, E. S. *Angew. Chem. Int. Ed.* **2011**, *50*, 1644.

(193) Siggel, U.; Bindig, U.; Endisch, C.; Komatsu, T.; Tsuchida, E.; Voigt, J.; Fuhrhop, J. H. *Ber. Bunseng. Phys. Chem.* **1996**, *100*, 2070.

(194) Yuan, Y.; Feng, G.; Qin, W.; Tang, B. Z.; Liu, B. *Chem. Commun.* **2014**, *50*, 8757.

(195) Horobin, R. W.; Trapp, S.; Weissig, V. *J. Controlled Release* **2007**, *121*, 125.

(196) Smith, R. A. J.; Porteous, C. M.; Gane, A. M.; Murphy, M. P. *Proc. Natl. Acad. Sci. U.S.A.* **2003**, *100*, 5407.

LIST OF PUBLICATIONS

(1) **Feng, G.**; Qin, W.; Hu, Q.; Tang, B. Z.; Liu, B. Cellular and mitochondria dual targeted organic dots with aggregation-induced emission characteristics for image-guided photodynamic therapy. *Adv. Healthcare Mater.* **2015**. (***Accepted, Chapter 5***)

(2) **Feng, G.**; Yuan, Y.; Hu, F.; Zhang, R.; Xing, B.; Zhang, G.; Zhang, D.; Liu, B. Light-up probe with aggregation-induced emission characteristics (AIE) for selective imaging, naked-eye detection and photodynamic killing of Gram-positive bacteria. *Chem. Commun*. **2015**, 51, 12490-12493.

(3) Gao, Y.; **Feng, G.**; Goh, C. C.; Ng, N. G.; Liu, B.; Li, B.; Yang, L.; Hua, J. Biocompatible Nanoparticles Based on Diketo-pyrrolo-pyrrole (DPP) with Aggregation-Induced Red/NIR Emission for In Vivo Two-photon Fluorescence Imaging. *Adv. Funct. Mater.* **2015**, 25, 2857-2866. (***First co-author***)

(4) **Feng, G.**; Liu, J.; Geng, J.; Liu, B. Unfunctionalized conjugated polymer microparticles for selective cancer cell image-guided photothermal therapy, *J. Mater. Chem. B* **2015**, 3, 1135-1141.

(5) **Feng, G.**; Liu, J.; Zhang, R.; Liu, B. Cell imaging with red fluorescent light-up probe based on environment-sensitive fluorogen with intramolecular charge transfer characteristics. *Chem. Commun.* **2014**, 50, 9497-9500.

(6) Yuan, Y.; **Feng, G.**; Qin, W.; Tang, B. Z.; Liu, B. Targeted and Image-guided Photodynamic Cancer Therapy based on Organic Nanoparticles with Aggregation-induced Emission Characteristics. *Chem Commun.* **2014**, 50, 8587-8760. (***First co-auther; Chapter 4***)

(7) **Feng, G.**; Tay, C. Y.; Chu, Q.; Liu, R.; Tomczak, N.; Liu, J.; Tang, B. Z.; Leong, D. T.; Liu, B. Ultrabright organic dots with aggregation-induced emission characteristic as a facile cell tracker. *Biomaterials* **2014**, 35, 8669-8677. (***Chapter 2***)

(8) **Feng G.**; Li, K.; Liu, J.; Ding, D.; Liu, B. Bright Single-Chain Conjugated Polymer Dots Embedded Nanoparticles for Long-term Cell Tracing and Imaging. *Small* **2014**, 6, 1212-1219.

(9) **Feng, G.**; Ding, D.; Li, K.; Liu, J.; Liu, B. Reversible Photoswitching Conjugated Polymer Nanoparticles for Cell and Tumor Imaging. *Nanoscale* **2014**, 4, 4141-4147.

(10) **Feng, G.**; Liang, J.; Liu, B. Hyperbranched Conjugated Polyelectrolytes for Biological Sensing and Imaging. *Macromol. Rapid Commun.* **2013**, 34(9), 705-715. (***Review***)

(11) **Feng, G.**; Ding, D.; Liu, B. Fluorescence Bioimaging with Conjugated Polyelectrolytes. *Nanoscale* **2012**, 4, 6150-6165. (***Review***)

(12) Zhang, M.; **Feng, G.**; Song, Z.; Zhou, Y.; Chao, H.; Yuan, D.; Tan, T. Y.; Guo, Z.; Hu, Z.; Tang, B. Z.; Liu, B.; Zhao, D. Two-dimensional metal-organic

framework with wide channels and responsive turn-on fluorescence for the chemical sensing of volatile organic compounds, *J. Am. Chem. Soc.* **2014**, 136, 7241-7244.

(13) Liu, J.; **Feng, G.**; Liu, R.; Tomczak, N.; Ma, L.; Gurzadyan, G. G.; Liu, B. Bright Quantum-Dot-Sized Single-Chain Conjugated Polyelectrolyte Nanoparticles: Synthesis, Characterization and Application for Specific Extracellular Labeling and Imaging. *Small* **2014**, 10, 3110-3118.

(14) Liu, J.; **Feng, G.**; Ding, D.; Liu, B. Bright far-red/near-infrared fluorescent conjugated polymer nanoparticles for targeted imaging of HER2-positive cancer cells. *Polym. Chem.* **2013**, 4, 4326-4334.

(15) Liu, J.; **Feng, G.**; Geng, J.; Liu, B. A Facile Strategy towards Conjugated Polyelectrolyte with Oligopeptide as Pendants for Biological Applications. *ACS Appl. Mater. Interfaces* **2013**, 5, 4511-4515.

(16) Hu, Q.; Gao, M.; **Feng, G.**; Chen, X.; Liu, B. A Cell Apoptosis Probe Based on Fluorogen with Aggregation Induced Emission Characteristics. *ACS Appl. Mater. Interfaces* **2015**, 7, 4875-4882.

(17) Hu, Q.; Gao, M.; **Feng, G.**; Tomczak, N.; Liu, R.; Xing, B.; Tang, B. Z.; Liu, B. A Multifunctional Probe with Aggregation-Induced Emission Characteristics for Selective Fluorescence Imaging and Photodynamic Killing of Bacteria Over Mammalian Cells. *Adv. Healthcare Mater.* **2015**, 4,659-663.

(18) Gomez-Duran, C. F. A.; Hu, R.; **Feng, G.**; Li, T,; Bu, F.; Arseneault, M.; Liu, B.; Peña-Cabrera, E.; Tang, B. Z. Effect of AIE Substituents on the Fluorescence of Tetraphenylethene-Containing BODIPY Derivatives. *ACS Appl. Mater. Interfaces* **2015**. DOI: 10.1021/acsami.5b05033

(19) Hu, Q.; Gao, M.; **Feng, G.**; Liu, B. Mitochondria-Targeted Cancer Therapy Using a Light Up probe with Aggregation-induced Emission Characteristics. *Angew. Chem. Int. Ed.* **2014**, 53, 14225-14229.

(20) Cai, X.; Zhan, R.; **Feng, G.**; Liu, B. Organometallic Conjugated Polyelectrolytes: Synthesis and Applications, *J. Inorg. Org. Polym. Mater.* **2015**, 25, 27-36.

(21) Hu, Q.; Gao, M.; **Feng, G.**; Tang, B. Z.; Liu, B. Fluorescent light-up probe with "AIE + ESIPT" characteristics for specific detection of lysosomal esterase. *J. Mater. Chem. B* **2014**, 2, 3438-3442.

(22) Yuan, Y.; Kwok, R. T. K.; **Feng, G.**; Liang, J.; Geng, J.; Tang, B. Z.; Liu, B. Rational Design of Fluorescent Light-Up Probes Based on an AIE Luminogen for Targeted Intracellular Thiol Imaging. *Chem. Commun.* **2013**, 50, 295–297.

(23) Ding, D.; Liu, J.; **Feng, G.**; Li, K.; Hu, Y.; Liu, B. Bright Far-Red/Near-Infrared Conjugated Polymer Nanoparticles for In Vivo Bioimaging. *Small* **2013**, 9, 3093-3102.

(24) Qin W.; Li, K.; **Feng, G.**; Li, M.; Yang, Z.; Liu, B.; Tang, B. Z. Bright and photostable Organic Fluorescent Dots with Aggregation-Induced Emission Characteristics for Noninvasive Long-term Cell Imaging. *Adv. Funct. Mater.* **2013**, 24, 635-643.

(25) Ding, D.; Goh, C. C.; **Feng, G.**; Zhao, Z.; Liu, J.; Liu, R.; Tomczak, N.; Geng, J.; Tang, B. Z.; Ng, L. G.; Liu, B. Ultrabright Organic Dots with Aggregation-Induced Emission Characteristics for Real-Time Two-Photon Intravital Vasculature Imaging. *Adv. Mater.* **2013**, 25, 6083-6088.

(26) Zhang, C.-J.; Hu, Q.; **Feng, G.**; Zhang, R.; Yuan, Y.; Lu, X.; Liu, B. Image-guided combination chemotherapy and photodynamic therapy using a mitochondria-targeted molecular probe with aggregation-induced emission characteristics. *Chem. Sci.* **2015**. DOI: 10.1039/C5SC00826C

(27) Xiang, J.; Cai, X.; Lou, X.; **Feng, G.**; Min, X.; Luo, W.; He, B.; Goh, C. C.; Ng, L. G.; Zhou, J.; Zhao, Z.; Liu, B.; Tang, B. Z. Biocompatible Green and Red Fluorescent Organic Dots with Remarkably Large Two-Photon Cross Action Sections for Targeted Cellular Imaging and Real-Time Intravital Blood Vascular Visualization. *ACS Appl. Mater. Interfaces* **2015**. DOI: 10.1021/acsami.5b03766

(28) Ding, D.; Kwok, R. T. K.; Yuan, Y.; **Feng, G.**; Tang, B. Z.; Liu, B. Fluorescent Light-up Nanoparticle Probe with Aggregation-induced Emission Characteristics and Tumor-acidity Responsiveness for Targeted Imaging and Selective Suppression of Cells, *Mater. Horiz.* **2015**, 2, 100-105.

(29) Zhang, R.; Yuan, Y.; Liang J.; Kwok, R. T. K.; Zhu, Q.; **Feng, G.**; Geng, J.; Tang, B. Z.; Liu, B. Fluorogen-peptide conjugates with tunable aggregation-induced emission characteristics for bioprobe design. *ACS Appl. Mater. Interfaces* **2014**, 6, 14302-14310.

(30) Gao, M.; Sim, C. K.; Leung, C. W. T.; Hu, Q.; **Feng, G.**; Xu, F.; Tang, B. Z., Liu, B. A fluorescent light-up probe with AIE characteristics for specific mitochondrial imaging to identify differentiating brown adipose cells, *Chem. Commun.* **2014**, 50, 8312-8315.

(31) Ding, D.; Liang, J.; Shi, H.; Kwok, R. T. K.; Gao, M. **Feng, G.**; Yuan, Y.; Tang, B. Z.; Liu, B. Light-Up Bioprobe with Aggregation-Induced Emission Characteristics for Real-Time Apoptosis Imaging in Target Cancer Cells, *J. Mater. Chem. B* **2013**, 2, 231-238.